Mechanics of Ultra-Thin Composite Coilable Structures

Thesis by
Christophe Leclerc

In Partial Fulfillment of the Requirements for the
Degree of
Doctor of Philosophy

CALIFORNIA INSTITUTE OF TECHNOLOGY
Pasadena, California

2020
Defended December 13, 2019

Christophe Leclerc
ORCID: 0000-0003-1999-4757

ACKNOWLEDGEMENTS

Many people at Caltech and around the world supported me during the completion of this work, and their help made this success possible. First and foremost, I would like to thank my advisor, Professor Sergio Pellegrino. My decision to come to Caltech was mainly driven by my interest toward the research done by Professor Pellegrino, and I am glad I had the chance to work with him. I am extremely thankful for his guidance, expertise and encouragement throughout my PhD. He pushed us to improve every aspect of our work, and was always available to help us when needed.

I would also like to thank the members of my candidacy and defense committees for their help and all the useful feedback they shared with me, Prof. Bhattacharya, Prof. Daraio, Prof. Ravichandran, Prof. Rosakis and Dr. Mobrem.

The Space Solar Power Project is an ambitious endeavour that provided tangible applications for my work, and it was a privilege to be part of such project. I would like to thank all past and present members of this collaborative effort, particularly Professor Harry Atwater and Professor Ali Hajimiri.

I would also like to thank the Keck Institute for Space Studies for their funding. I will always be grateful to Michele Judd, who organized many incredible events throughout my stay at Caltech, and really helped improving my experience at Caltech.

I had the chance to be supported by multiple mentors throughout the years that pushed me to become a better researcher and engineer. Specifically, I would like to thank Dr. Gregory Davis, Dr. Daniel Scharf and John Baker for their invaluable advices during the AAReST project, and Professor Annie Ross from Polytechnique Montréal who gave me a chance to start doing research very early, and taught me a lot about how to conduct scientific research.

I would like to acknowledge past and present members of the Space Structure Laboratory for their support, and for the ideas and discussions we shared that helped pushing my research forward: Manan Arya, Miguel Bessa, Stephen Bongiorno, Federico Bosi, Mélanie Delapierre, Charles Dorn, Serena Ferraro, Terry Gdoutos, Ashish Goel, Armanj Hasanyan, Yang Li, Chinthaka Mallikarachchi, Michael Marshall, Antonio Pedivellano, Harsha Reddy, Fabien Royer, Maria Sakovsky, Charles Sommer, John Steeves, Thibaud Talon, Alan Truong, Kanthasamy Ubamanyu, Yuchen Wei, Alexander Wen, and Lee Wilson.

My time at Caltech would have been much harder without the support from many friends: my colleagues during the first year in GALCIT which was a challenging experience and would have been impossible without them; my friends from volleyball and soccer, with whom I was able to stay active during my PhD; and all the other friends that helped me maintain a healthy work-life balance.

I will always be grateful to my parents, Céline and Denis, who supported me since the very beginning, for instilling the value of education, for pushing me to follow my passions, and for being always there for me.

And lastly, I would like to express my deepest gratitude to my better half, Catherine, who always stayed by my side despite the distance, who always encouraged me, and who gave me the strength to accomplish this journey. Her support throughout my time at Caltech was invaluable, and I will always be thankful.

This work was partially funded by the Natural Sciences and Engineering Research Council of Canada.

ABSTRACT

Coilable structures are thin-shell structures that can be coiled around a hub by flattening their cross-section. They are attractive for multiple space applications as they allow efficient packaging and deployment of large planar structures. Reducing the shell thickness enables smaller coiling radius and more efficient packaging.

This thesis investigates TRAC structures, a type of coilable structure, made of ultra-thin composite materials. A design using a laminate made of glass fiber plainweave fabric and carbon fiber unidirectional tape is proposed, leading to a shell thickness of 80 µm. An in-autoclave, two-cure manufacturing process is presented, and a shape measurement method is used to mitigate post-cure shape changes due to residual stresses.

A study of the structure behavior in its deployed configuration is performed. First, the behavior when subjected to pure bending is investigated experimentally for structures with a length of 575 mm. Two regimes are observed, with a pre-buckling phase transitioning to a stable post-buckling phase after an initial buckling event. The ultimate buckling moment following the stable post-buckling regime can be as high as four times the initial buckling moment. A finite element model is developed and is able to reproduce all the features observed experimentally, except the ultimate buckling. This simulation model is used to study the effect of varying the structure length from 300 mm to 5000 mm on the initial buckling moment. Results show that nonlinearities in the pre-buckling deformations of the flanges under compression lead to a constant wavelength lateral-torsional buckling mode for which the critical moment is mostly constant across the range of length. The torsional behavior of the TRAC structure is also investigated. Good agreement is obtained between experiments and numerical simulations, and initial twist in the structure is shown to have little effect on the overall behavior due to the small torsional stiffness in the undeformed configuration.

An analytical method to predict the buckling load of a TRAC structure under pure bending is presented. It is achieved by considering only one flange of the structure and solving the problem of a cylindrical shell panel with a longitudinal free edge under non-uniform axial compression. Partially uncoupled stability equations for a balanced laminate are derived and are used in conjunction with the Rayleigh-Ritz method to approximate the buckling load. This method overestimates the buckling

load by 44% in the case of a 500 mm TRAC structure made with ultra-thin composite materials.

A study of the coiling behavior is also presented. High localized curvature in the transition region between the coiled and deployed regions is observed in experiments, leading to material failure for a structure made only of carbon fiber unidirectional tape. A numerical framework is developed and reproduces the localized curvature observed in experiments, predicting stress concentration at this location. The study shows that changing the laminate to a a single ply of carbon fiber unidirectional tape sandwiched between plies of glass fiber plainweave fabrics reduces significantly the maximum stress in the transition region, to the extent that the highest stress is now in the fully coiled region and can be accurately predicted using simple equations based on the change of curvatures due to the coiling process.

PUBLISHED CONTENT AND CONTRIBUTIONS

Leclerc, Christophe and Pellegrino, Sergio (2019). "Reducing Stress Concentration in the Transition Region of Coilable Ultra-Thin-Shell Booms". In: *AIAA Scitech 2019 Forum*. 2019–1522. San Diego, CA. DOI: 10.2514/6.2019-1522.
C.L. developed the numerical framework, performed all the simulations, proposed the improvements to the coiling process and the boom geometry, and wrote the manuscript.

Leclerc, Christophe, Pedivellano, Antonio, and Pellegrino, Sergio (2018). "Stress Concentration and Material Failure During Coiling of Ultra-Thin TRAC Booms". In: *2018 AIAA Spacecraft Structures Conference*. 2018–0690. Orlando, FL.
C.L. designed and performed the experiments, participated in the analysis of the results, and co-wrote the manuscript.

Leclerc, Christophe and Pellegrino, Sergio (2017). "Ultra-Thin Composite Deployable Booms". In: *IASS Annual Symposium "Interfaces: Architecture. Engineering. Science"*. Hamburg, Germany.
C.L. developed the manufacturing process and the shape measurement method, performed the experiments, and wrote the manuscript.

Leclerc, Christophe, Wilson, Lee, Bessa, Miguel A, and Pellegrino, Sergio (2017). "Characterization of Ultra-Thin Composite Triangular Rollable and Collapsible Booms". In: *4th AIAA Spacecraft Structures Conference*. 2017–0172. Grapevine, TX.
C.L. developed the manufacturing process, performed the experiments on the deployed behavior, and co-wrote the manuscript.

TABLE OF CONTENTS

LIST OF ILLUSTRATIONS

LIST OF TABLES

Chapter 1

INTRODUCTION

1.1 Motivation

Deployable structures have been used extensively in many spacecraft architectures as they allow efficient packaging of large systems that could not otherwise comply with tight volume requirements of current launch vehicles. One type of such structures is a coilable structure, for which the cross-section can be elastically flattened such that the structure can be rolled around a hub for packaging. These thin-shell structures can often be passively deployed using the stored strain energy, making them attractive for some applications.

One of the main uses of coilable structures is to deploy and support large aperture systems such as antennas (Leipold, Runge, and Sickinger, 2005), photovoltaic surfaces (Campbell et al., 2006), and solar sails (Banik and Ardelean, 2010; Leipold et al., 2003). For such systems, the coilable structures are used as booms that support a large membrane-like structure encompassing the desired functionalities, improving packaging efficiency.

Coilable booms have been used in multiple spacecraft designs. Figure 1.1a shows the spacecraft NanoSail-D, a NASA solar sail mission that was launched in November 2010 and deployed in January 2011 (Johnson et al., 2011; Whorton et al., 2008). The four triangular sections of the sail, made of a 2 µm thick polymer film coated with aluminum on one side, were deployed using four coilable booms along the diagonals. Figure 1.1b shows the Roll-Out Solar Array, a demonstration mission of a deployable solar array (Chamberlain, Kiefer, and Banik, 2018; Hoang et al., 2016; Spence et al., 2018). It was deployed from the International Space Station in June 2017 using two longitudinal coilable booms.

Multiple concepts for coilable booms have been developed. One simple example is a regular tape spring, but other designs offer better mechanical performance such as the Collapsible Tube Mast (CTM) (Aguirre-Martinez et al., 1986; Herbeck et al., 2001), the SHEARLESS boom (Fernandez, 2017, 2018), and the Storable Tubular Extendible Member (STEM) (Rimrott, 1965). Figure 1.2 compares the cross-section of various coilable booms.

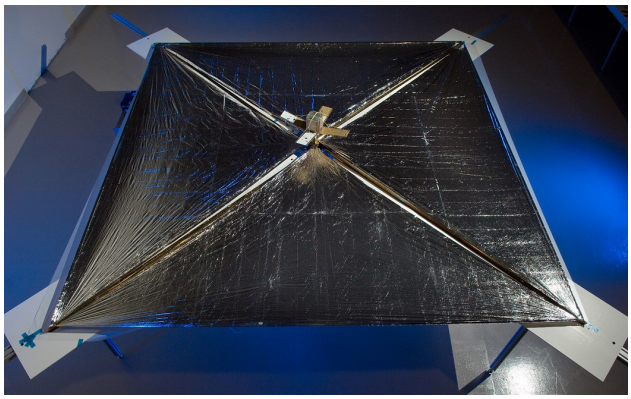

(a) NanoSail-D (Credit photo: NASA/MSFC/D-Higginbotham, 2012).

(b) Roll-Out Solar Array (NASA, 2019).

Figure 1.1: Example of spacecraft missions using coilable booms.

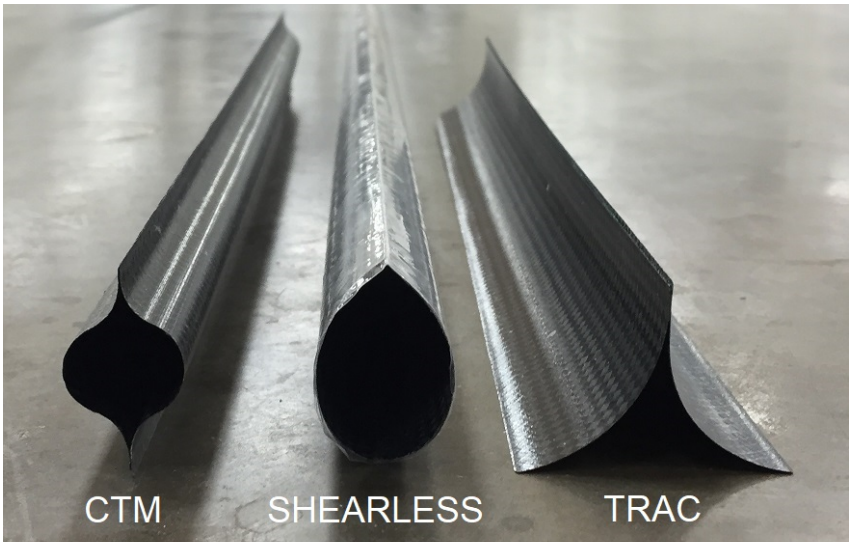

Figure 1.2: Comparison of the CTM, SHEARLESS and TRAC cross-sections (Credit: NASA, Fernandez, 2017).

A recent concept for coilable booms is the Triangular Rollable And Collapsible (TRAC) boom (Murphey and Banik, 2011). It was developed by the Air Force Research Laboratory and was shown to exhibit high bending stiffness-to-packaged height ratio when compared to the CTM and the STEM booms (Roybal, Banik, and Murphey, 2007). The TRAC cross-section consists of two circular arcs (tape springs) attached along one edge, forming two curved flanges and a flat web, as shown in Figure 1.3. This type of boom has already flown on three different solar sails demonstrations: NASA's NanoSail-D (Johnson et al., 2011; Whorton et al., 2008), and the Planetary Society's LightSail-1 (Biddy and Svitek, 2012) and

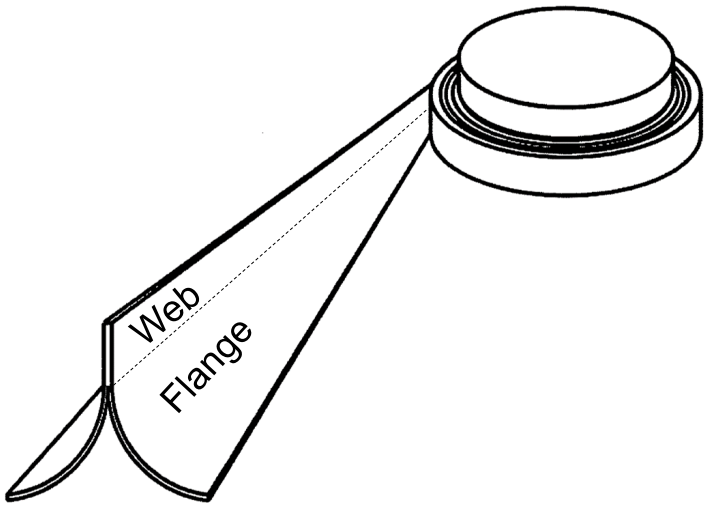

Figure 1.3: TRAC boom partially coiled around a cylindrical hub with the web and flange regions marked (modified from Murphey and Banik, (2011)).

LightSail-2 (Betts et al., 2017). In all three cases, the booms were made from a metal alloy. More recently, research has shown that metallic TRAC booms are sensitive to thermal gradients, causing large tip deflections when one flange is facing the sun in space, while the other flange remains in the shadow (Stohlman and Loper, 2016). Therefore, TRAC booms made of high-strain composites have been studied extensively in recent years.

While the TRAC cross-section was used exclusively in boom architectures in the past, other applications can benefit from the features of this cross-section while using it as different types of structural elements. The more general term *TRAC structure* will therefore be used to include all possible applications of structural elements using the TRAC cross-section.

A recent system-level study for a space solar power satellite architecture has shown the need for long coilable structural elements (longerons) with the TRAC cross-section (up to 60 m) with small required bending stiffness (around $6\,\mathrm{N\,m^2}$) (Arya, Lee, and Pellegrino, 2016). In such architecture, the longerons are mainly loaded in bending. Furthermore, this study showed that the packaging efficiency of such structure increases significantly by reducing the thickness of the flanges of the TRAC structural elements. Ultra-thin coilable structures are also attractive for small satellites, as they can be coiled around small hubs, reducing the volume requirements.

A key feature of a TRAC structure is its thin-walled open cross-section, leading to a

complex, nonlinear behavior both in the deployed configuration and during coiling (Murphey, Turse, and Adams, 2017). Inner flange buckling is observed during coiling, leading to high localized strains and potentially material failure (Cox and Medina, 2018, 2019; Murphey, Turse, and Adams, 2017). Buckling when subjected to pure bending is localized and can lead to a stable post-buckling regime (Banik and Murphey, 2010). Reducing the thickness amplifies these challenges.

1.2 Research Goals, Methodology and Outline

The overall objectives of the research presented in this thesis are to implement and enable the use of ultra-thin ply composites in coilable structures, studying the specific case of the TRAC cross-section. These can be divided in 4 goals. 1) Develop a manufacturing process to fabricate coilable structures using the thinnest composites available. 2) Study the behavior in the deployed configuration when subjected to typical loading conditions such as pure bending and torsion. 3) Predict the buckling load under pure bending. 4) Understand and reduce stress concentrations observed during the coiling process.

One challenge of studying structures made of ultra-thin composites is that the material properties and structural performance are closely related to the manufacturing processes of both the structure itself and the thin-ply composite materials. The desire to push the limit of current technologies, aiming to use the thinnest material available, drives the methodology used in the current research.

As it will become evident throughout the thesis, many types of local effects are observed during experiments, and are very sensitive to both the actual shape of the prototypes and the material properties. Therefore, the first part of this thesis focuses on the manufacturing process for the coilable structures, the characterization of the as-built prototypes, and the determination of their material properties. Then, in subsequent chapters, both the deployed and coiling behavior are first studied experimentally to better understand the particularities due to the use of ultra-thin materials, and then studied using numerical simulations to analyze thoroughly the behavior.

This thesis is organized as follows. Chapter 2 details the design of the coilable structure prototypes, based on stiffness requirements. Thin-ply composite materials are introduced and their mechanical properties are measured. The TRAC structure manufacturing process is presented, and the method to characterize the post-cure shape of the prototypes is introduced.

The behavior of the coilable structure in its deployed configuration is studied in Chapter 3. Using both experimental and numerical methods, buckling when subjected to pure bending is analyzed. It is observed that an initial buckling event is followed by a stable post-buckling regime before reaching ultimate buckling. The effect of varying the structure length from 300 mm to 5000 mm on the initial buckling load is also investigated. Finally, the torsional behavior is also studied.

An analytical model to predict the initial buckling load of coilable structures is presented in Chapter 4. The buckling of a TRAC structure under pure bending is analyzed by considering a curved panel simply supported on three sides and free along one longitudinal edge, loaded with non-uniform axial compression. The Rayleigh-Ritz method is used with the second variation of the total potential energy to estimate the buckling load. A structure made from isotropic materials is first studied, and then the model is extended to a structure made from orthotropic materials. A comparison of the predicted buckling load from this model is also made with results from numerical simulations.

The behavior of the coilable structure during coiling is investigated in Chapter 5. Preliminary coiling experiments of ultra-thin composite coilable structures made from the first laminate that was considered are first performed, showing material failure in the inner flange. A numerical simulation framework is developed to better understand the stress distribution in the transition region between the fully deployed and fully coiled regions. To reduce the high localized curvature observed from numerical results, a new laminate is proposed, for which no stress concentrations are observed in the transition region.

Finally, Chapter 6 concludes this thesis by summarizing the main results and the principal contributions. Areas of future research are also presented.

Chapter 2

TEST PROTOTYPES DESIGN, MANUFACTURING AND CHARACTERIZATION

This chapter describes the design process that led to the prototypes that were studied throughout this research. An overview of thin-ply composites is first presented, highlighting how they differ from typical composites and what are their advantages. Second, a TRAC cross-section is chosen based on stiffness requirements derived from a system-level study for a space solar power satellite architecture while utilizing the thinnest composite materials available. Third, the mechanical properties of the materials used in the design are characterized, both at the ply level and at the laminate level. Then, the manufacturing process for the TRAC structures is presented. Finally, a method to measure the shape of TRAC structure post-cure is introduced.

Parts of section 2.5 were modified from the following publication:

Leclerc, Christophe and Pellegrino, Sergio (2017). "Ultra-Thin Composite Deployable Booms". In: *IASS Annual Symposium "Interfaces: Architecture. Engineering. Science"*. Hamburg, Germany.

2.1 Thin-Ply Composite

Thin-ply composites, usually defined as having a ply thickness of less than 100 µm, have been made available in recent years due to advancements in manufacturing technologies such as the tow-spreading process (Sihn et al., 2007). The advantages of using thin-ply materials have been studied by many authors, demonstrating improved mechanical properties when compared to traditional, thick-ply composite materials (Amacher et al., 2014; Sihn et al., 2007). In particular, it was observed that some failure modes such as delamination and transverse cracking are mostly suppressed in thin-ply laminated composites, delaying the onset of damage, increasing the ultimate strength and significantly reducing the performance loss after fatigue loading cycles. Furthermore, thin-ply composites expand the design space of laminates by increasing the number of plies, allowing more flexibility in tailoring the mechanical properties through ply orientation, while keeping the overall laminate thickness low.

Two types of thin-ply composites are of interest in the current research: unidirectional carbon fiber tape and glass fiber plainweave. The thinnest available carbon fiber tape is currently manufactured by North Thin Ply Technology using a tow-spreading process. The fiber areal density of this material can be as low as $17\,\mathrm{g\,m^{-2}}$, corresponding to a thickness of about $18\,\mu\mathrm{m}$. For the glass fiber plainweave, JPS Composites manufactures a wide range of fabrics, with fiber areal density as low as $11\,\mathrm{g\,m^{-2}}$.

For coilable structures with the TRAC cross-section, thin-ply composites are very attractive as they can significantly reduce the flange thickness, therefore decreasing the maximum strains in the material during flattening of the cross-section and coiling around the hub. This in turn helps improve the packaging efficiency and reduce the minimum coiling radius.

2.2 Design of Prototypes

Multiple iterations of ultra-thin composite TRAC structure were studied during the present research. These iterations were driven by improvement in manufacturing techniques, availability of new materials and better understanding of the mechanics of TRAC structure. Only the two most important design iterations are presented in this section. The first prototypes were designed initially to comply with the requirements detailed in Section 2.2.1 while using the thinnest material available. This design process is presented here in detail. Then, a study of the coiling behavior, detailed in Chapter 5, showed that the initial design led to high stress concentrations during coiling. An improved laminate mitigating this issue was developed, and is detailed at the end of this section.

2.2.1 Design Requirements

Initial research on ultra-thin composites TRAC structure was achieved in the context of the Space Solar Power Project, an ongoing effort at the California Institute of Technology to develop key technologies enabling space-based solar power collection and distribution. The initial structural concept was developed by Arya, Lee, and Pellegrino, (2016). It consists of strips of various lengths that are stiff in bending due to the use of two continuous longerons with TRAC cross-section along the edges of each strip, as shown in Figure 2.1. This study found that a strip bending stiffness of $11\,\mathrm{N\,m^2}$ was optimal in term of specific power. It corresponds to TRAC structures with a bending stiffness of $5.5\,\mathrm{N\,m^2}$, roughly one order of magnitude less than the TRAC booms previously studied by other researchers (Banik and Murphey, 2010;

Roybal, Banik, and Murphey, 2007). This demonstrates the need for new designs of ultra-thin composite TRAC structures.

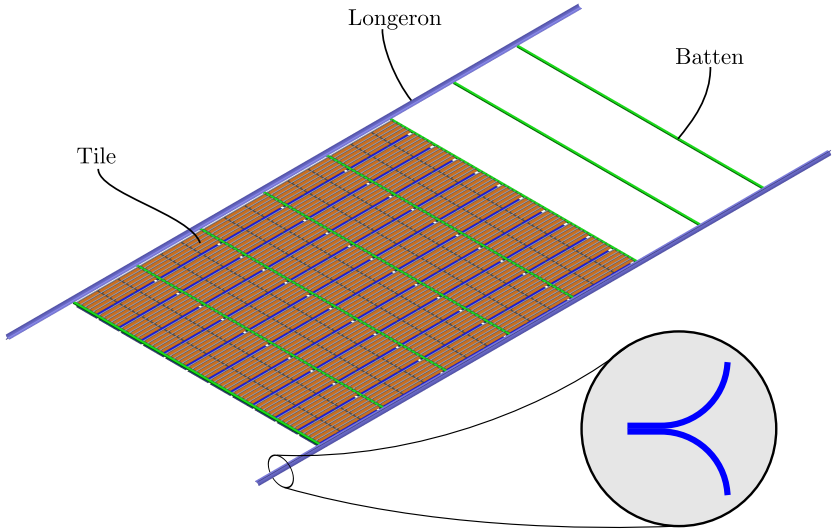

Figure 2.1: Strip architecture for the Space Solar Power Project. It consists of two TRAC longerons connected by battens supporting multiple tiles, which are the functional elements. The TRAC longerons are aligned such that the web is within the plane of the strip, allowing it to be coiled around a hub. (Credit: Arya, Lee, and Pellegrino, 2016)

Therefore, the two driving requirements for the design of prototype structures are: 1) a bending stiffness of about 5.5 N m^2 when loaded with one flange in compression and one flange in tension, and 2) the smallest possible flange thickness to improve packaging efficiency.

2.2.2 Bending Stiffness of TRAC Structures

To design a TRAC structure complying with these requirements, analytical estimates of the bending stiffness were derived. While only the bending stiffness around the Y axis, defined in Figure 2.2, was of particular interest for the strip architecture, estimates for the bending stiffness around both axes are derived. Figure 2.2 shows the TRAC cross-section. The main parameters are the web width w and the flange radius r, opening angle θ_f, and thickness t. A bond line thickness t_b is included so the total web thickness is $2t + t_b$. The Y axis is parallel to the web, while the X axis is perpendicular. The origin of the coordinate system is at the base of the web, where the flanges are attached. Z is in the longitudinal direction. The location of the centroid of the cross-section is marked as (X_c, Y_c). For the nominal geometry, the cross-section is symmetric about the Y axis and therefore $X_c = 0$.

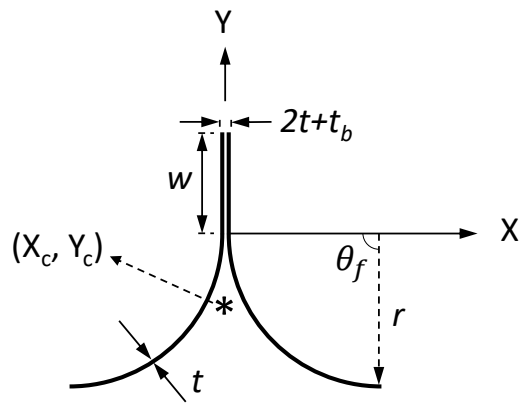

Figure 2.2: TRAC cross-section, defined by: web width w, flange radius r, opening angle θ_f and thickness t, and bonding line thickness t_b. The centroid, shown as a star, is located at (X_C, Y_C).

The main assumptions used to estimate the bending stiffness are:

1. The structure is made of two halves bonded together along the web and they are assumed to be uniform and equal thickness shells.
2. When loaded with pure bending, the longitudinal axis of the structure deforms to a circular arc with constant curvature radius ρ.
3. The cross-section does not deform.

The first step is to find the location of the centroid. Due to symmetry, $X_c = 0$, and Y_c of the cross-section is the same as Y_c for one of the halves, as it has the same value for each half. The web (1) and flange (2) regions can be considered separately. For the web, $Y_{c1} = w/2$. For the flange, Figure 2.3 shows the location of the centroid in a rotated coordinate system, where the X' axis is the bisector of θ_f. X'_c can be found by solving

$$\int_{-\theta_f/2}^{\theta_f/2} \left(X' - X'_c\right) r d\theta = 0 \longrightarrow X'_c = \frac{r \sin\left(\theta_f/2\right)}{\theta_f/2} \tag{2.1}$$

Then, the centroid of the TRAC section is computed as

$$Y_c = \frac{l_1 Y_{c1} + l_2 Y_{c2}}{l_1 + l_2} = \frac{w^2/2 - 2r^2 \sin^2\left(\theta_f/2\right)}{w + r\theta_f} \tag{2.2}$$

where l_1 and l_2 are the arclengths of the web and flange regions, respectively, and Y_{c1} and Y_{c2} are their respective centroids. They are expressed as

$$l_1 = w \qquad l_2 = r\theta_f \qquad Y_{c1} = \frac{w}{2} \qquad Y_{c2} = -\sin\left(\theta_f/2\right) X'_c \tag{2.3}$$

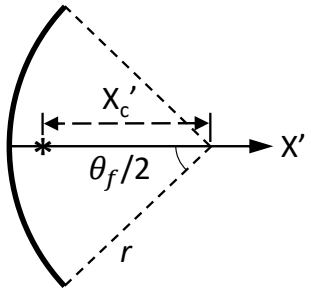

Figure 2.3: Centroid location of one flange in a rotated coordinate system where the X' axis is the bisector of θ_f.

For the bending stiffness around the Y axis,

$$M_Y = \int_s X N_Z ds \tag{2.4}$$

where N_Z is the axial stress resultant in the shell, and the integral is along the arclength of both halves of the section. Using the classical lamination theory (CLT), described in more detail in Section 2.3, the constitutive relation is

$$N_Z = \left(A_{11} - \frac{A_{12}^2}{A_{22}}\right)\varepsilon_Z \qquad \text{with} \qquad \varepsilon_Z = \frac{X}{\rho} \tag{2.5}$$

Substituting these equations in equation 2.4, the result is

$$M_Y = \frac{1}{\rho}\left(A_{11} - \frac{A_{12}^2}{A_{22}}\right)\int_s X^2 ds = \frac{(EI)_Y}{\rho} \tag{2.6}$$

where $(EI)_Y$ represents the bending stiffness around the Y axis. While this calculation does not directly include the second moment of area, this notation for the bending stiffness is preferred as it is often used in literature. Furthermore, an approximation of I_Y can be obtained by simply multiplying the integral $\int_s X^2 ds$ in equation 2.6 by the flange thickness t. Finally, solving the integral along the arclength, one can obtain

$$\begin{aligned}(EI)_Y = 2&\left(A_{11} - \frac{A_{12}^2}{A_{22}}\right)\\ &\left(w\bar{t}^2 + \frac{r^2}{2}\sin\theta_f\left(r\cos\theta_f - 4\left(r+\bar{t}\right)\right) + \frac{3r\theta_f}{2}\left(r^2 + \frac{4}{3}r\bar{t} + \frac{2}{3}\bar{t}^2\right)\right)\end{aligned} \tag{2.7}$$

where $\bar{t} = (t + t_b)/2$. A similar derivation for $(EI)_X$ yields

$$M_X = \frac{1}{\rho}\left(A_{11} - \frac{A_{12}^2}{A_{22}}\right)\int_s (Y - Y_C)^2\, ds = \frac{(EI)_X}{\rho} \tag{2.8}$$

$$(EI)_X = \left(A_{11} - \frac{A_{12}^2}{A_{22}}\right)\left(2w\left(\frac{w^2}{3} + Y_C^2 - wY_C\right)\right) + r\left(A_{11} - \frac{A_{12}^2}{A_{22}}\right)\left(r^2\theta_f + 2Y_C^2\theta_f - 4Y_C r\cos\theta_f + 4Y_c r - r^2\cos\theta_f\sin\theta_f\right) \tag{2.9}$$

2.2.3 Cross-Section Design

These equations for the bending stiffness can be used to design a TRAC structure following the requirements derived in Section 2.2.1. The first step is to select the thinnest laminate possible. Using materials from North Thin Ply Technology, the first laminate that was studied uses the stacking sequence $[0/90]_S$, where each layer is a 18 µm thick unidirectional carbon fiber tape with an epoxy resin, as described in Section 2.3. Using the corresponding material properties yields

$$\left(A_{11} - \frac{A_{12}^2}{A_{22}}\right) = 4.8 \times 10^6\ \mathrm{N\,m^{-1}} \tag{2.10}$$

To simplify the design, the flange opening angle was set at 90°, the web width at 8 mm, and it was assumed that $t_b = 0$. Solving equation 2.7 for the flange radius, the result is $r = 11.7$ mm. To simplify manufacturing, the radius was increased to the standard dimension 12.7 mm (0.5 inch). Table 2.1 summarizes the first prototype design.

Table 2.1: Cross-section geometry and bending stiffness estimates for the first TRAC prototype with a $[0/90]_S$ carbon fiber/epoxy laminate.

r [mm]	θ_f [°]	w [mm]	$(EI)_X$ [N m^2]	$(EI)_Y$ [N m^2]
12.7	90	8	11.2	7.1

While this initial design was obtained using the $[0/90]_S$ laminate, later work on coiling (presented in detail in Chapter 5) showed that a different laminate, a hybrid of glass fiber plainweave fabric and unidirectional plies of carbon fiber, performed better during coiling. This type of laminate, also referred as *FlexLam*, was initially proposed by Pollard and Murphey, (2006). A second prototype was therefore designed using this type of laminate. To achieve the desired bending stiffness, the new laminate selected is $[\pm 45_{GFPW}/0_{CF}/\pm 45_{GFPW}]$, where $GFPW$ denotes a ply made with the glass fiber fabric, and CF denotes a unidirectional carbon fiber ply. To achieve similar bending stiffnesses with the same cross-section, the single ply of carbon fiber is thicker, around 30 µm.

2.3 Material Characterization

To predict the performance of the manufactured TRAC structures, accurate values of the material properties are required. In this section, only the $[\pm 45_{GFPW}/0_{CF}/\pm 45_{GFPW}]$ laminate will be studied. The glass fiber plainweave prepreg is composed of a JPS E-glass fabric (style 1067, 31 g m^{-2}) and Patz PMT-F4 epoxy resin. The unidirectional carbon fiber prepreg tape is manufactured by North Thin Ply Technology from Torayca T800 carbon fibers and the epoxy resin system is ThinPreg 120 EPHTg-402.

For the glass fiber plain weave, the mechanical properties were measured on 4-ply flat laminates. E_1 and ν_{12} were measured by performing tension tests on three samples. As the glass fabric has the same fiber count in the warp and weft directions, it was assumed that $E_1 = E_2$, where the 1 and 2 directions are aligned with the fibers. Figure 2.4 shows a sketch of the experimental setup.

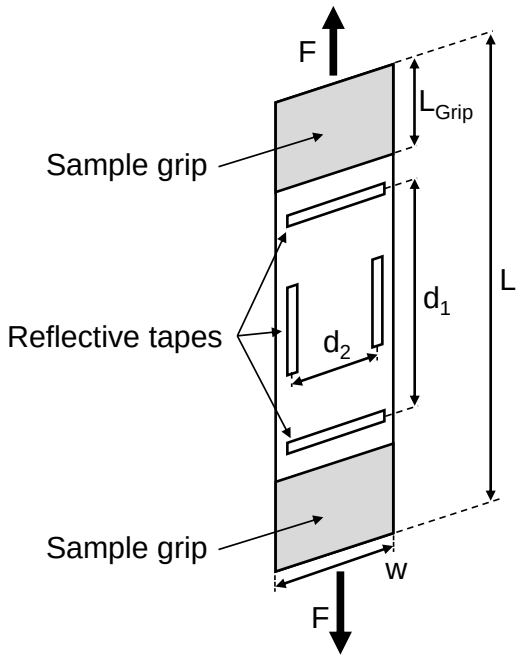

Figure 2.4: Tension test setup.

The tensile force F was measured with a 50 kN Instron load cell, while the axial and transverse strains were measured using two laser extensometers (LE-01 and LE-05 from Electronics Instrument Research). Reflective tape strips for these measurements were attached on the samples. Sandpaper pieces were bonded on the sample at both ends to increase friction and prevent slippage.

The sample dimensions were $w = 40$ mm, $t = 100$ µm, $L = 165$ mm and $L_{Grip} = 38$ mm.

The axial stress and the axial and transverse strains were obtained from

$$\sigma_1 = \frac{F}{wt} \qquad \varepsilon_1 = \frac{d_1 - d_1^0}{d_1^0} \qquad \varepsilon_2 = \frac{d_2 - d_2^0}{d_2^0} \tag{2.11}$$

where d_1^0 and d_2^0 are the initial values of d_1 and d_2, respectively. The stiffness and the Poisson's ratio were then obtained from

$$E_1 = \frac{\sigma_1}{\varepsilon_1} \qquad \nu_{12} = \frac{-\varepsilon_2}{\varepsilon_1} \tag{2.12}$$

The shear modulus, G_{12}, was measured by performing a 3-rail shear test, as described in ASTM D4255 (ASTM, 2015). Figure 2.5 shows a sketch of the test setup. A rectangular sample is clamped at both ends by rails that are fixed, while a third rail is attached in the middle of the sample. A vertical force is applied to the middle rail, creating two shear regions, one on each side.

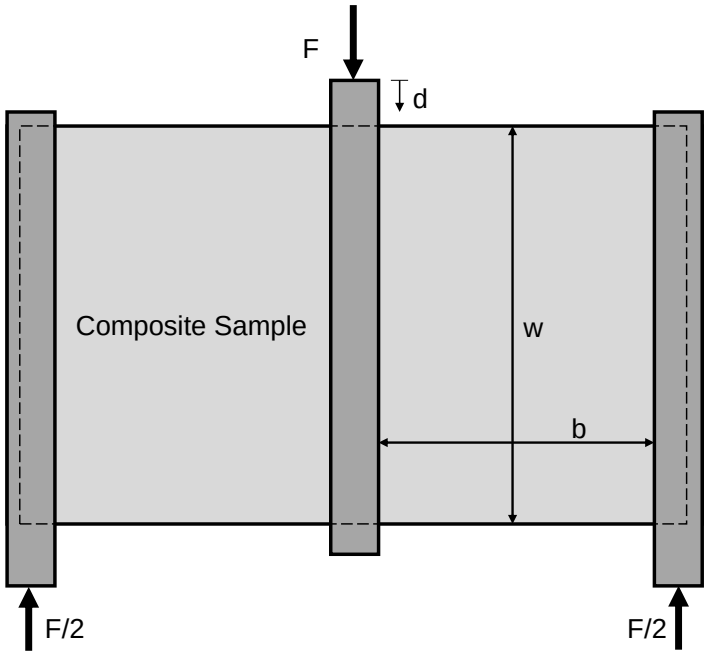

Figure 2.5: Three-rails shear test setup.

Three 151 x 138 mm samples were tested, with dimensions based on the fixture used (Wyoming Test Fixtures CU-3R-6). The distance between the rails was $b = 25.4$ mm. The vertical force F was measured with a 50 kN Instron load cell, and the shear displacement d was measured with a laser extensometer. The corresponding shear force for each region was $F/2$. The shear stress, shear strain and shear modulus

were obtained from

$$\tau_{12} = \frac{F/2}{wt} \qquad \gamma_{12} = \arctan\left(\frac{d}{b}\right) \qquad G_{12} = \frac{\tau_{12}}{\gamma_{12}} \tag{2.13}$$

The properties for the unidirectional carbon fiber prepregs were previously measured by Ning and Pellegrino, (2017). Table 2.2 summarizes the elastic properties of both materials.

Table 2.2: Elastic properties of carbon fiber and glass fiber plain weave prepregs.

	E_1 [GPa]	E_2 [GPa]	G_{12} [GPa]	ν_{12}	t [µm]
CF	128	6.5	7.6	0.35	30
GFPW	23.8	23.8	3.3	0.17	25

To predict the elastic behavior of the laminates, the classical lamination theory (CLT) described in Daniel and Ishai, (2005) was used,

$$\begin{bmatrix} \boldsymbol{N} \\ \boldsymbol{M} \end{bmatrix} = \begin{bmatrix} \boldsymbol{A} & \boldsymbol{B} \\ \boldsymbol{B} & \boldsymbol{D} \end{bmatrix} \begin{bmatrix} \boldsymbol{\varepsilon^0} \\ \boldsymbol{\kappa} \end{bmatrix} \tag{2.14}$$

where $\boldsymbol{N}$ and $\boldsymbol{M}$ are the forces and moments per unit length, $\boldsymbol{\varepsilon^0}$ and $\boldsymbol{\kappa}$ are the mid-plane strains and curvatures, $\boldsymbol{A}$ is the in-plane stiffness matrix, $\boldsymbol{B}$ is the in-plane/bending coupling matrix, and $\boldsymbol{D}$ is the bending stiffness matrix. The stiffness matrices are obtained from

$$\boldsymbol{A} = \sum_{k=1}^{n} \bar{\boldsymbol{Q}}_k \left(z_k - z_{k-1}\right) \tag{2.15}$$

$$\boldsymbol{B} = \frac{1}{2} \sum_{k=1}^{n} \bar{\boldsymbol{Q}}_k \left(z_k^2 - z_{k-1}^2\right) \tag{2.16}$$

$$\boldsymbol{D} = \frac{1}{3} \sum_{k=1}^{n} \bar{\boldsymbol{Q}}_k \left(z_k^3 - z_{k-1}^3\right) \tag{2.17}$$

$$\bar{\boldsymbol{Q}}_k = \boldsymbol{T}^{-1} \begin{bmatrix} \frac{E_1}{1-\nu_{12}\nu_{21}} & \frac{\nu_{12}E_2}{1-\nu_{12}\nu_{21}} & 0 \\ \frac{\nu_{12}E_2}{1-\nu_{12}\nu_{21}} & \frac{E_2}{1-\nu_{12}\nu_{21}} & 0 \\ 0 & 0 & G_{12} \end{bmatrix} \left(\boldsymbol{T}^{-1}\right)^T \tag{2.18}$$

where $\boldsymbol{T}$ is a rotation matrix that accounts for ply orientation, and z_k and z_{k-1} are the distances between the mid-plane of the laminate and the upper and lower surfaces of the k-th ply, respectively, as shown in Figure 2.6. For symmetric laminates, such as these used in this study, $\boldsymbol{B} = \boldsymbol{0}$. Using the properties from Table 2.2, both the $\boldsymbol{A}$ and $\boldsymbol{D}$ matrices were evaluated for the flange laminate.

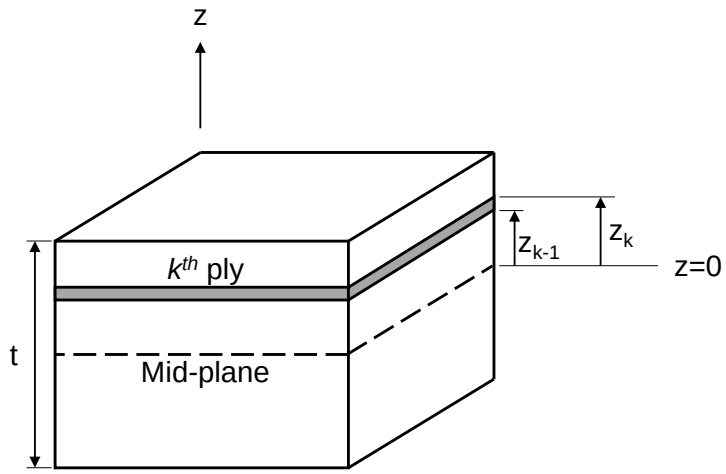

Figure 2.6: Definition of the ply coordinate system in a laminate.

To validate these stiffness matrices, tension and bending experiments were performed on flat samples of the laminate in both the longitudinal and transverse directions. As the web laminate is composed of twice the flange laminate plus a bonding ply, only the mechanical properties of the flange laminate were validated using this method.

The tension test was similar to the test performed on the glass fiber plainweave, shown in Figure 2.4. The sample dimensions were $w = 25\,\text{mm}$, $t = 80\,\mu\text{m}$ and $L = 245\,\text{mm}$. Three samples were tested for each direction (x and y, where x is aligned with the 0° direction). From equation 2.14:

$$\boldsymbol{\varepsilon^0} = \boldsymbol{aN} \tag{2.19}$$

where $\boldsymbol{a}$ is the inverse of $\boldsymbol{A}$. The components a_{11} and a_{22} of the $\boldsymbol{a}$ matrix can be obtained experimentally from

$$N_x = \frac{F}{w} \qquad \varepsilon_x = a_{11}N_x \tag{2.20}$$

$$N_y = \frac{F}{w} \qquad \varepsilon_y = a_{22}N_y \tag{2.21}$$

The $\boldsymbol{A}$ matrix can then be obtained by computing the inverse of the $\boldsymbol{a}$ matrix.

A four-point bending test was also performed. Figure 2.7 shows the bending setup. Three samples were tested for each direction. The distance between the outer supports was 35.6 mm, and the width of the samples was $w = 20$ mm.

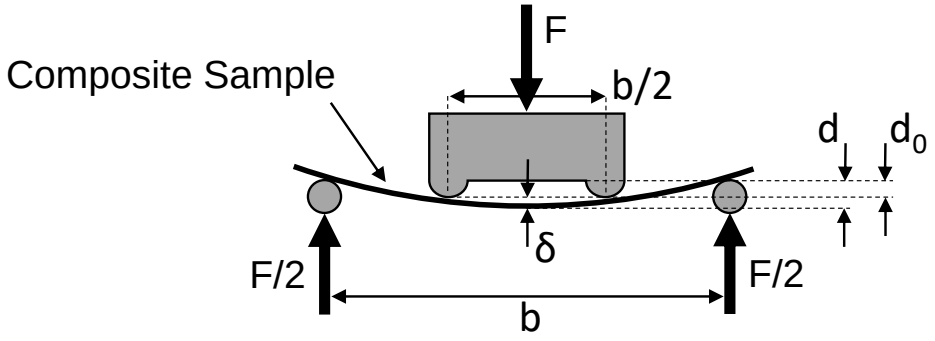

Figure 2.7: Four-point bending test setup.

From CLT, the constitutive equations are

$$M_x = D_{11}\kappa_x \qquad\qquad M_y = D_{22}\kappa_y \tag{2.22}$$

The moment stress resultants (moment per unit width) were obtained from

$$M_x = M_y = \frac{Fb}{8w} \tag{2.23}$$

The deflection at the center of the sample δ can be related to the curvature by considering a clamped beam of length $b/4$ under a bending moment $Fb/8$. Then, for the longitudinal bending

$$\delta = \frac{M_x(b/4)^2}{2D_{11}} = \frac{\kappa_x(b/4)^2}{2} \longrightarrow \kappa_x = \frac{32\delta}{b^2} \tag{2.24}$$

where

$$\delta = d - d_0 \tag{2.25}$$

with d_0 representing the initial value of d. Similar equations are obtained for a laminate loaded in the transverse direction y.

From the results of these experiments, it was observed that the CLT overestimate a_{11} by 13% and underestimates a_{22} by 15%. Therefore, these two elements of the $\boldsymbol{a}$ matrix were corrected accordingly and the $\boldsymbol{A}$ matrix was computed. It was also

observed that the CLT underestimates D_{11} and D_{22} by 8% and 6% respectively. Hence, the complete $\boldsymbol{D}$ matrix obtained from CLT was scaled up to correct the average error of 7%, as suggested in Sakovsky and Pellegrino, (2019). In summary, the flange laminate stiffness matrices are:

$$\boldsymbol{A} = \begin{bmatrix} 5432 & 619 & 0 \\ 619 & 942 & 0 \\ 0 & 0 & 737 \end{bmatrix} N/mm \tag{2.26}$$

$$\boldsymbol{D} = \begin{bmatrix} 1.076 & 0.482 & 0 \\ 0.482 & 0.781 & 0 \\ 0 & 0 & 0.459 \end{bmatrix} Nmm \tag{2.27}$$

For the web laminate, CLT was used to estimate the $\boldsymbol{A}$ and $\boldsymbol{D}$ matrices. Scaling of the $\boldsymbol{a}$ matrix was done in the same way as described for the flange laminate, decreasing a_{11} by 13% and increasing a_{22} by 15%. The $\boldsymbol{D}$ matrix was left unchanged. The corresponding stiffness matrices for the web are therefore:

$$\boldsymbol{A}_{web} = \begin{bmatrix} 11369 & 1512 & 0 \\ 1512 & 2269 & 0 \\ 0 & 0 & 1727 \end{bmatrix} N/mm \tag{2.28}$$

$$\boldsymbol{D}_{web} = \begin{bmatrix} 28.20 & 4.32 & 0 \\ 4.32 & 7.44 & 0 \\ 0 & 0 & 4.93 \end{bmatrix} Nmm \tag{2.29}$$

2.4 Coilable Structure Prototype Fabrication

Manufacturing was done in an autoclave using a two-cure process, where the flanges were first cured separately, then bonded together during a second cure cycle. The main steps are illustrated in Figure 2.8. First, the laminate is draped over two U-shape aluminum molds (Fig. 2.8a) to form the two flanges. Both parts are vacuum bagged together and autoclave cured. Then, a single ply of glass fiber plain weave, oriented at ±45° to the axis of the molds, is used to bond together the two flanges (Fig. 2.8b). This creates a 7-ply web region with stacking sequence $[\pm 45_{GFPW}/0_{CF}/\pm 45_{3,GFPW}/0_{CF}/\pm 45_{GFPW}]$. The two molds are clamped together using a series of bolts in order to apply adequate consolidation pressure on the web region (Fig. 2.8c). As all the bolts are situated below the laminate, shims are added

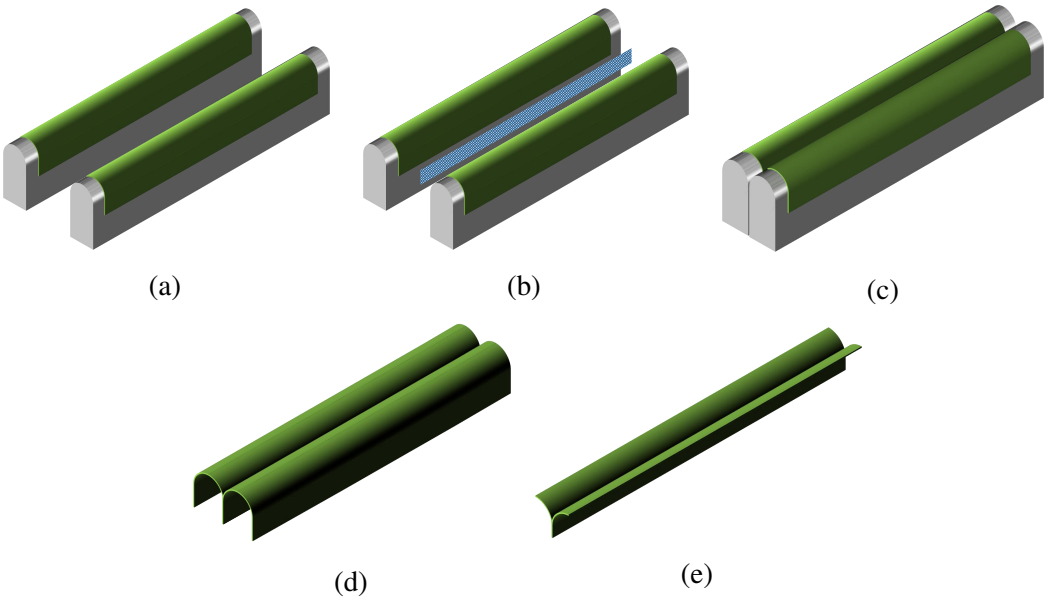

Figure 2.8: TRAC structure manufacturing process. Configuration for first cure, with two U-shape shells shown in green (a), addition of bonding ply, shown in blue (b), configuration for second cure (c), cured part (d), and final structure (e).

at the base of the mold to ensure the pressure is evenly distributed over the web region. A second autoclave cure is then performed to cure the bonding ply. Finally, the part is removed from the molds (Fig. 2.8d) and the excess material is cut to obtain the final part (Fig. 2.8e).

The mold geometry and final cutting step were designed to yield the nominal geometric parameters for the TRAC structure: $r = 12.7$ mm, $\theta_f = 90°$ and $w = 8$ mm. However, due to cure-related residual stresses, the actual shape of the resulting prototypes differs significantly. Section 2.5 describes how an accurate measurement of the shape is obtained. For the current study, shape variations are not a concern, but one could use a post-cure cycle to partially release residual stresses. Samples with length up to 1.6 m were manufactured using this method.

2.5 TRAC Structure Characterization

As mentioned in Section 2.4, the shape of the TRAC structures changes after removal from the mold. Accurate measurements of the actual shape of each sample were done using a Faro Arm (Edge 14000) with a 3D laser scanner attachment (ScanArm HD).

For this measurement, the samples are supported at each end to remove any global twist. A point cloud was generated using the CAM2 Measure 10 software. A Matlab

script was created to extract, from the point cloud thus obtained, the cross-section geometry (flange radius and opening angle) at multiple (10) locations along the length of a TRAC structure. The data processing is done in four steps:

1. The data points are split into two regions, one for each flange (including the web region). Because the 3D scanner measures the surface, the web region is represented by two similar surfaces offset by the web thickness, thus allowing the whole structure to be represented by two surfaces having a constant thickness.

2. For each flange, the best fit circle is computed, and the flange radius r and opening angle θ_f are extracted.

3. A known function is fitted to each flange. To ensure the functions are well-defined, each flange is rotated 45° (−45° for the left flange, 45° for the right flange). The full cross-section is then discretized in small length segments (∼ 20000) and the flanges are rotated back to their initial orientation.

4. The centroid location, the second moments of area, the orientation of the principal axes and the twist and camber along the length of the sample are computed using numerical integration. The camber is defined as the distance between the centroid of the cross-section at each location and a straight line connecting the centroids at each end.

For the third step, a 6th order Fourier series, defined as:

$$y = a_0 + \sum_{n=1}^{6} \left(a_n \cos\left(\frac{2\pi n x}{P}\right) + b_n \sin\left(\frac{2\pi n x}{P}\right)\right) \tag{2.30}$$

was found to accurately reproduce the shape of each flange. In this equation, P is defined as $(\max(x) - \min(x))$.

Figure 2.9 shows an example result, obtained for the sample 1 in Chapter 3. Figure 2.9a shows the experimental data for all ten profiles along the length of a 600 mm long sample, superimposed on a single plot. Figure 2.9b shows a single profile, located at $Z = 460$ mm. The circle fits for both flanges are plotted on top of the experimental data, and the linear fit for the web is also shown. Figure 2.9c shows the Fourier series superimposed over the experimental data, and Figure 2.9d shows only the Fourier series fit, with the centroid marked as a red cross. In Figure 2.9d, the section has been translated such that the centroid is located at (0,0).

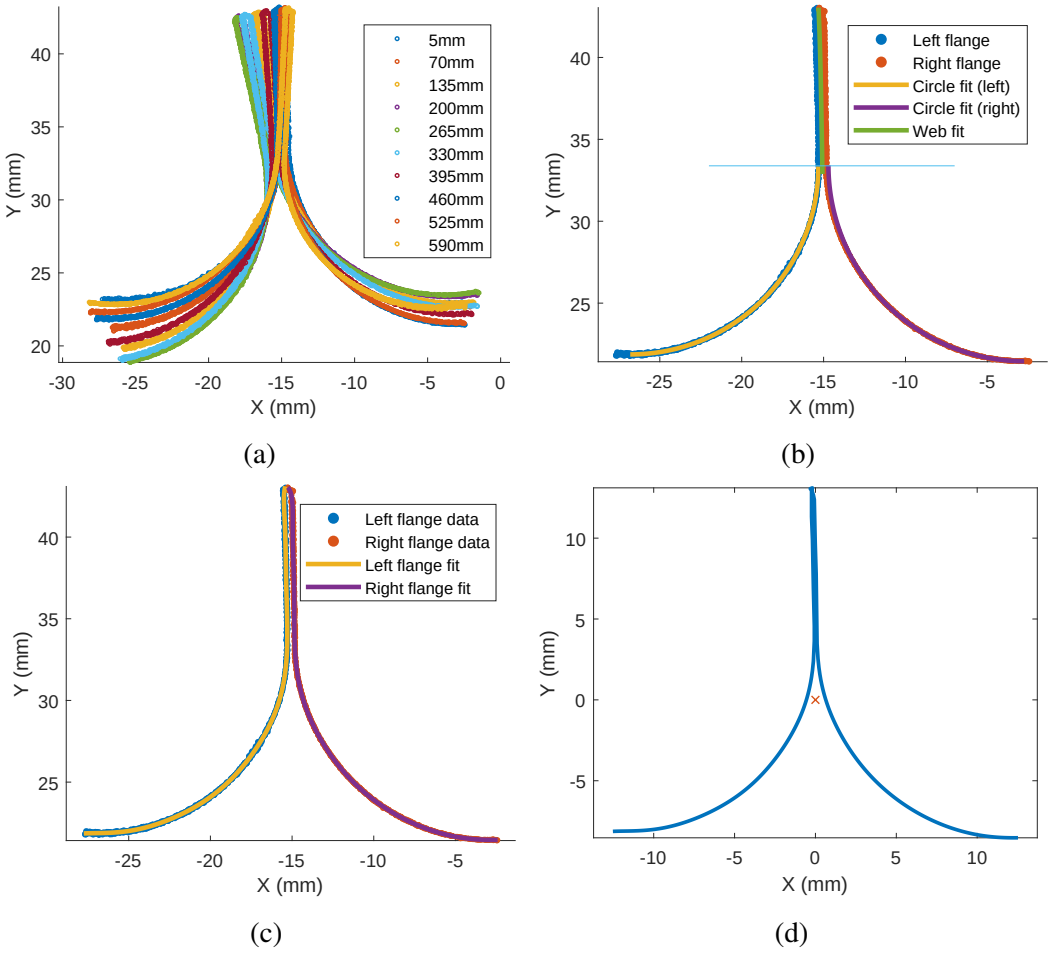

Figure 2.9: Example of the data obtained from the shape post-processing (sample 1 from Chapter 3). (a) Ten cross-sections along the full length of the structure, superimposed. (b) Cross-section at $Z = 460\,\text{mm}$, with experimental data (red and blue), flange circle fits (yellow and purple), and linear fit for the web (green). The horizontal line marks the start of the web. (c) Cross-section at $Z = 460\,\text{mm}$, with experimental data (red and blue) and Fourier series fit (yellow and purple). (d) Analytical function and centroid location (red cross) of the cross-section at $Z = 460\,\text{mm}$.

The camber and twist along the length of the structure are shown in Figure 2.10. The twist is computed as the rotation of the web region. For this specific sample, the maximum camber is $-0.8\,\text{mm}$, while the maximum twist is $-10°$.

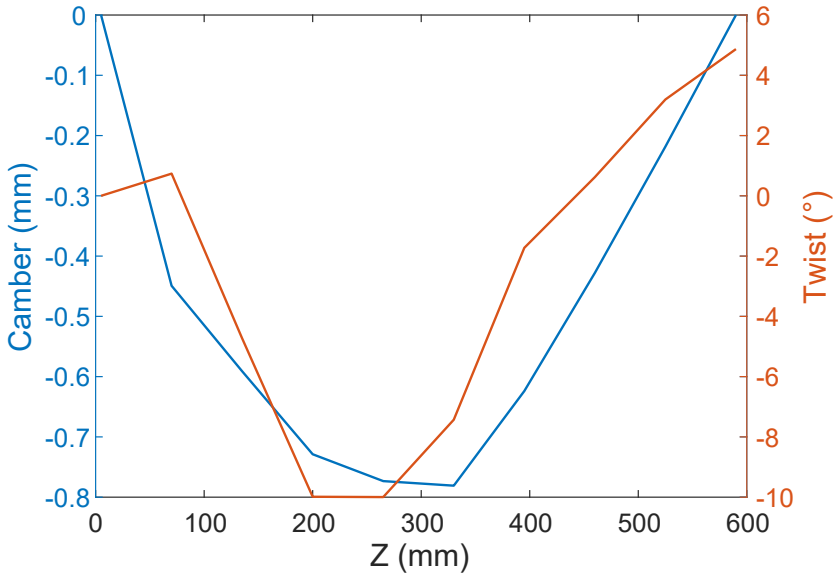

Figure 2.10: Example of camber (in blue) and twist (in red) along the length of a TRAC structure (sample 1 from Chapter 3).

Chapter 3

NONLINEAR BEHAVIOR IN THE DEPLOYED CONFIGURATION

3.1 Introduction

The behavior of ultra-thin TRAC structures in their deployed configuration is investigated in this chapter. During operation, the loads applied on these coilable structures and their boundary conditions depend on the structural architecture. While in most cases the loading conditions will be a combination of multiple type of loads, the present research focuses independently on two typical loading conditions: pure bending and torsion.

In previous research on the bending behavior of TRAC booms, localized buckling was observed to be the main structural failure mode for a deployed boom loaded under pure moment (Murphey, Turse, and Adams, 2017). Banik and Murphey, (2010) showed that nonlinear finite element analysis can accurately predict the behavior under bending for booms that are relatively thick ($t \approx 1$ mm). Bessa and Pellegrino, (2017) studied numerically the behavior of ultra-thin ($t < 100\,\mu$m) TRAC booms under pure bending and showed how to optimize the cross-section to reduce the effect of shape imperfections on the ultimate buckling load. In both of these previous studies, rather short booms were considered (0.6 m and 0.5 m respectively). Murphey, Turse, and Adams, (2017) also studied the torsional behavior of TRAC booms, showing that the response is highly nonlinear and depends on the boundary conditions.

The current chapter contains three sections following this introduction. First, the bending behavior is studied both experimentally and numerically. The effect of varying the length up to 5 m is also investigated. Then, the torsional behavior is studied, again through a combination of both experiments and numerical simulations. Finally, a conclusion summarizes and discusses the main findings.

3.2 TRAC Structure Behavior under Pure Bending

Buckling of thin-shell structures is sensitive to both material properties and geometrical imperfections. Therefore, buckling of TRAC structures under pure bending

was first studied experimentally. Then, a simulation model was developed to predict the bending behavior, and validated by comparing with experimental results. Finally, the numerical model was used to predict the buckling moment of structures with lengths varying from 0.3 to 5 m.

3.2.1 Experiments

Experimental Setup

The experimental test setup used for the bending experiments is shown in Figure 3.1. The samples were potted at each end with epoxy in acrylic plates with laser-cut thin slits following the cross-section of each specific test sample. This ensured that the cross-section of the thin-shell was not distorted near the ends prior to testing, and aligned the centroid of the cross-section with the rotation axis of the testing machine.

The rotation at each end was independently controlled by a worm drive. A calibrated camera (8 MP camera of an iPhone 6, calibrated with the Matlab Camera Calibrator) installed above the setup tracked four targets installed on two rigid rods, to magnify the rotation at each end. The rotations were measured from images using a Matlab script. The sample was mounted on hollow shafts instrumented with strain gauges to measure the moment at both ends using a Vishay P3 strain amplifier. The longitudinal translation of one end was not constrained, allowing the sample to shorten due to large bending deformations.

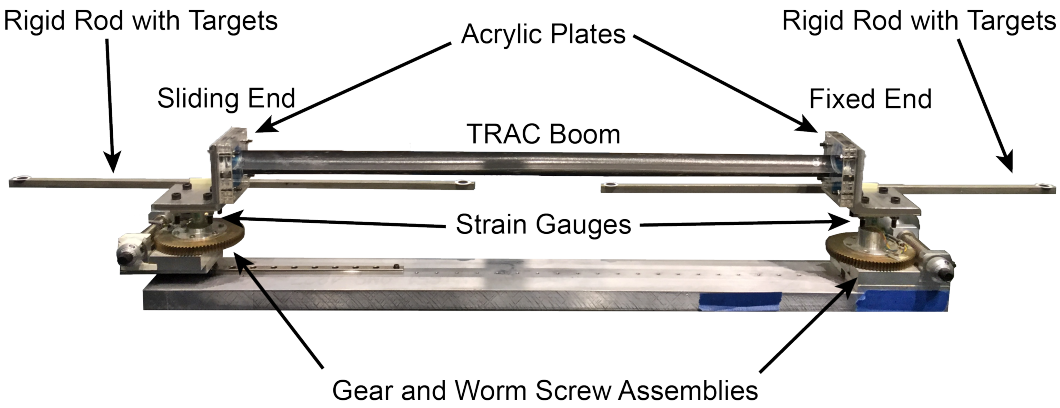

Figure 3.1: Bending experimental setup. The sliding end is mounted on a rail to allow longitudinal translation.

To perform a bending test, the end rotations were increased in small steps, keeping the moments equal in order to ensure a pure moment loading. Once the ultimate buckling has been reached, the measured moments dropped significantly, and were usually

different at the two ends, meaning that the sample had buckled asymmetrically and was not loaded under pure bending anymore.

Each sample was tested in bending around both axes, X and Y. In the case of bending around X, the TRAC cross-section is not symmetric. Positive moments cause the web to be in compression, while negative moments cause it to be in tension. Bending around Y is nominally symmetric.

Experimental results

Three different samples were tested. They were cut such that their free length between the end plates was 575 mm. The measurement procedure described in Section 2.5 was used to extract the geometry of each sample. Table 3.1 summarizes the dimensions of each sample.

Table 3.1: Average measured cross-section geometry for each experimental sample.

	r [mm]	θ_f [°]	w [mm]	Y_C [mm]
Sample 1 (V4-3A-1)	11.8	91.3	8	-4.1
Sample 2 (V4-3A-2)	11.9	88.5	8	-4.2
Sample 3 (V4-4A-2)	11.5	95.7	8	-4.1

The three samples behaved consistently. Therefore, only the results for the first sample are presented herein. Bending tests were performed three times in each of the four directions ($\pm X$, $\pm Y$) up to ultimate buckling. In all cases, two regimes were observed. The first regime is a linear pre-buckling phase until the first buckling event. This first buckling load is also referred as the critical moment. The second regime, following the initial buckling event, is a stable post-buckling phase until the ultimate buckling occurred. A loading-unloading test was also performed for each axis of bending, without reaching ultimate buckling.

The experimental results are shown in Figures 3.2 and 3.3. These plots show the measured moment as a function of the total rotation angle. The experiment was repeated three times, and overall, the behavior under pure bending is repeatable. Not only the responses are mostly indistinguishable, with an average variation of the angle for a given moment of 0.04°, but more importantly the same buckling events (as described in the next paragraphs) were observed at the same loads and locations.

For X bending, the overall deviation in the ultimate buckling moment was 5%. Furthermore, the behavior was consistent between loading and unloading. Devi-

ation between loading and unloading was only observed when a negative moment was applied, close to the ultimate buckling. For Y bending, the deviation in ultimate buckling loads was 10%. In the case of a negative moment, tests 2 and 3 captured some unstable behavior at rotations larger than 3°, while test 1 directly underwent ultimate buckling. Very little difference was observed between loading and unloading.

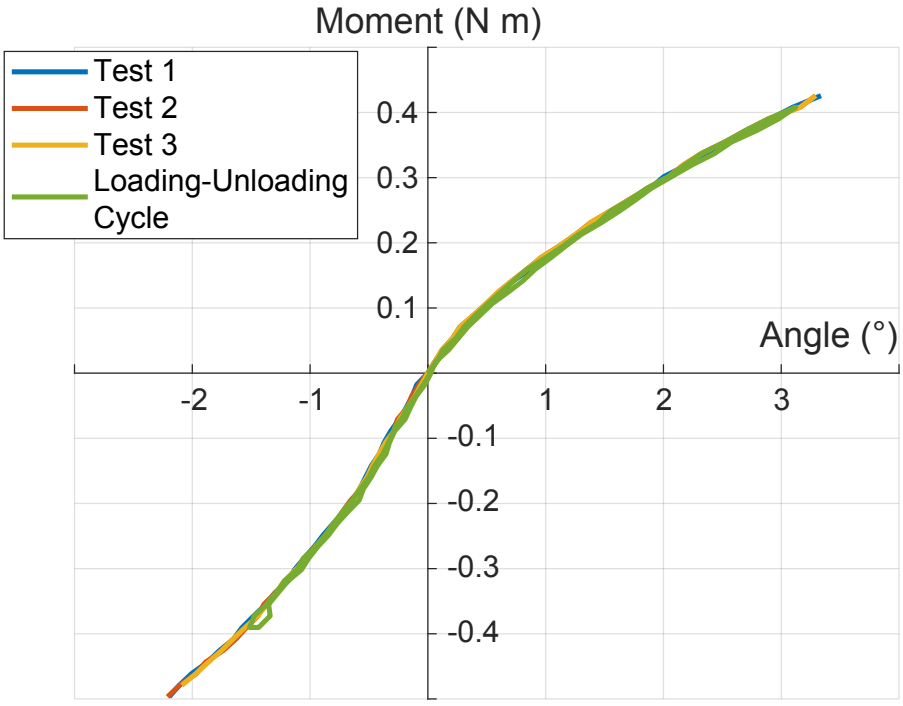

Figure 3.2: Experimental moment rotation results for sample 1 under X bending.

Figure 3.4 shows photos of the buckling modes observed in the experiments on a sample subjected to bending around the X axis. When the structure is loaded by a *positive* moment, the web is under compression. Beyond the critical moment (about 0.1 N m), the web starts to buckle globally in a wave pattern, with a wavelength of 1/4 of the total length. This reduces the effective stiffness of the structure and a softening of about 45% can be observed in the moment-angle plot. Subsequently increasing the moment increases the amplitude of the web waviness, until the deformation localizes (always at the same location, 90 mm from the fixed end) and ultimate buckling occurs. The maximum moment for this load case is 0.43 N m. Overall, two regimes were observed: pre-buckling, followed by a first buckling event, and stable post-buckling, followed by ultimate buckling.

The behavior of the structure loaded by a *negative* X moment has the same two

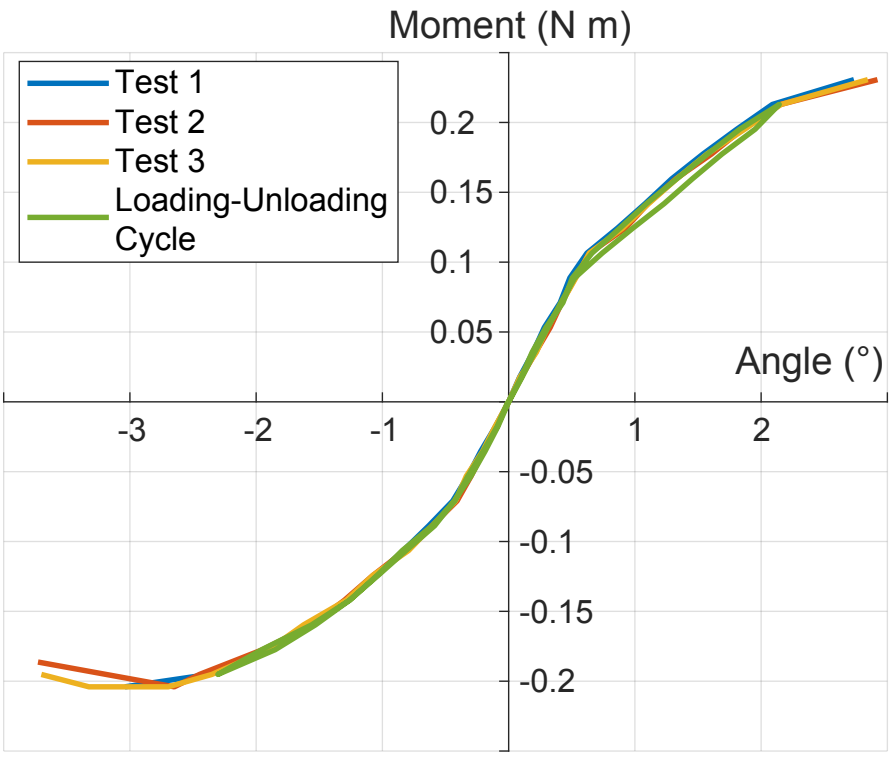

Figure 3.3: Experimental moment rotation results for sample 1 under Y bending.

regimes, but is different otherwise as in this case the flanges are under compression. At a critical moment of about $-0.21\,\mathrm{N\,m}$, a small localized buckle appears on one flange, quickly followed by another on the other flange. These buckles lead to a softening of about 40%, as shown in Figure 3.4. At a load of $-0.4\,\mathrm{N\,m}$, the buckle on one flange moves longitudinally 20 mm toward the closest end of the structure. However, this displacement occurs at a different load (about $-0.35\,\mathrm{N\,m}$) during unloading, explaining the difference between loading and unloading observed in Figure 3.2. Ultimate buckling occurs when a torsional instability forces one buckle to flatten transversally and form a kink at the junction of the flange with the web. The maximum moment for this load case is $-0.5\,\mathrm{N\,m}$.

Figure 3.5 shows the buckling modes observed in the experiments when the TRAC structure is loaded by a moment around the Y axis. As the behavior is nominally symmetric, only the behavior under positive moments will be discussed. Since the inner flange is under compression, the buckling modes are similar to the $-X$ case. First, there is a mostly linear pre-buckling regime. Then, at critical moment of about $0.1\,\mathrm{N\,m}$, a small localized buckle appears in the compression flange, which reduces the effective stiffness of the structure by about 60%. In the stable post-buckling

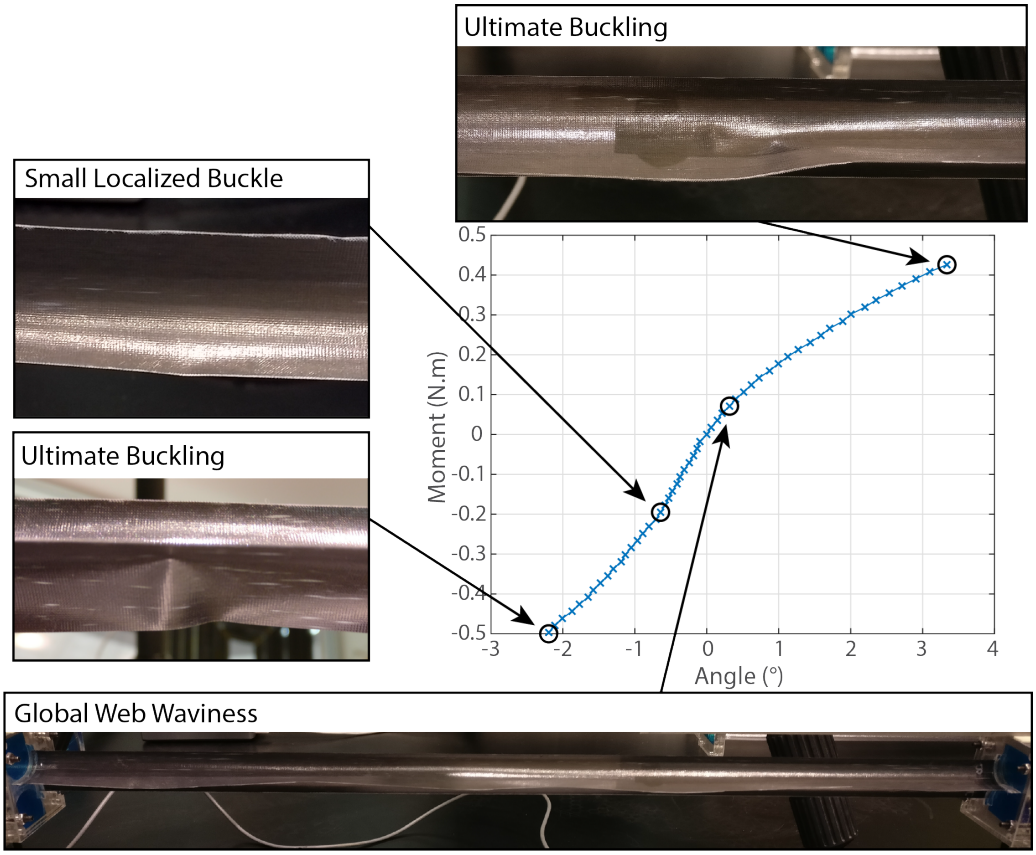

Figure 3.4: Buckling modes for X bending under positive and negative moments.

regime, the buckle slowly increases in amplitude until the flange flattens and forms a kink at the root of the web. Ultimate buckling occurs at a load of 0.23 N m, 180 mm from the sliding end of the sample. Comparing Figures 3.4 and 3.5, the ultimate buckling mode for moments around Y appears identical to the ultimate buckling mode for negative moments around X.

In summary, initial buckling of ultra-thin TRAC structures under pure bending loading occurs when small localized buckles appear, reducing the effective bending stiffness. This is followed by a stable post-buckling regime, where the structure is able to withstand moments as high as four times the initial buckling moments. In both of these regimes there is almost no difference between loading and unloading behavior.

3.2.2 Finite Element Simulations

A finite element model, shown in Figure 3.6, was built in Abaqus/Standard 2018 to predict and better understand the behavior of ultra-thin TRAC structures when subjected to pure bending. The structure is modeled using 4-node shell elements

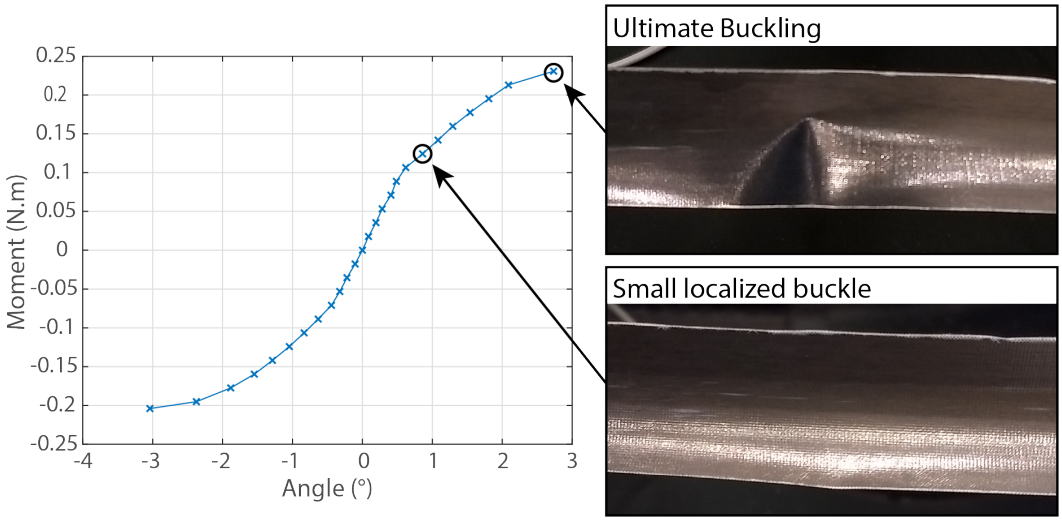

Figure 3.5: Buckling modes for *Y* bending under positive moments.

with reduced integration (S4R). A uniform mesh is used with element size of 2 mm, corresponding to 20 elements across each flange and 4 elements across the web. The material properties are defined in the form of a general stiffness matrix based on the properties given in Section 2.3.

	Degrees of Freedom at End 2					
	T_X	T_Y	T_Z	R_X	R_Y	R_Z
X Bending	Free	0	Free	Free	0	0
Y Bending	0	Free	Free	0	Free	0

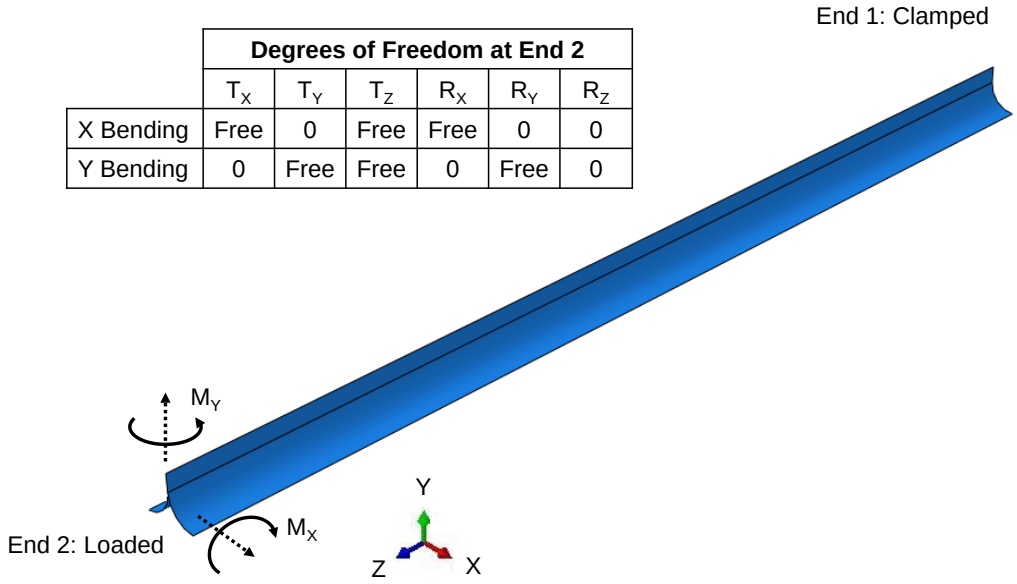

Figure 3.6: Finite element model for TRAC structure bending, with boundary conditions (T = translation, R = rotation) and applied moments.

At both ends of the structure, all the nodes forming the cross-section are coupled to a reference point using a kinematic coupling, effectively creating a rigid cross-section, matching the experimental setup. All six degrees of freedom of the reference point

at end 1 are restricted, making it effectively clamped. At the other end, a pure moment load is applied at the reference point. In the case of a moment around the X axis, the translational degrees of freedom along Y and Z as well as the rotational degree of freedom around X are kept free, while the other three degrees of freedom are fixed. In the case of moments around the Y axis, the same boundary conditions are used, only inverting X and Y.

While these boundary conditions do not match kinematically the experimental setup, in both cases the resulting loading condition on the structure is a pure moment, making them statically equivalent. Furthermore, a comparison was made between the model described above and a different model that matches exactly the boundary conditions of the experiments, and it was observed that they both predict the same buckling load. For this reason, the simpler model, where the applied moment and the resulting rotation are extracted at a single point, was preferred.

The analysis procedure consists of 4 steps and is similar to the procedure presented in Bessa and Pellegrino, (2017):

1. A preliminary buckling prediction (eigenvalue) is performed starting from the undeformed configuration (*linear buckling prediction*).

2. An implicit, nonlinear static analysis is then performed, starting from the undeformed configuration until buckling occurs, at which point convergence is not attained. This buckling load can be lower or higher than the previous, linear prediction. The goal of this step is to compute the deformed geometry just before buckling.

3. A new linear buckling prediction is performed in the deformed configuration, using the results from the previous step. An iterative process is used to find the last increment at which the buckling prediction could be obtained, as the nonlinear analysis can sometimes converge for a few increments in the post-buckling regime. Combining the applied load to reach this deformed configuration and the new predicted buckling load gives the *nonlinear buckling prediction*.

4. Simulation of the post-buckling regime is performed using an arc-length method (modified Riks method (Crisfield, 1981)), where a geometric imperfection based on the first buckling mode found in step 3 is introduced in the initial geometry. For this study, an amplitude of 20% of the flange thickness

(16 μm) was sufficient to trigger the post-buckling regime without changing the pre-buckling behavior.

Similarly to the experiments, three loading conditions were studied numerically. Figure 3.7 shows, for a structure with the nominal cross-section and a length of 500 mm, the different buckling modes obtained for the linear and nonlinear buckling predictions, as well as the post-buckling shape, for each loading condition. The following can be observed. First, when a positive moment around X is applied (web under compression), both the linear (fig. 3.7a) and nonlinear (fig. 3.7b) buckling involve a global wave pattern in the web and are in close agreement. In the post-buckling regime (fig. 3.7c), a localization of the deformation is observed.

Second, when a negative moment around X is applied (flanges under compression), linear buckling (fig. 3.7d) predicts a global wave pattern on both flanges. The nonlinear analysis (fig. 3.7e) predicts localized buckling close to both ends, and the post-buckling shape (fig. 3.7f) displays two kinks on each flange, also close to both ends.

Finally, in the case of a moment applied around Y, the linear prediction (fig. 3.7g) is a global wave pattern on the flange loaded in compression. For the nonlinear buckling (fig. 3.7h), the deformation is localized in the middle of the structure. In the post-buckling regime (fig. 3.7i), a kink forms in the middle.

3.2.3 Comparison with Experiments

To validate the numerical model presented in the previous section, simulations of the samples tested experimentally were done. The cross-section in the model was adjusted to match each sample using the measured dimensions in Table 3.1. For all three samples, a similar agreement between experiments and their respective simulation was observed, so only results for sample TRAC V4-3A-1 are presented in this paper.

Figures 3.8 and 3.9 show moment-angle plots comparing experimental results and simulations for bending around X and Y, respectively. In both cases, the pre-buckling stiffness is well predicted by the simulations. For negative moment around X (web in tension), the simulations did not converge in the post-buckling regime. However, the initial buckling load from the simulation ($-0.25\,\mathrm{N\,m}$) matches relatively well with the first appearance of small localized buckles in the experiments ($-0.21\,\mathrm{N\,m}$).

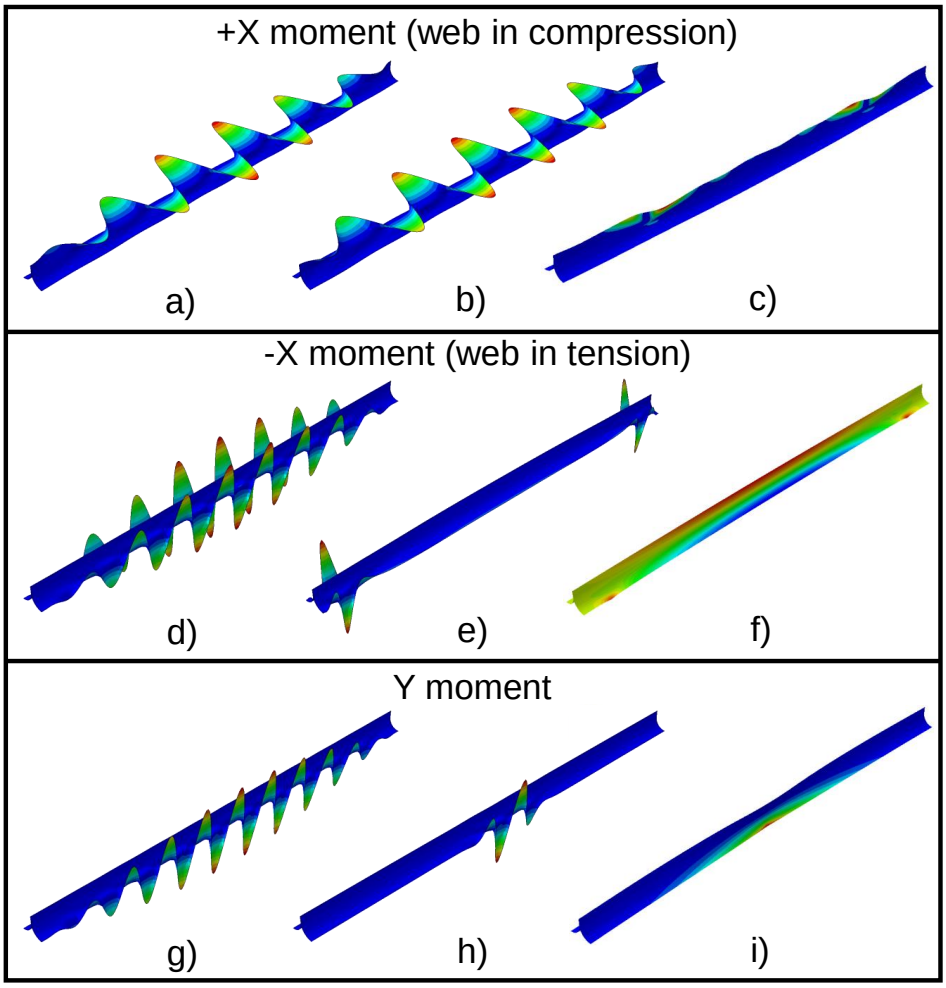

Figure 3.7: Buckling modes from finite element simulations. $+X$ moment: linear buckling (a), nonlinear buckling (b), post-buckling (c). $-X$ moment: linear buckling (d), nonlinear buckling (e), post-buckling (f). Y moment: linear buckling (g), nonlinear buckling (h), post-buckling (i).

In the case of a positive bending moment around X (web is compression), the stable post-buckling regime is well captured in the simulation. The softening observed in the experiments, due to the web undergoing global buckling, is also seen in the numerical results. Furthermore, the ultimate buckling from the simulation (0.5 N m) is fairly close to the experimental value (0.43 N m). The main difference between these two results is that, while the simulation shows a clear transition from the pre-buckling regime to the post-buckling regime, this transition is more gradual in the experiments. This can be seen in Figure 3.8, where the numerical results display a localized change of slope, while the experimental results show a smooth transition.

In the case of a bending moment around the Y axis, the simulation predicts well both

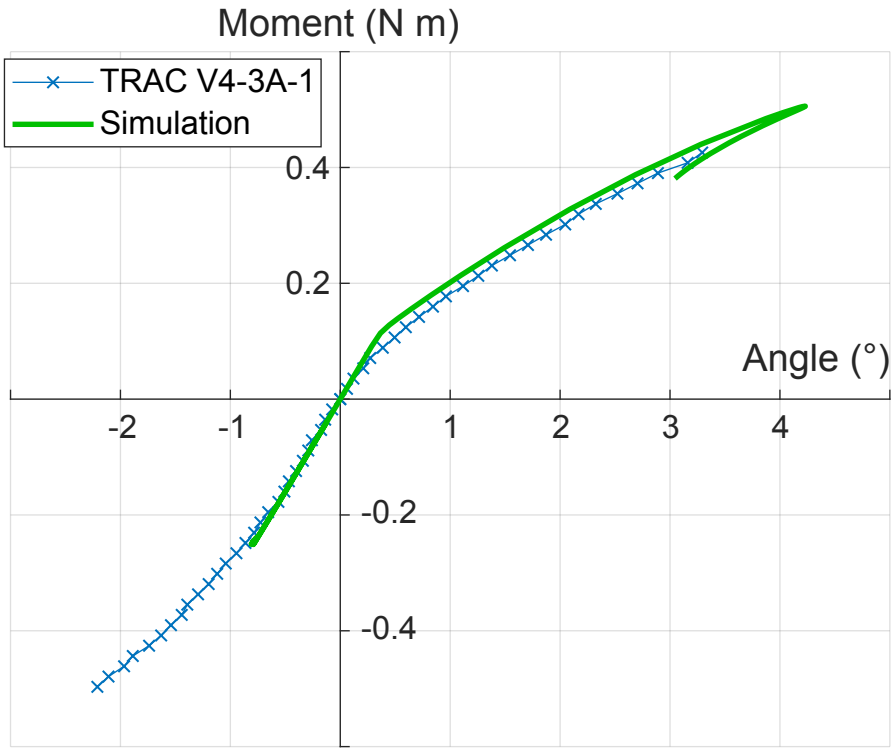

Figure 3.8: Comparison of simulation and experiment for sample 1 under X bending.

the pre-buckling and stable post-buckling stiffnesses. A key aspect of the numerical results is a sudden drop in both moment and rotation following the initial buckling, before transitioning to a stable post-buckling regime. This unstable region is not seen in the experiments, but the buckling load from the simulation (0.1 N m) matches very well with the observed appearance of a small localized buckle during the experiment (0.11 N m). Due to multiple bifurcations encountered during the simulation of the post-buckling behavior, the current numerical results do not predict the ultimate buckling load as convergence is challenging to obtain at each of these bifurcations. The end of the simulation curve marks the point where convergence was no longer obtained. A different numerical technique, such as the *generalized path-following*, would be necessary to fully capture the complete post-buckling regime (Eriksson, 1998; Groh, Avitabile, and Pirrera, 2018).

3.2.4 Effect of Length on Buckling Load

Due to the wide range of applications of TRAC structures, the same cross-section could be used for a large range of lengths. Therefore, an understanding of how the initial buckling load of these structures varies with their length is important. Hence, the simulation framework presented in Section 3.2.2 can be used to investigate this

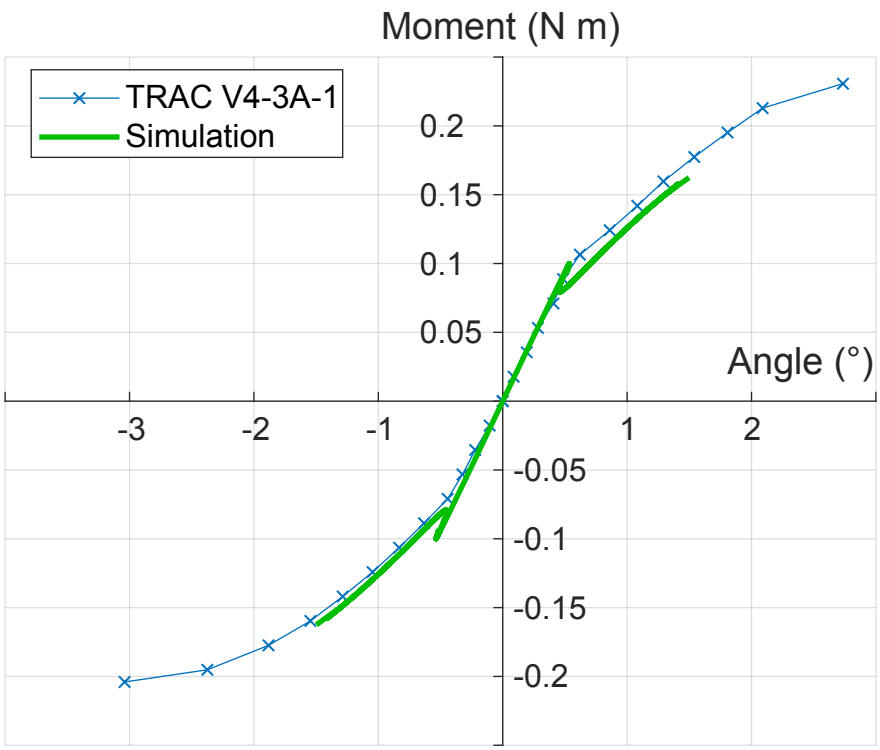

Figure 3.9: Comparison of simulation and experiment for sample 1 under Y bending.

behavior.

For this study, the buckling loads of structures with the nominal cross-section in Table 3.1 and lengths varying from 0.3 m to 5 m was obtained numerically. Both the linear (step 1 in Section 3.2.2) and the nonlinear predictions (step 3) were obtained. Figure 3.10 shows the buckling moment as a function of the structure length for each loading condition.

The first loading case is a negative moment applied around the X axis, compressing both flanges. The plot of the buckling moment (both linear and nonlinear) as a function of length is shown in Figure 3.10a. For the linear prediction, two regimes are observed. For a length smaller than 700 mm, the buckling mode is a global wave pattern on both flanges (Figure 3.11a.1), with a uniform wavelength of about 52 mm. For this length range, the buckling load is constant with length. Increasing the length beyond 700 mm leads to a different, lateral-torsional buckling mode (Figure 3.11a.2). In this case, the buckling load decreases with length. Lateral-torsional buckling is often observed in thin-walled open cross-section beams (Bazant and Cedolin, 2010). The nonlinear results show three regimes. First, for lengths up to 1000 mm, the buckling mode is localized close to both ends (Figure 3.11b.1). At

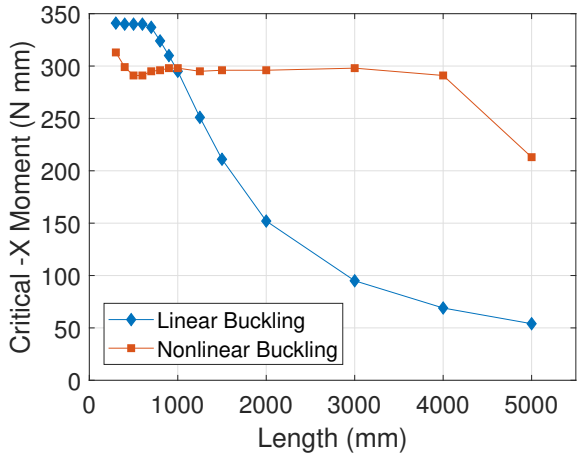

(a)

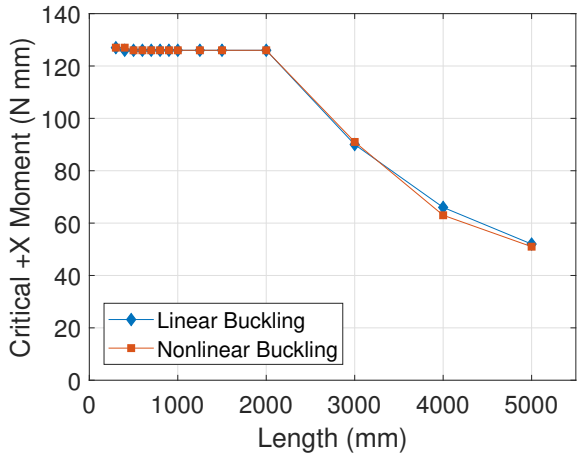

(b)

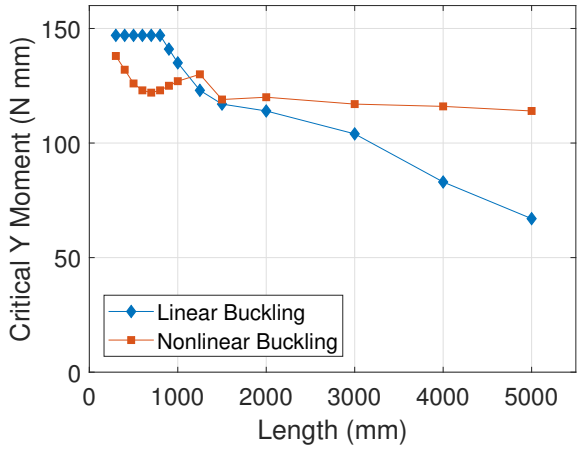

(c)

Figure 3.10: Critical moment as a function of structure length, both linear and nonlinear predictions, for $-X$ bending (a), $+X$ bending (b), and Y bending (c).

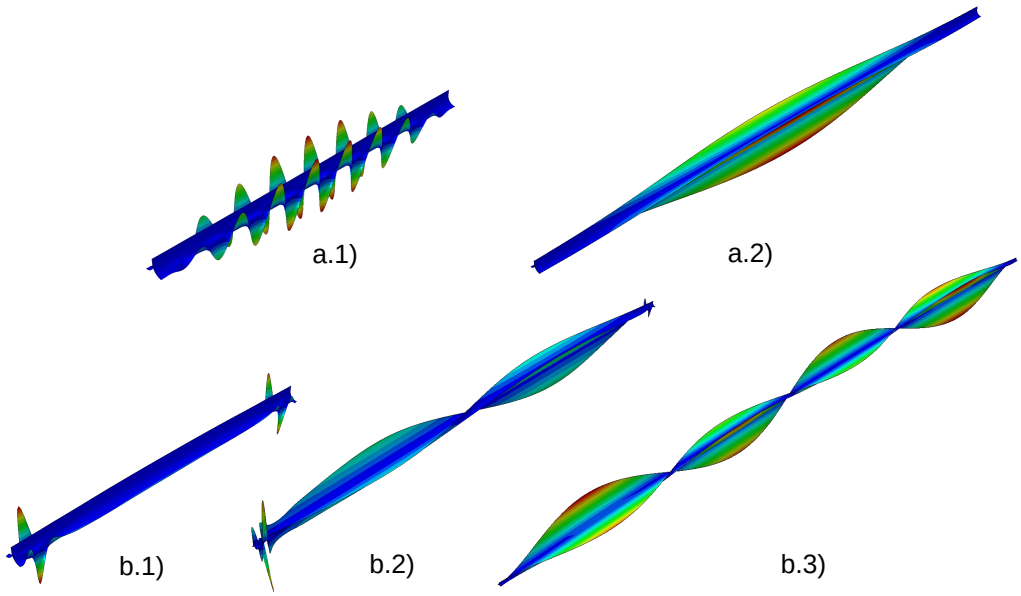

Figure 3.11: Buckling modes from simulation for $-X$ bending. Linear buckling, lengths of 500 mm (a.1) and 1250 mm (a.2). Nonlinear buckling, lengths of 500 mm (b.1), 2000 mm (b.2) and 5000 mm (b.3).

the opposite end of the spectrum, for a length of 5000 mm, buckling occurs with a lateral-torsional mode, but with a shorter wavelength (Figure 3.11b.3) than in the linear prediction. Finally, for lengths between 1000 mm and 5000 mm, the buckling mode is a combination of the two mentioned previously, as seen in Figure 3.11b.2. In this regime, the buckling moment is mostly constant, decreasing only by 3% when the length is increased from 1000 mm to 4000 mm.

The second loading case is when a positive moment is applied around the X axis, compressing the web. The plot of the buckling load as a function of length is shown in Figure 3.10b. For this loading condition, the linear and nonlinear buckling predictions practically coincide for the full range of lengths. Two regimes are observed. First, for lengths varying from 300 mm to 2000 mm, the buckling load is constant. The buckling mode (Figure 3.12a) is a global wave pattern with a wavelength of about 77 mm (13 half-wavelengths for a 500 mm structure), and this wavelength remains constant when the length is increased. The second regime, for lengths above 2000 mm, is once again a lateral-torsional mode (Figure 3.12b). However, in contrast with what was observed for a negative X moment, both the linear and nonlinear results predict a single wave, with the buckling moment decreasing with length.

The last loading case is a moment applied around the Y axis. The plot of the buckling

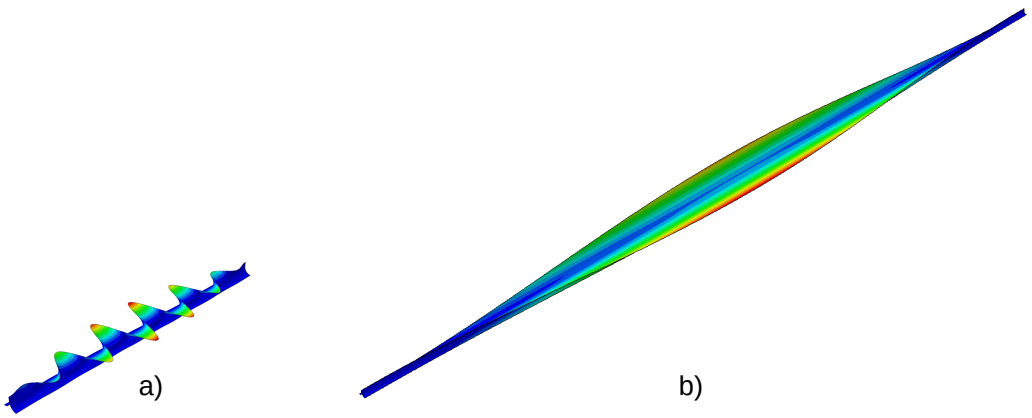

Figure 3.12: Buckling modes from simulation for $+X$ bending. Linear and nonlinear buckling, lengths of 500 mm (a) and 3000 mm (b).

load as a function of length is shown in Figure 3.10c. Similarly to the other two cases, the linear prediction consists of two regimes. The critical moment is constant for lengths ranging from 300 mm to 800 mm, where the buckling mode is a wave pattern in the inner flange (Figure 3.13a.1), with a uniform wavelength, constant with load, of 45 mm. Lateral-torsional buckling is observed for lengths above 800 mm (Figure 3.13a.2), and the critical moment decreases with length. The nonlinear buckling response is also similar to what was observed for the negative moment around X, with three regimes. First, for lengths varying from 300 mm to 1000 mm, the buckling mode is localized in the middle of the flange (Figure 3.13b.1) and the buckling load is relatively constant. For lengths above 2000 mm, the buckling mode is once again lateral-torsional with shorter wavelength (3 full waves at a length of 3000 mm, Figure 3.13b.2). In the range 1000-2000 mm, both modes are competing. The result is that the nonlinear simulation predicts a mostly constant critical moment over the full range of lengths, with the load decreasing by only 10% when the length increases from 1000 mm to 5000 mm.

While the linear buckling simulation (and also the nonlinear simulation in the case of a positive X moment) predicts a typical buckling behavior for a thin-shell structure, with first a region of constant load followed by a region where the load decreases with length, the nonlinear results for ultra-thin TRAC structures are more interesting. The main feature is that for both negative X moments and Y moments, the critical buckling load is almost constant with length. This phenomenon can be explained by nonlinear deformations during the pre-buckling phase. Bending around Y will be used as an example. As shown in Figure 3.9, the first buckling event

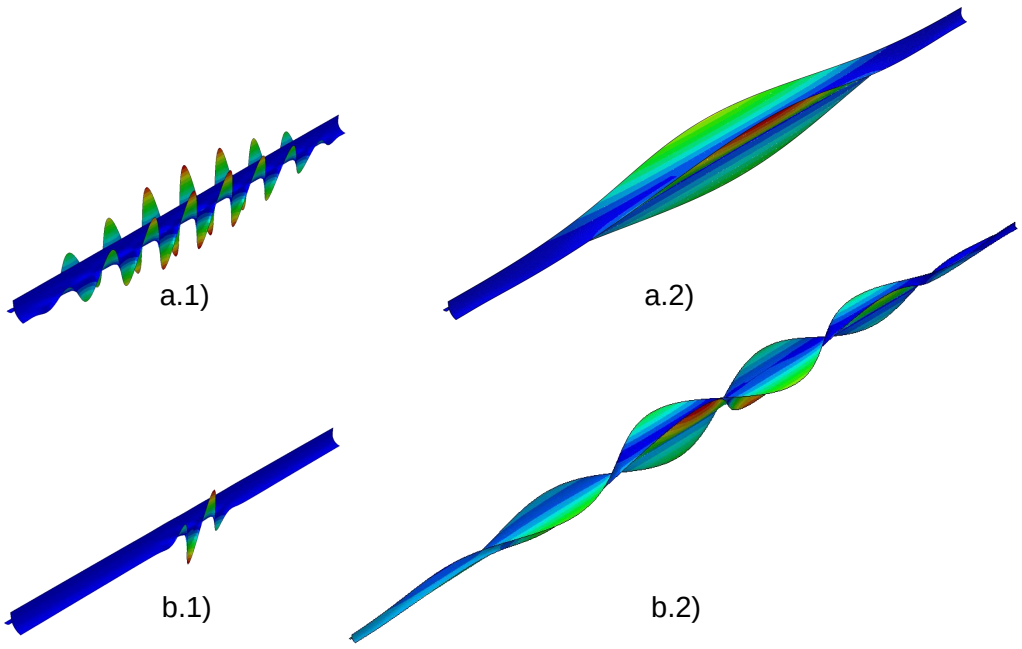

Figure 3.13: Buckling modes from simulation for Y bending. Linear buckling, lengths of 500 mm (a.1) and 1000 mm (a.2). Nonlinear buckling, lengths of 500 mm (b.1) and 3000 mm (b.2).

follows a seemingly linear phase. However, while the global structural behavior is linear in this region, nonlinear deformations occur locally in the structure. Figure 3.14 illustrates the deformation (magnified by a factor of 4) of a 3000 mm long TRAC structure loaded around Y. The critical moment for this case is 117 N mm. At a load of 23 N mm, the inner flange has deflected down along the full length. This deformation pattern remains mostly unchanged for larger loads. For example, when a load of 90 N mm is reached, there is some torsional deformation, where the inner flange moves down close to the ends, but not in the middle. Finally, when the load approaches the buckling load, the torsional deformation decreases in wavelength, as shown in Figure 3.14 for an applied moment of 115 N mm. This nonlinear torsional deformation prior to buckling constrains the buckling mode to a higher order lateral-torsional mode, leading to a mostly constant critical moment, regardless of the length.

3.3 TRAC Structure Behavior under Torsion

Due to its thin-shell open cross-section, the TRAC structure has a very low torsional stiffness and can undergo large torsional deformation. Therefore, it is important to characterize the response of a structure when it is subjected to a torque, as could be

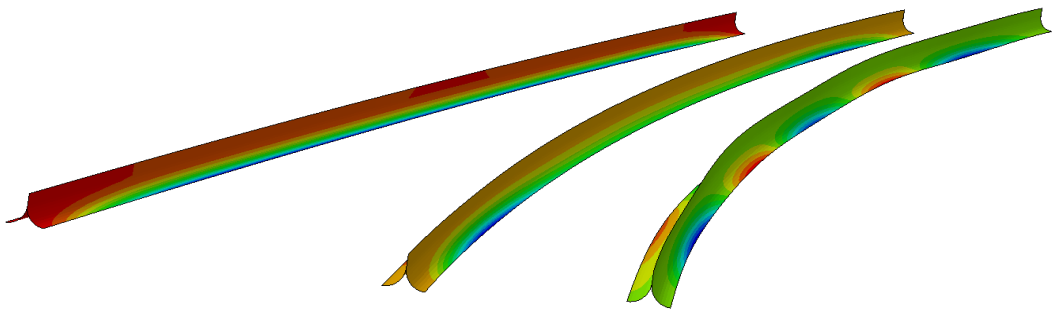

Figure 3.14: Nonlinear deformation in the pre-buckling regime during Y bending of a 3000 mm long structure. The color contour represents the displacement in the Y axis, where blue is negative (down) and red is positive (up). Displacements have been amplified by a factor of 4.

the case for example when loaded with an eccentric transverse force. In this section, the torsional behavior is first studied experimentally and numerically. Then, the results are compared and discussed.

3.3.1 Experimental Setup

An experimental setup to study the torsional behavior of thin-shell structures is shown in Figure 3.15. The rotation was driven using a gearbox with a 60:1 reduction ratio (Ondrive P30-60) and the twist angle was measured using a turns-counting dial, resulting in a resolution of 0.06°. At the other end, the structure was rigidly attached to a 6-axis load cell (ATI Nano 17 force/torque sensor). All force and moments components were measured during the installation of the sample to prevent any initial loads. Shims were added as needed to ensure all forces and moments were zero prior to the start of the experiment. The end of the structure attached to the load cell was mounted on a longitudinal low friction guide rail to allow the structure to shorten axially during the tests.

The same samples used for bending stiffness were studied with this setup, as the acrylic plates for each sample were designed such that the centroid location Y_C of the cross-section at each end was aligned with the rotation axis of the experimental setup. Only one sample, Sample 1 from Table 3.1, was tested to investigate the torsional behavior.

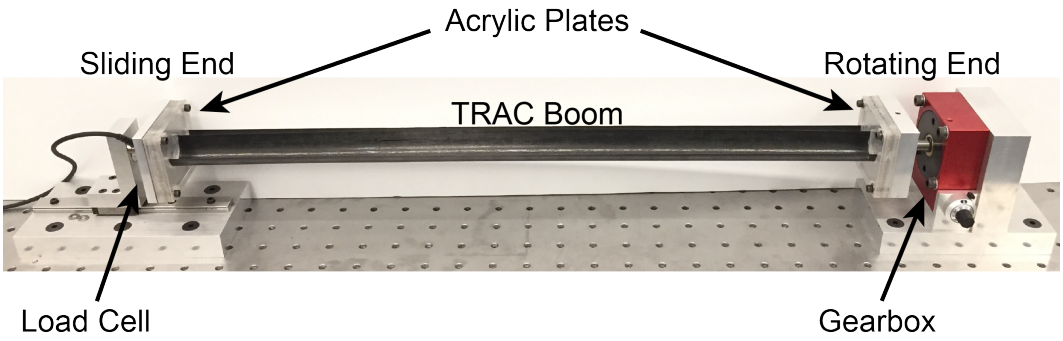

Figure 3.15: Torsion experimental setup.

3.3.2 Finite Element Simulations

A finite element model, shown in Figure 3.16, was built in Abaqus/Standard 2018 to predict the torsional behavior of TRAC structures. The structure is modeled using 4-node shell elements with reduced integration (S4R). A uniform mesh is used with element size of 2 mm, corresponding to 20 elements across each flange and 4 elements across the web. The material properties are defined in the form of a general stiffness matrix based on the properties given in Section 2.3.

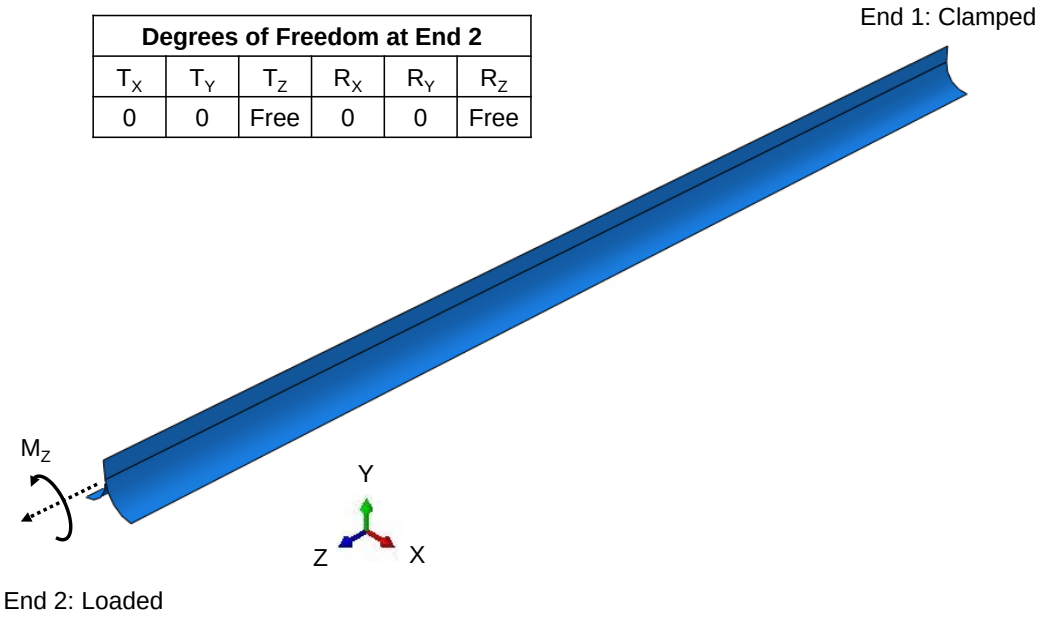

Figure 3.16: Finite element model for TRAC structure torsion, with boundary conditions (T = translation, R = rotation) and applied moments.

One end of the structure (end 1) is fully clamped along the full cross-section to reproduce the clamped boundary condition from the experiment. At the other end (end 2), all the nodes forming the cross-section are coupled to a reference point

using a kinematic coupling, effectively creating a rigid cross-section. This reference point is located at the centroid position defined by Y_C. A torque M_Z is applied at end 2. The boundary conditions at end 2 mirror the experimental setup, where only the axial displacement and rotation (T_Z and R_Z) are free. The simulation is performed using a nonlinear static step with an arc-length method (Riks). A rotation around the Z axis is imposed on the reference point at end 2, while the reaction torque is extracted. The geometry of the structure is adjusted to match the measured geometry.

3.3.3 Results

The torque-twist plots from both the experiment and the numerical simulation, over a range of twist angle from $-120°$ to $120°$ (equivalent to a twist varying from $-3.64\,\mathrm{rad\,m^{-1}}$ to $3.64\,\mathrm{rad\,m^{-1}}$), are shown in Figure 3.17a. The structure is able to undergo larger deformation, but the experiment was restricted to this range in order to prevent any damage. Figure 3.17b shows the torsional tangent stiffness, computed by numerical differentiation using a central difference algorithm, for both the experiment and the simulation.

These figures show that there is very good agreement between experiment and simulation. The maximum error is $2.15\,\mathrm{N\,mm}$ at a twist of $-3.64\,\mathrm{rad\,m^{-1}}$, which corresponds to an error of 9%. For a positive twist, the error at $3.64\,\mathrm{rad\,m^{-1}}$ is only $0.2\,\mathrm{N\,mm}$, less than 1% error. The root mean square of the error over the full range is $0.7\,\mathrm{N\,mm}$.

These figures also show that the relation between the torque and the twist is non-linear, due to warping as the ends are clamped. From Figure 3.17b, it can be seen that the torsional stiffness is a quadratic function of the twist.

Due to the manufacturing process, TRAC structure samples usually exhibit some residual twist post cure. This can be observed in Figure 3.17b, where the minimum torsional stiffness from experiment is located at a twist of $0.27\,\mathrm{rad\,m^{-1}}$, corresponding to a twist angle of $9°$. Correcting for that initial twist could decrease the error observed. This initial twist in the sample also explains why the behavior is not symmetric around a twist of 0.

Finally, the numerical simulations overestimates the initial torsional stiffness when compared with experiments. The minimum torsional stiffness from the simulations is $0.217\,\mathrm{N\,m^2}$, more than twice the minimum torsional stiffness from the experiments ($0.085\,\mathrm{N\,m^2}$).

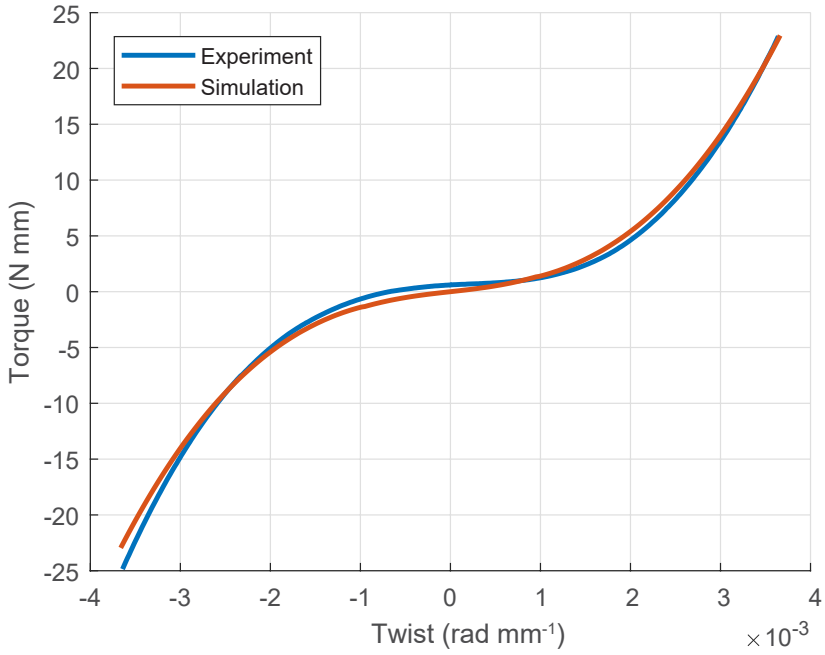

(a) Torque as a function of the twist.

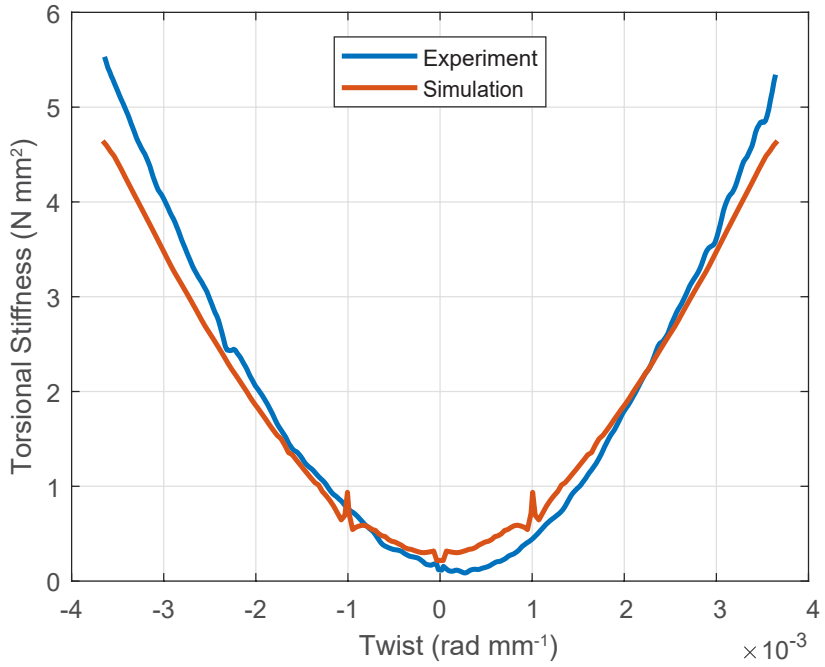

(b) Torsional stiffness as a function of the twist.

Figure 3.17: Comparison of experiment with simulation for TRAC structures under torsion.

Overall, the numerical model developed to study the torsion of ultra-thin TRAC structures was able to accurately predict the behavior observed in experiments, with the maximum error less than 10%.

3.4 Discussion

An investigation of the nonlinear deployed behavior of composite TRAC structures was presented in this chapter. Bending of the structures was investigated experimentally, by applying a pure moment around both axes of the cross-section. In both cases, a linear pre-buckling regime was observed, followed by further buckling events transitioning to a stable post-buckling regime. Ultimate buckling occurred at loads up to four times higher than the initial observed buckling. For loading cases where the flanges are in compression ($-X$ and Y bending), the first event corresponds to the formation of a localized buckle, which decreases the structural bending stiffness. Ultimate buckling occurs when one flange partially flattens at the location where the first buckle had formed, forming a kink at the intersection of the flange with the web. For $-X$ bending, the web is under compression and the initial buckling mode is a global wave pattern of the web. This wave pattern appeared very early in the test (0.1 N m), and led to a gradual decrease of the bending stiffness. Ultimate buckling occurred when the deformation localized.

A numerical simulation framework using the Abaqus finite-element software was presented to predict the behavior of TRAC structures subjected to pure bending. The same three loading conditions were studied: negative moment around X (web in tension), positive moment around X (web in compression) and moment around Y. In all cases, the simulation results matched well with experimental results. The stable post-buckling regime was accurately predicted for $+X$ and Y bending using the modified Riks method, but not for $-X$ bending. While simulations predicted well the pre- and post-buckling stiffness, the perfect geometry of the model was not able to capture the gradual softening observed in the experiments.

The effect of varying the length, from 300 mm to 5000 mm, on the buckling load was also studied numerically. When the flanges are loaded in compression ($-X$ and Y moments), nonlinearities during the pre-buckling phase needed to be taken into account. They lead to a mostly similar buckling mode for most of the length range. Hence, the $-X$ buckling load only decreased by 3% when increasing the length from 1000 mm to 4000 mm, and the Y buckling load only decreased by 10% when increasing the length from 1000 mm to 5000 mm. This behavior could be a

useful feature for the design of large structures. However, the buckling load for $-X$ bending at a length of 5000 mm was shown to decrease significantly, hinting at a change in behavior for longer structures. This will need to be investigated further. When the web is loaded under compression ($+X$ bending), both linear and nonlinear predictions agree. After a regime with constant buckling moment, the critical load decreases with length, dropping by 60% from 2000 mm to 5000 mm.

The torsional behavior of TRAC structures was also investigated. Experiments showed that very large torsional deformation can be obtained without any buckling. A numerical model was developed and good agreement was obtained when compared with experimental results. The behavior was shown to be somewhat sensitive to the initial twist of the structure. However, due to the low torsional stiffness at low twist angle, even an initial twist of 16°/m did not affect much the results. It was also observed that the torsional stiffness increases quadratically with twist.

Chapter 4

ANALYTICAL BUCKLING PREDICTION OF ORTHOTROPIC CYLINDRICAL SHELL PANELS WITH A FREE EDGE

This chapter presents a method to predict linear buckling of a TRAC structure loaded with pure moment around the Y axis. Under this loading condition, it is assumed that the web has little effect, being located on the structure's neutral axis. Therefore, as buckling occurs in the inner flange, the buckling load can be predicted by studying a simpler structure, representing the isolated inner flange, consisting of an open cylindrical shell panel with a free edge loaded under a non-uniform compression.

First, a literature review of buckling of axially compressed cylindrical shells is presented. Second, the analytical model, using the Donnell linear shallow shell equations and the Rayleigh-Ritz method is introduced. Third, a simple problem, a simply-supported cylindrical shell panel under uniform axial compression, is solved to validate the method. Fourth, buckling of an isotropic TRAC structure is estimated. Then, the equations are extended to orthotropic structures and the buckling load of a composite TRAC structure is estimated. Finally, a discussion closes this chapter.

4.1 Background: Elastic Buckling of Thin-Walled Cylindrical Shells

Cylindrical shells have been used extensively as structural elements. To improve the mass efficiency of such structures, shells are designed to be very thin when compared to other dimensions, such as radius and length. This can lead to stability issues, and the design of cylindrical shells needs to involve buckling considerations.

Classical buckling of cylindrical shells has been studied by many authors in the past. A simple form of the equilibrium and stability equations for a cylindrical shell was derived by Donnell, (1933, 1934), based on the Kirchhoff-Love shell theory (Love, 1892). The principal assumptions of this theory are:

1. The thickness of the shell is small compared to the radius, such that $t/r \ll 1$.

For example, Novozhilov proposed $t/r \leq 20$ to keep the error below 5% (Novozhilov, 1959);

2. Strains are small, so higher-order terms can be neglected when compared to first-order terms;

3. The transverse normal stress σ_z is negligible;

4. The normals to the undeformed mid-surface of the shell remain straight and normal to the deformed mid-surface, and there is no transverse extension.

This reduces the three-dimensional problem to a two-dimensional problem, where the shell behavior is described only by the mid-surface strains and curvature. Furthermore, as a consequence of the fourth assumption, the transverse shear strains are zero ($\gamma_{xz} = \gamma_{\phi z} = 0$). As a result, the displacements at any point in the shell can be obtained from

$$\bar{u}(x, \phi, z) = u(x, \phi) - z\frac{\partial w(x, \phi)}{\partial x} \tag{4.1a}$$

$$\bar{v}(x, \phi, z) = v(x, \phi) - \frac{z}{r}\frac{\partial w(x, \phi)}{\partial \phi} \tag{4.1b}$$

$$\bar{w}(x, \phi, z) = w(x, \phi) \tag{4.1c}$$

where (x, ϕ, z) are the axial, transverse and normal directions, $(\bar{u}, \bar{v}, \bar{w})$ are the displacements in the axial, transverse and normal directions, and (u, v, w) are the mid-plane value of the displacements.

Donnell's equations (presented in Section 4.2) were initially derived for shallow and quasi-shallow shells, i.e. shells that are relatively flat or for which the buckling half-wavelength is small when compared to the shell curvature (Bazant and Cedolin, 2010). Due to this assumption and the four previous ones, these equations can be exactly solved for some specific cases. For this reason, they are often used to study the stability of cylindrical shells. For example, Batdorf, (1947) used these equations to find the buckling load of a closed cylinder under axial compression, and Seide and Weingarten, (1961) studied the buckling of a closed cylinder under pure bending.

The stability of orthotropic cylindrical shells was studied by many authors; for example Becker and Gerard, (1962), Dong, Pister, and Taylor, (1962), Hess, (1961), and J. Peterson, Seide, and Weingarten, (1968). A comparison of different shell theories in terms of the accuracy of the buckling prediction for laminated composite panels was performed by Jaunky and Knight, (1999), showing that the Donnell shell

theory overestimates the axial compressive buckling load. In Brush and Almroth, (1975), the linear stability equations for orthotropic cylindrical shells are derived and compared with Donnell's equations. Onoda, (1985) used the Donnell equations, extended to account for material orthotropy, coupled with the Rayleigh-Ritz method to estimate the axial compressive buckling load of laminated cylindrical shells, and to optimize the laminate configuration.

All of the studies presented above were for either circular cylinders, or cylindrical panels with simply supported boundary conditions. For the problem of interest in this chapter, the open shell has a free edge. The buckling of isotropic cylindrical shells with two longitudinal free edges subjected to uniform compressive load was studied by Chu and Krishnamoorthy, (1967), Turula and Chu, (1970) and T. Yang and Guralnick, (1976). A solution for the buckling of a cylindrical panel with two longitudinal free edges loaded with both a compressive load and an end moment was proposed by Krishnamoorthy and Narang, (1977). The buckling of a cylindrical panel under uniform axial compression with one longitudinal free edge and three simply supported edges was also studied by Magnucki and Maćkiewicz, (2006), Szyc, Laszczyk, and Magnucki, (2006) and Wilde, Zawodny, and Magnucki, (2007).

While extensive work has been done on the buckling of cylindrical shells, the specific case of interest in this chapter, consisting of a cylindrical orthotropic panel with one longitudinal free edge and loaded with a non-uniform axial compression has not been previously studied.

4.2 Method Description

4.2.1 Problem Statement

Figure 4.1 illustrates the buckling problem of interest. A TRAC structure of length L with flange radius r, opening angle θ_f and thickness t, is loaded with moments M_y around the Y axis at each end. It is assumed that the boundary conditions at each end are simply supported (SS). As shown in Chapter 3, for a short structure ($L \leq 800\,\text{mm}$) the buckling mode when loaded with a moment around the Y axis is localized in the inner flange. Therefore, for this type of buckling the simpler problem shown in Figure 4.2 can be considered. It consists of a cylindrical panel with the same dimensions (L, r, θ_f and t) loaded with a non-constant axial force resultant N_x which is a function of ϕ. Here, a cylindrical coordinate system is chosen, where x and ϕ are the axial and tangential directions, respectively. This shell is simply supported at both ends and along one longitudinal edge, while the

other longitudinal edge is free. The solution of this simplified problem will be compared to the buckling of a complete TRAC structure later in this chapter.

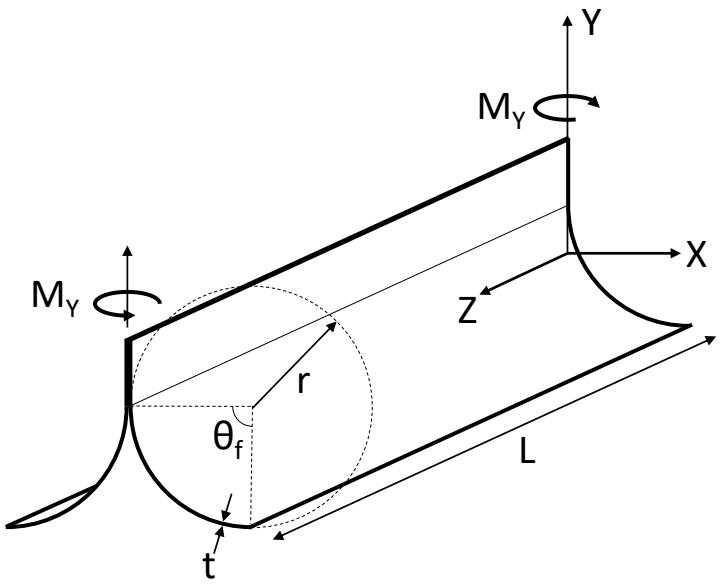

Figure 4.1: A TRAC structure of length L with flange radius r, opening angle θ_f and thickness t, is loaded under a pure moment M_Y around the Y axis of the global coordinate system.

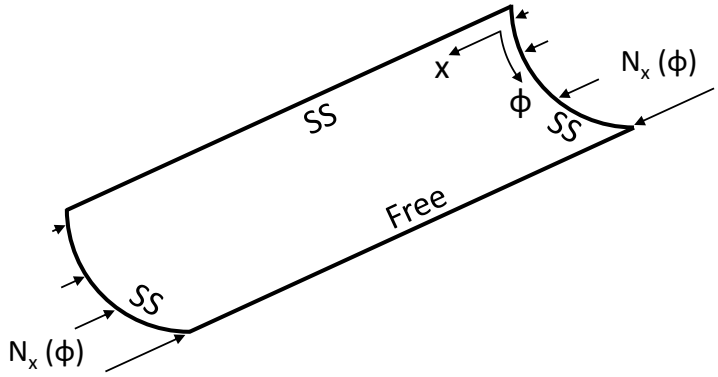

Figure 4.2: Simplified model of the TRAC structure inner flange loaded by a pure moment. x and ϕ are the axial and tangential directions of the shell in a cylindrical coordinate system. The shell is simply supported (SS) on three side, and free along one edge. A compressive force per unit length N_x, function of ϕ, is applied at each end.

In order to define $N_x(\phi)$, the pre-buckling equilibrium of the whole structure is studied. It is assumed that plane cross-sections remain plane and undeformed, and that the material is linear-elastic. Using the global coordinate system X, Y and Z,

the moment equilibrium around Y in a cross-section is given by

$$M_Y = \iint X \sigma_Z dX dY \tag{4.2}$$

The longitudinal stress σ_Z is a linear function of X, and can be written as

$$\sigma_Z(X) = \sigma_Z^0 X \tag{4.3}$$

where σ_Z^0 is a constant. The moment equilibrium can then be written as

$$M_Y = \iint X^2 \sigma_Z^0 dX dY = \sigma_Z^0 I_Y = \frac{\sigma_Z(X) I_Y}{X} \tag{4.4}$$

where I_Y is the second moment of area of the cross-section around the Y axis. It is important to note that going from the global coordinate system to the shell coordinate system implies $\sigma_Z = \sigma_x$. The force resultant N_x can be obtained from

$$N_x = \int_{-t/2}^{t/2} \sigma_x dz \tag{4.5}$$

Combining Equation 4.5 with Equation 4.4 and assuming that due to the thinness of the shell, σ_x is constant across the wall thickness, the following relation is found

$$N_x = \frac{t M_Y X}{I_Y} \tag{4.6}$$

Finally, the X coordinate can be expressed as a function of ϕ in the cylindrical coordinate system. Defining $\phi = 0$ at the longitudinal, simply supported edge, where the web would begin, then the relation becomes

$$N_x = \frac{t M_Y r \, (1 - \cos \phi)}{I_Y} = N_x^0 \, (1 - \cos \phi) \tag{4.7}$$

where N_x^0 is a constant. Therefore, Equation 4.7 defines the load to apply in the buckling problem shown in Figure 4.2.

4.2.2 Donnell's Stability Equations

Figure 4.3 shows a cylindrical shell element and defines the force stress resultants (N_x, N_ϕ, $N_{x\phi}$, $N_{\phi x}$, Q_x and Q_ϕ) and the moment stress resultants (M_x, M_ϕ, $M_{x\phi}$ and $M_{\phi x}$). These resultants are defined as a force or moment per unit length, and can be obtained by integrating the stresses across the thickness.

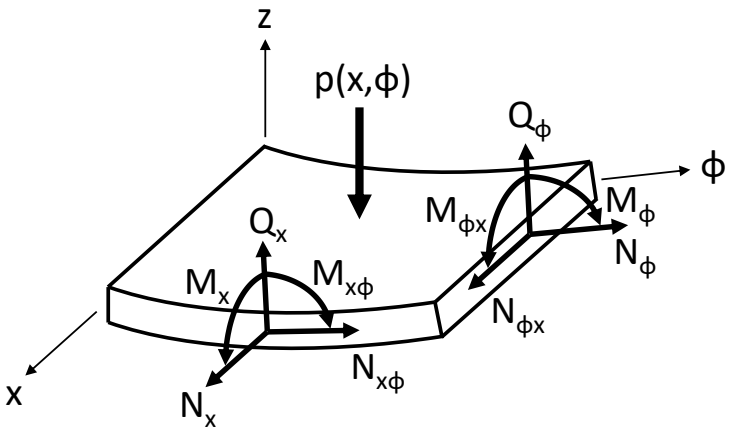

Figure 4.3: Force and moment resultants acting on a cylindrical shell element, expressed in the cylindrical coordinate system x, ϕ, z.

Donnell's equilibrium equations for isotropic material can be written in the following form (Brush and Almroth, 1975)

$$rN_{x,x} + N_{x\phi,\phi} = 0 \tag{4.8a}$$

$$rN_{x\phi,x} + N_{\phi,\phi} = 0 \tag{4.8b}$$

$$D\nabla^4 w + \frac{1}{r}N_\phi - \left(N_x w_{,xx} + \frac{2}{r}N_{x\phi}w_{,x\phi} + \frac{1}{r^2}N_\phi w_{,\phi\phi}\right) = p(x,\phi) \tag{4.8c}$$

where p is the normal pressure and

$$\nabla^4 w \equiv w_{,xxxx} + \frac{2}{r^2}w_{,xx\phi\phi} + \frac{1}{r^4}w_{,\phi\phi\phi\phi} \tag{4.9}$$

Subscripts following a comma denote a partial derivative with respect to those variables. The constitutive equations for isotropic shells are

$$\begin{aligned} N_x &= C\left(\varepsilon_x + \nu\varepsilon_\phi\right) & M_x &= D\left(\kappa_x + \nu\kappa_\phi\right) \\ N_\phi &= C\left(\varepsilon_\phi + \nu\varepsilon_x\right) & M_\phi &= D\left(\kappa_\phi + \nu\kappa_x\right) \\ N_{x\phi} &= C\frac{1-\nu}{2}\gamma_{x\phi} & M_{x\phi} &= D\left(1-\nu\right)\kappa_{x\phi} \end{aligned} \tag{4.10}$$

where C and D are the extensional and bending stiffness, respectively, and are defined as

$$C \equiv \frac{Et}{1-\nu^2} \qquad D \equiv \frac{Et^3}{12\left(1-\nu^2\right)} \tag{4.11}$$

The kinematic relations are (from Donnell, 1933)

$$\begin{aligned}
\varepsilon_x &= u_{,x} + \frac{1}{2}\beta_x^2 & \kappa_x &= \beta_{x,x} = -w_{,xx} & & \\
\varepsilon_\phi &= \frac{v_{,\phi} + w}{r} + \frac{1}{2}\beta_\phi^2 & \kappa_\phi &= \frac{\beta_{\phi,\phi}}{r} = -\frac{w_{,\phi\phi}}{r^2} & \beta_x &= -w_{,x} \\
\gamma_{x\phi} &= \left(\frac{u_{,\phi}}{r} + v_{,x}\right) + \beta_x\beta_\phi & \kappa_{x\phi} &= \frac{1}{2}\left(\frac{\beta_{x,\phi}}{r} + \beta_{\phi,x}\right) & \beta_\phi &= -\frac{w_{,\phi}}{r}
\end{aligned} \tag{4.12}$$

where u, v and w are the displacement in the x, ϕ and z directions respectively. β_x and β_ϕ are the mid-plane rotations in the x and ϕ directions, respectively.

To derive Donnell's stability equations, Brush and Almroth, (1975) introduced a small displacement increment starting from an initial equilibrium configuration. Hence, the displacements can be expressed as

$$u = u_0 + u_1 \qquad v = v_0 + v_1 \qquad w = w_0 + w_1 \tag{4.13}$$

Introducing these displacements in the equilibrium equation, Brush and Almroth, (1975) showed that the following uncoupled Donnell stability equations can be obtained:

$$\nabla^4 u_1 = -\frac{\nu}{r} w_{1,xxx} + \frac{1}{r^3} w_{1,x\phi\phi} \tag{4.14a}$$

$$\nabla^4 v_1 = -\frac{2+\nu}{r^2} w_{1,xx\phi} - \frac{1}{r^4} w_{1,\phi\phi\phi} \tag{4.14b}$$

$$D\nabla^8 w_1 + \frac{1-\nu^2}{r^2} C w_{1,xxxx} - \nabla^4\left(N_{x0} w_{1,xx} + \frac{2}{r} N_{x\phi 0} w_{1,x\phi} + \frac{1}{r^2} N_{\phi 0} w_{1,\phi\phi}\right) = 0 \tag{4.14c}$$

which are linear with respect to (u_1, v_1, w_1) and where $\nabla^8 w_1 \equiv \nabla^4(\nabla^4 w_1)$. The stress resultants are defined as

$$\begin{aligned}
N_{x0} &= C\left(\varepsilon_{x0} + \nu\varepsilon_{\phi 0}\right) & \varepsilon_{x0} &= u_{0,x} + \frac{1}{2} w_{0,x}^2 \\
N_{\phi 0} &= C\left(\varepsilon_{\phi 0} + \nu\varepsilon_{x0}\right) & \varepsilon_{\phi 0} &= \frac{v_{0,\phi} + w_0}{r} + \frac{1}{2}\frac{w_{0,\phi}^2}{r^2} \\
N_{x\phi 0} &= C\frac{1-\nu}{2}\gamma_{x\phi 0} & \gamma_{x\phi 0} &= \left(\frac{u_{0,\phi}}{r} + v_{0,x}\right) + \frac{w_{0,x} w_{0,\phi}}{r}
\end{aligned} \tag{4.15}$$

Here, the displacements increments u_1, v_1 and w_1 define the buckling mode, while the initial displacements u_0, v_0 and w_0 define the pre-buckling solution. Equations 4.14 can be solved directly for simple loads and boundary conditions, as shown in Section 4.3.

4.2.3 Rayleigh-Ritz Method

For complex loads and boundary conditions, Equation 4.14c cannot be solved directly. An approximate solution can be obtained using the Rayleigh-Ritz method, for example described in Varadan and Bhaskar, (1999). This method was used by many workers to solve shell buckling problems. Almroth, (1962) used this approach for a cylindrical shell with non-uniform external pressure, and Ansari, Sahmani, and Rouhi, (2011) studied buckling of carbon nanotubes under axial loading with various boundary conditions.

For a system under load, a state of stable equilibrium corresponds to a minimum of the total potential energy, Π. Therefore, the minimum buckling load represents the load at which the total potential energy is stationary, i.e. both the first and second variation of the total potential energy are zero.

The Rayleigh-Ritz method for estimating buckling loads consists in assuming a displacement field that satisfies both compatibility and kinematic boundary conditions. It does not need to satisfy natural boundary conditions. Then, the total potential energy can be calculated and the buckling load found by solving for the loads when the second variation is equal to zero. This method gives an upper bound to the buckling load. To improve the estimate, the displacement field can be assumed to be a linear combination of multiple functions.

Brush and Almroth, (1975) derived the equation for the second variation of the total potential energy of a shallow cylindrical shell. Their expression will be used in this chapter for buckling of isotropic shells

$$\begin{aligned}\frac{1}{2}\delta^2\Pi = \frac{rC}{2}\iint\left(\varepsilon_{x1}^2+\varepsilon_{\phi1}^2+2\nu\varepsilon_{x1}\varepsilon_{\phi1}+\frac{1-\nu}{2}\gamma_{x\phi1}^2\right)dxd\phi \\ +\frac{r}{2}\iint\left(N_{x0}w_{1,x}^2+N_{\phi0}\frac{w_{1,\phi}^2}{r^2}+2N_{x\phi0}w_{1,x}\frac{w_{1,\phi}}{r}\right)dxd\phi \\ +\frac{rD}{2}\iint\left(w_{1,xx}^2+\frac{w_{1,\phi\phi}^2}{r^4}+2\nu w_{1,xx}\frac{w_{1,\phi\phi}}{r^2}+2\left(1-\nu\right)\frac{w_{1,x\phi}^2}{r^2}\right)dxd\phi\end{aligned} \tag{4.16}$$

where the strains (neglecting pre-buckling rotations $w_{0,x}$ and $w_{0,\phi}$) can be expressed as

$$\varepsilon_{x1} = u_{1,x} \qquad \varepsilon_{\phi 1} = \frac{v_{1,\phi} + w_1}{r} \qquad \gamma_{x\phi 1} = \frac{u_{1,\phi}}{r} + v_{1,x} \tag{4.17}$$

4.3 Simply Supported Isotropic Tape-Spring Under Uniform Compression

The first problem that will be studied is shown in Figure 4.4. A cylindrical shell of length L with radius r and opening angle θ_f is loaded under constant axial compression N_x, where N_x is a force per unit length. The shell is simply supported on all sides and is made of an isotropic material with thickness t, Young's modulus E, and Poisson's ratio ν. As shown for example by Timoshenko and Gere, (1961), this problem can be solved using the same method as for a cylindrical tube.

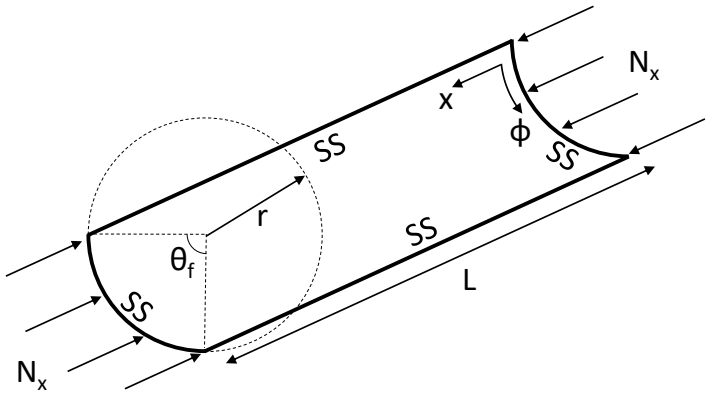

Figure 4.4: Cylindrical shell of length L with radius r and opening angle θ_f loaded under uniform axial compression with all four sides simply supported (SS).

The pre-buckling equilibrium configuration can be found using the linear membrane equations (Brush and Almroth, 1975) as there is no out-of-plane deformation in the pre-buckling state ($w(x, \phi) = 0$)

$$rN_{x0,x} + N_{x\phi 0,\phi} = 0 \qquad rN_{x\phi 0,x} + N_{\phi 0,\phi} = 0 \qquad N_{\phi 0} = pr \tag{4.18}$$

Both partial derivatives of $N_{x\phi 0}$ are zero as there is no pressure and N_{x0} is constant. Therefore, $N_{x\phi 0}$ is also a constant, and must be zero as its value is zero at the boundaries. As a result, Equation 4.14c can be solved exactly. One can observe that only even derivatives are present in this equation. The simply supported boundary conditions mean that at the boundary the out-of-plane displacement and the applied

moment are zero, which can be expressed as

$$\begin{aligned} w = w_{,xx} = 0 \quad \text{at} \quad x = 0, L \\ w = w_{,\phi\phi} = 0 \quad \text{at} \quad \phi = 0, \theta \end{aligned} \tag{4.19}$$

Hence, the solution is of the form

$$w_1(x, \phi) = A_0 \sin \frac{m\pi x}{L} \sin \frac{n\pi \phi}{\theta} \tag{4.20}$$

The critical buckling load can be found by substituting this expression into Equation 4.14c, and solving for N_x. The critical buckling load is then found by minimizing N_x with respect to n and m. For the shell described in Table 4.1, the minimum buckling load is $N_x = -33.23\,\mathrm{N\,mm^{-1}}$, with $n = 1$ and $m = 253$.

Table 4.1: Dimensions and material properties for isotropic cylindrical shell.

r [mm]	θ_f	L [mm]	t [mm]	E [GPa]	ν
12.7	90°	500	0.1	69	0.33

A solution can also be obtained using the Rayleigh-Ritz method. Assuming $w_1(x, \phi)$ to be given by Equation 4.20, Equations 4.14a-b can be solved to find $u_1(x, \phi)$ and $v_1(x, \phi)$. Because the assumed function is the exact solution, it is expected that solving using the energy equation (Equation 4.16) will yield the same result. The following expressions are obtained:

$$u_1(x, \phi) = B_0 \cos \bar{m}x \sin \bar{n}\phi \tag{4.21a}$$

$$v_1(x, \phi) = C_0 \sin \bar{m}x \cos \bar{n}\phi \tag{4.21b}$$

where

$$\bar{m} = m\pi/L \qquad\qquad \bar{n} = n\pi/\theta \tag{4.22}$$

and

$$\begin{aligned} B_0 &= \frac{A_0 \bar{m} r \left(\bar{m}^2 \nu r^2 - \bar{n}^2\right)}{\left(r^2 \bar{m}^2 + \bar{n}^2\right)^2} \\ C_0 &= \frac{A_0 \bar{n} \left(\bar{m}^2 r^2 (2 + \nu) + \bar{n}^2\right)}{\left(r^2 \bar{m}^2 + \bar{n}^2\right)^2} \end{aligned} \tag{4.23}$$

The critical buckling load can then be obtained by substituting Equations 4.20 and 4.21 into Equation 4.16 to obtain the second variation of the total potential energy. The resulting expression is set equal to zero, and solved for N_{x0}. For the shell described in Table 4.1, the buckling is found to be $N_x = -33.23\,\mathrm{N\,mm^{-1}}$, once again with $n = 1$ and $m = 253$. Therefore, the Rayleigh-Ritz method gave the same result as the exact solution, as expected. The corresponding mode shape is shown in Figure 4.5.

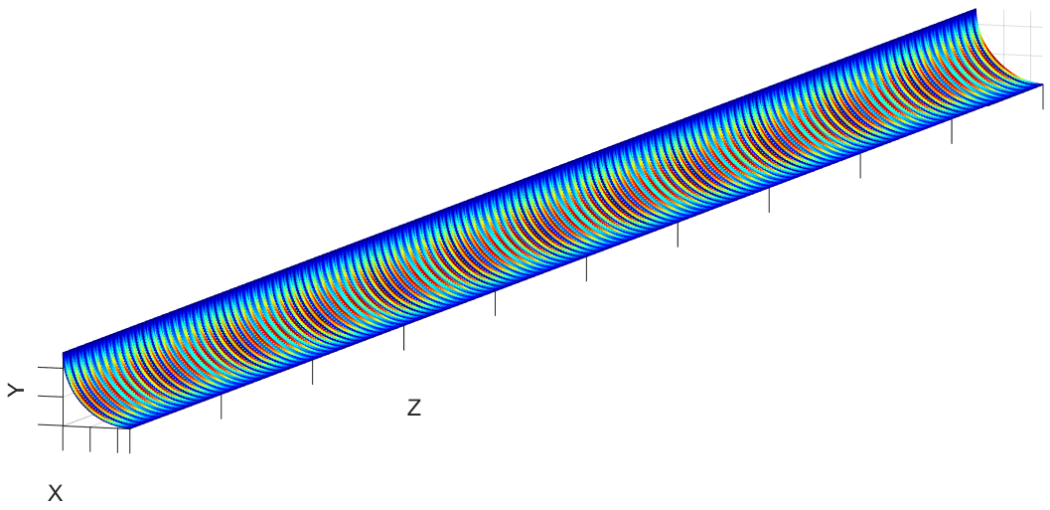

Figure 4.5: Analytical buckling mode for an isotropic cylindrical shell loaded under uniform axial compression and simply supported on all sides, with $L = 500\,\mathrm{mm}$, $r = 12.7\,\mathrm{mm}$, $\theta_f = 90°$ and $t = 0.1\,\mathrm{mm}$. The associated buckling load is $N_x = -33.23\,\mathrm{N\,mm^{-1}}$.

For a further validation of these results, the buckling load for this specific case was also obtained using the finite element software Abaqus Standard 2018. A model was created using the properties from Table 4.1. The structure was modeled using quadrilateral shell elements with reduced integration (S4R). To capture the small wavelength buckling predicted (253 half-waves along the length, equal to a half-wavelength of ≈ 2 mm), the mesh size was chosen as 0.5 mm, corresponding to 1000 elements along the length and 40 elements along the transverse direction. All edges are simply supported, and the shell is loaded symmetrically with a uniformly distributed edge compressive load at each end. The buckling load was calculated using a linear perturbation step with the Eigensolver *Subspace*. The buckling mode obtained from the simulation can be seen in Figure 4.6, and the associated buckling load was found to be $N_x = -33.22\,\mathrm{N\,mm^{-1}}$.

As predicted from the analytical model, the buckling mode has a very short wave-

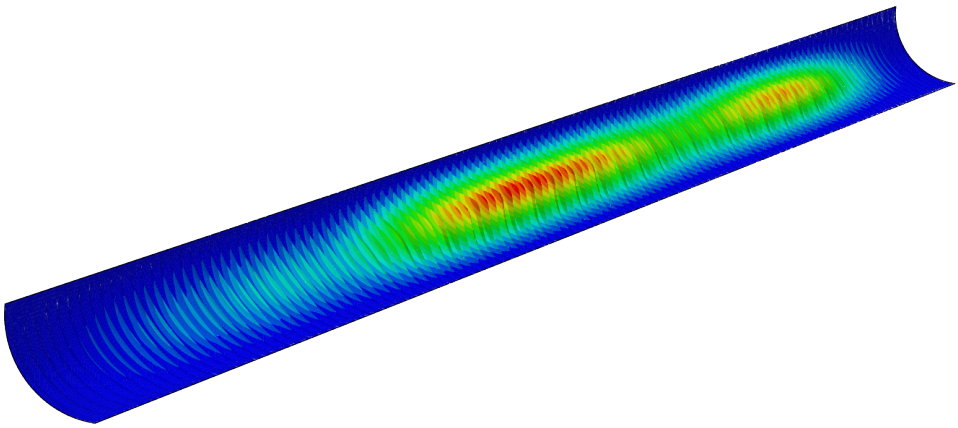

Figure 4.6: Buckling mode obtained from finite element for an isotropic cylindrical shell loaded under uniform axial compression and simply supported on all sides, with $L = 500\,\text{mm}$, $r = 12.7\,\text{mm}$, $\theta_f = 90°$ and $t = 0.1\,\text{mm}$. The associated buckling load is $N_x = -33.22\,\text{N}\,\text{mm}^{-1}$.

length in the axial direction, and only one half-wave in the transverse direction. However, the buckling mode obtained from the finite element simulation also has a longer wavelength component in the axial direction, as shown in Figure 4.6. Despite this small discrepancy, the difference between the two predicted buckling loads is negligible.

Using this simple test case, the Rayleigh-Ritz method was validated both by comparing with the direct analytical solution and a finite element simulation. It is important to note, however, that for this specific problem, the assumption behind the shallow shell theory, which is that the wavelength of the buckling mode is small when compared to the shell radius of curvature, was valid.

4.4 Cylindrical Panel with Free Edge Under Non-Uniform Compression

For the simplified version of the TRAC structure buckling described in Section 4.2.1 and shown in Figure 4.2, the stability equation 4.14c cannot be solved directly as it was done for the simply supported shell in the previous section. Therefore, the Rayleigh-Ritz method will be used directly.

In this case, the displacement field is not known. The accuracy of the Rayleigh-Ritz method directly depends on how close the assumed shape function is to the real displacement field. Therefore, the initial guess is important. To comply with the Rayleigh-Ritz method requirements, the shape functions need to satisfy the

kinematic boundary conditions, which for this problem are

$$\begin{aligned} w &= 0 \quad \text{at} \quad x = 0, L \\ w &= 0 \quad \text{at} \quad \phi = 0 \end{aligned} \tag{4.24}$$

Furthermore, while it is not necessary, the natural boundary conditions on the three simply supported edges can easily be satisfied. These boundary conditions are expressed as

$$\begin{aligned} w_{,xx} &= 0 \quad \text{at} \quad x = 0, L \\ w_{,\phi\phi} &= 0 \quad \text{at} \quad \phi = 0 \end{aligned} \tag{4.25}$$

The w displacement field is assumed to be of the following form

$$w_1(x, \phi) = f_x(x) f_\phi(\phi) \tag{4.26}$$

To satisfy the boundary conditions at $x = 0, L$, $f_x(x)$ is assumed to be

$$f_x(x) = \sin\left(\frac{m\pi x}{L}\right) \tag{4.27}$$

For the transverse direction, the shape function is assumed to be similar to the shape function of a plate simply supported on three sides and free on one side, which is a combination of a hyperbolic sine and a sine function (Jones, 2006). Therefore, the assumed displacement field is

$$w_1(x, \phi) = \sin\left(\frac{m\pi x}{L}\right)\left(A_1 \sinh(\alpha\phi) + A_2 \sin\left(\frac{\beta\phi}{\theta_f}\right)\right) \tag{4.28}$$

where α and β are free parameters that can be varied to find the minimum buckling load. To further simplify the problem, it is assumed that $\beta = \pi/2$ such as $\sin\left(\beta\phi/\theta_f\right) = 1$ at $\phi = \theta_f$. This assumption will be used in the remaining of this chapter.

The displacement field $u_1(x, \phi)$ and $v_1(x, \phi)$ can once again be obtained by solving Equations 4.14a-b. The expressions are

$$u_1(x, \phi) = \cos(\bar{m}x)\left(B_1 \sinh(\alpha\phi) + B_2 \sin\left(\bar{\beta}\phi\right)\right) \tag{4.29a}$$

$$v_1(x, \phi) = \sin(\bar{m}x)\left(C_1 \cosh(\alpha\phi) + C_2 \cos\left(\bar{\beta}\phi\right)\right) \tag{4.29b}$$

where

$$\bar{m} = m\pi/L \qquad\qquad \bar{\beta} = \pi/2\theta_f \tag{4.30}$$

and

$$\begin{aligned} B_1 &= \frac{A_1 \bar{m} r \left(\bar{m}^2 \nu r^2 + \alpha^2\right)}{\left(r^2\bar{m}^2 - \alpha^2\right)^2} \\ B_2 &= \frac{A_2 \bar{m} r \left(\bar{m}^2 \nu r^2 - \bar{\beta}^2\right)}{\left(r^2\bar{m}^2 + \bar{\beta}^2\right)^2} \\ C_1 &= \frac{A_1 \alpha \left(\bar{m}^2 (2+\nu) r^2 - \alpha^2\right)}{\left(r^2\bar{m}^2 - \alpha^2\right)^2} \\ C_2 &= \frac{A_2 \left(\bar{m}^2 (2+\nu) r^2 + \bar{\beta}^2\right)}{\left(r^2\bar{m}^2 + \bar{\beta}^2\right)^2} \end{aligned} \tag{4.31}$$

As detailed in Section 4.2.1, the edge loading is given by

$$N_{x0} = N_x^0 (1 - \cos\phi) \tag{4.32}$$

Solving the linear membrane equations (Equations 4.18) gives $N_{\phi 0} = N_{x\phi 0} = 0$.

This problem was solved using the Maple software for symbolic mathematical computation. Substituting Equations 4.28 and 4.29 in the second variation of the total potential energy (Equation 4.16), the result is a quadratic form in A_1 and A_2. This can be written in the form

$$\begin{bmatrix} A_1 & A_2 \end{bmatrix} \bar{\boldsymbol{A}} \begin{bmatrix} A_1 \\ A_2 \end{bmatrix} = 0 \tag{4.33}$$

where $\bar{\boldsymbol{A}}$ is a coefficient matrix. The critical buckling load is found by setting the determinant of $\bar{\boldsymbol{A}}$ equal to zero and solving for N_x^0. The result is an expression that is a function of the geometry (L, r, θ_f and t), the material properties (E and ν), and two parameters: m and α.

The mode shape can also be computed by substituting the critical buckling load, assuming $A_1 = 1$, and solving for A_2 in the following expression

$$\bar{\boldsymbol{A}} \begin{bmatrix} A_1 \\ A_2 \end{bmatrix} = 0 \tag{4.34}$$

Specializing for the shell described in Table 4.1, the critical buckling load is $N_x^0 = -2.25\,\mathrm{N\,mm^{-1}}$, with $m = 1$ and $\alpha = 1.06$. The corresponding mode shape, shown in Figure 4.7, is defined by $A_1 = 1$ and $A_2 = 1.68$.

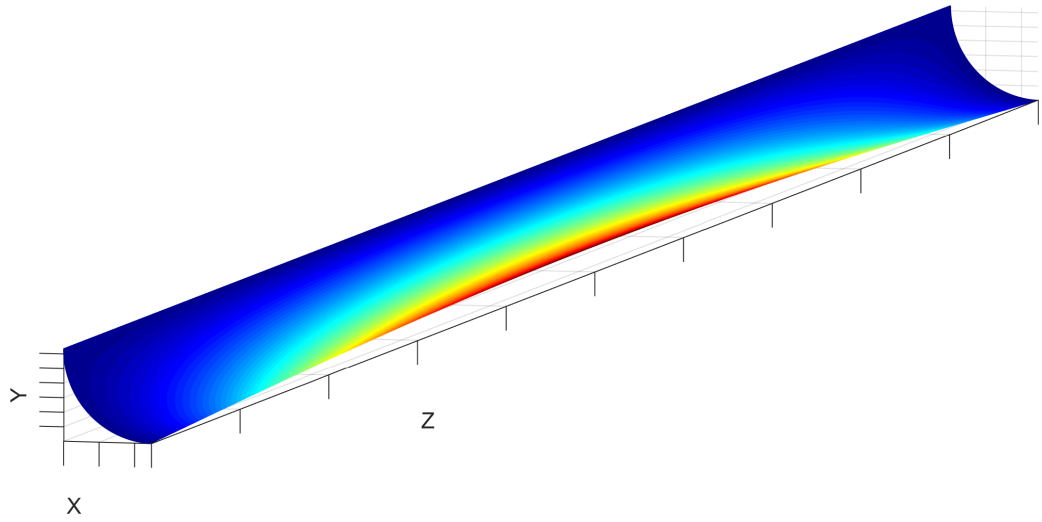

Figure 4.7: Analytical buckling mode for an isotropic cylindrical shell loaded under non-uniform axial compression, simply supported on three sides and free along one longitudinal edge, with $L = 500\,\text{mm}$, $r = 12.7\,\text{mm}$, $\theta_f = 90°$ and $t = 0.1\,\text{mm}$. The associated buckling load is $N_x^0 = -2.25\,\text{N mm}^{-1}$.

This analytical solution can be compared with a numerical simulation. The same model presented in the previous section is used to predict the buckling load for this case. The constraints along one longitudinal side are removed to obtain the free edge, and the compressive load is defined as an *Analytical Field* in Abaqus, following Equation 4.32.

Figure 4.8 shows the buckling mode obtained from simulation. The associated buckling load is $N_x^0 = -2.75\,\text{N mm}^{-1}$. As predicted from the Rayleigh-Ritz method, there is only one half-wavelength along the longitudinal direction. However, this means that this case, in contrast with the previous shell simply supported on all sides, does not comply very well with the shallow shell assumption of a small wavelength when compared with the radius. To obtain the equations presented in Section 4.2, it was assumed that some terms are negligibly small, for example the contribution of v on the shell rotation was neglected. While the difference between the numerical and the Rayleigh-Ritz results is less than 20%, a more complete shell theory, while harder to implement, could be used to reduce the difference.

The ability of the simplified shell model to predict the TRAC structure critical buckling moment was also verified using finite element method. The framework described in Section 3.2.2 was used to predict the buckling of an isotropic TRAC structure. Additionally to the properties defined in Table 4.1, the web width w was 8 mm and the web thickness was twice the flange thickness. A pure bending moment

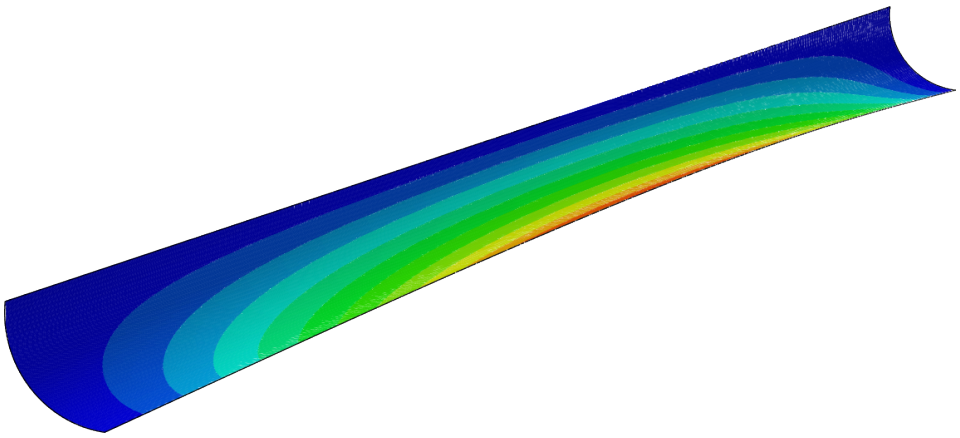

Figure 4.8: Finite element buckling mode for an isotropic cylindrical shell loaded under non-uniform axial compression, simply supported on three sides and free along one longitudinal edge, with $L = 500\,\text{mm}$, $r = 12.7\,\text{mm}$, $\theta_f = 90°$ and $t = 0.1\,\text{mm}$. The associated buckling load is $N_x^0 = -2.75\,\text{N mm}^{-1}$.

M_Y was applied at each end.

The critical moment obtained from the finite element simulation is $M_Y = 511\,\text{N mm}$ and the buckling mode is shown in Figure 4.9. Using Equation 4.7, with $I_Y = 148\,\text{mm}^4$ (computed from Equation 2.7), this critical moment can be compared with the estimate of the critical edge compression obtained from the simplified model. The result is $N_x^0 = -4.39\,\text{N mm}^{-1}$, which is 95% higher than the analytical prediction of $-2.25\,\text{N mm}^{-1}$, and 60% higher than the numerical result for the simplified model, $-2.75\,\text{N mm}^{-1}$.

While the buckling modes observed in the simplified model and the full TRAC structure model are similar, the TRAC structure buckling mode also includes a torsional component which was not captured by the simplified model. Furthermore, the attachment between the flange and the web is not exactly equivalent to a simply supported boundary condition, as there is a bending stiffness along the web. One could therefore assume that, due to the rotation of the web, the boundary condition along the web would be closer to a rotational spring. To test this assumption, the buckling load for the simple cylindrical shell model was calculated with Abaqus, for the case of a clamped boundary condition, instead of the simply supported longitudinal edge. For this new case, the critical buckling load was found to be $N_x^0 = -5.52\,\text{N mm}^{-1}$.

Table 4.2 summarizes the results obtained in the current section, with the critical moment M_Y calculated from Equation 4.7. While the Rayleigh-Ritz method was

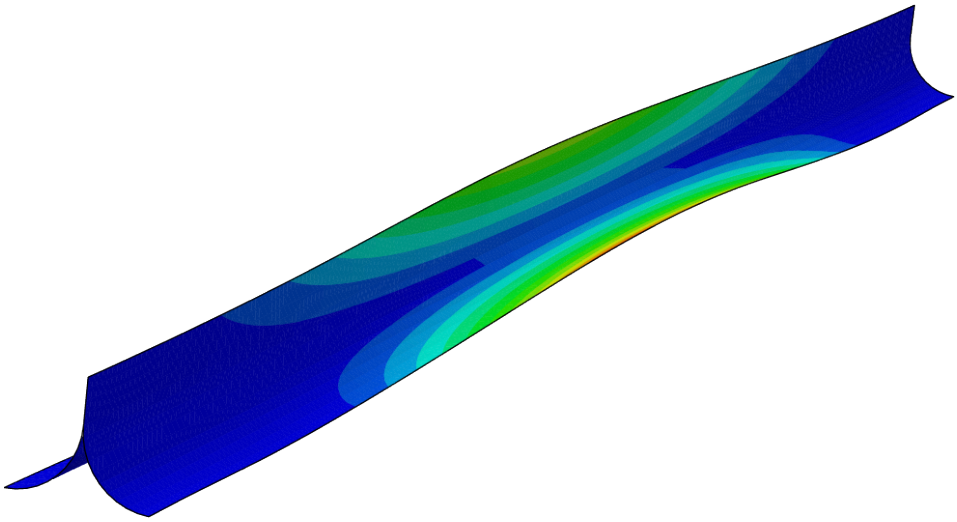

Figure 4.9: Buckling mode for an isotropic TRAC structure loaded by end moments M_Y, with $L = 500\,\text{mm}$, $r = 12.7\,\text{mm}$, $\theta_f = 90°$, $t = 0.1\,\text{mm}$ and $w = 8\,\text{mm}$. The associated buckling moment is $M_Y = 511\,\text{N mm}$.

able to estimate the buckling load of the simplified model with simply supported longitudinal edge quite well (less than 20% error), it was observed that the simply supported boundary condition along the web was not approximating adequately the actual connection between the inner flange and the web. By contrasting with the result obtained with the clamped longitudinal edge instead, the actual boundary condition along the web would be somewhere in between simply supported and clamped, which is to be expected as the connection at that location has bending stiffness due to the continuity of the material.

Table 4.2: Summary of the results obtained for the buckling of isotropic TRAC structure.

	N_x^0 [N mm^{-1}]	M_Y [N mm]
Rayleigh-Ritz Method, SS edge	-2.25	262
FEM, SS edge	-2.75	320
FEM, Clamped edge	-5.52	643
TRAC structure	-4.39	511

4.5 Extension to Symmetric Composite Laminates

The method to predict buckling moments presented in the previous section can be extended to structures made of orthotropic material. More specifically, the current section derives the stability equations (equivalent to Equations 4.14) and the second

variation of the potential energy (equivalent to Equation 4.16) for a shell made of composite material. One key assumption is that the laminate is symmetric, therefore there is no coupling between the in-plane and bending behavior of the shell. The equations derived in this section are general and can be used to solve a wide range of stability problems for such orthotropic cylindrical panels.

4.5.1 Second Variation of Total Potential Energy for Orthotropic Shells

For a symmetric laminate, the constitutive relations expressed in the shell cylindrical coordinate system are given by the expressions:

$$\begin{bmatrix} N_x \\ N_\phi \\ N_{x\phi} \end{bmatrix} = \begin{bmatrix} A_{11} & A_{12} & A_{16} \\ A_{12} & A_{22} & A_{26} \\ A_{16} & A_{26} & A_{66} \end{bmatrix} \begin{bmatrix} \varepsilon_x \\ \varepsilon_\phi \\ \gamma_{x\phi} \end{bmatrix} \quad \begin{bmatrix} M_x \\ M_\phi \\ M_{x\phi} \end{bmatrix} = \begin{bmatrix} D_{11} & D_{12} & D_{16} \\ D_{12} & D_{22} & D_{26} \\ D_{16} & D_{26} & D_{66} \end{bmatrix} \begin{bmatrix} \kappa_x \\ \kappa_\phi \\ \kappa_{x\phi} \end{bmatrix} \tag{4.35}$$

The strain energy is given by (Kollar and Springer, 2003)

$$U = U_m + U_b \tag{4.36}$$

where U_m and U_b are the membrane and bending strain energy, respectively, and are given by

$$U_m = \frac{r}{2} \iint \begin{bmatrix} \varepsilon_x & \varepsilon_\phi & \gamma_{x\phi} \end{bmatrix} \begin{bmatrix} A_{11} & A_{12} & A_{16} \\ A_{12} & A_{22} & A_{26} \\ A_{16} & A_{26} & A_{66} \end{bmatrix} \begin{bmatrix} \varepsilon_x \\ \varepsilon_\phi \\ \gamma_{x\phi} \end{bmatrix} dx d\phi \tag{4.37a}$$

$$U_b = \frac{r}{2} \iint \begin{bmatrix} \kappa_x & \kappa_\phi & \kappa_{x\phi} \end{bmatrix} \begin{bmatrix} D_{11} & D_{12} & D_{16} \\ D_{12} & D_{22} & D_{26} \\ D_{16} & D_{26} & D_{66} \end{bmatrix} \begin{bmatrix} \kappa_x \\ \kappa_\phi \\ \kappa_{x\phi} \end{bmatrix} dx d\phi \tag{4.37b}$$

The total potential energy is given by

$$\Pi = U + \Omega \tag{4.38}$$

where Ω is the potential energy of the applied loads and can be expressed as

$$\Omega = -\iint \left(N_x u_{,x} + N_\phi \frac{v_{,\phi}}{r} + N_{x\phi} \left(\frac{u_{,\phi}}{r} + v_{,x} \right) \right) dx d\phi \tag{4.39}$$

To obtain the first and second variation of the total potential energy, the displacements are assumed to be of the form

$$u = u_0 + u_1 \qquad v = v_0 + v_1 \qquad w = w_0 + w_1 \tag{4.40}$$

where u_0, v_0 and w_0 are the pre-buckling displacements and u_1, v_1 and w_1 are the increments. These expressions for the displacement components are first substituted in the kinematic equations 4.12, and then in the strain energy equations. The second variation is obtained by considering only the second-order terms of the increments. For this reason, the second variation of Ω is zero as it contains only linear terms of the displacement components.

The second variation of the total potential energy is obtained by combining the resulting equations, and can be expressed as

$$\begin{aligned}\frac{1}{2}\delta^2\Pi = \frac{r}{2}\iint \begin{bmatrix}\varepsilon_{x1} & \varepsilon_{\phi 1} & \gamma_{x\phi 1}\end{bmatrix}\begin{bmatrix}A_{11} & A_{12} & A_{16}\\ A_{12} & A_{22} & A_{26}\\ A_{16} & A_{26} & A_{66}\end{bmatrix}\begin{bmatrix}\varepsilon_{x1}\\ \varepsilon_{\phi 1}\\ \gamma_{x\phi 1}\end{bmatrix} dxd\phi \\ + \frac{r}{2}\iint \left(N_{x0}w_{1,x}^2 + N_{\phi 0}\frac{w_{1,\phi}^2}{r^2} + 2N_{x\phi 0}w_{1,x}\frac{w_{1,\phi}}{r}\right) dxd\phi \\ + \frac{r}{2}\iint \begin{bmatrix}w_{1,xx} & \frac{1}{r^2}w_{1,\phi\phi} & \frac{1}{r}w_{1,x\phi}\end{bmatrix}\begin{bmatrix}D_{11} & D_{12} & D_{16}\\ D_{12} & D_{22} & D_{26}\\ D_{16} & D_{26} & D_{66}\end{bmatrix}\begin{bmatrix}w_{1,xx}\\ \frac{1}{r^2}w_{1,\phi\phi}\\ \frac{1}{r}w_{1,x\phi}\end{bmatrix} dxd\phi\end{aligned} \tag{4.41}$$

where the strains are given by

$$\varepsilon_{x1} = u_{1,x} \qquad \varepsilon_{\phi 1} = \frac{v_{1,\phi} + w_1}{r} \qquad \gamma_{x\phi 1} = \frac{u_{1,\phi}}{r} + v_{1,x} \tag{4.42}$$

4.5.2 Stability Equations for Orthotropic Shells

For the two isotropic cases presented in the last two sections, the stability Equations 4.14a-b were used to express u_1 and v_1 as a function of w_1. For the orthotropic case, equivalent equations can be obtained by substituting the constitutive relations in Equations 4.8a-b. Then, as detailed for the isotropic case by Brush and Almroth, (1975), the displacements and loads are expressed as

$$u = u_0 + u_1 \qquad v = v_0 + v_1 \qquad w = w_0 + w_1 \tag{4.43}$$

$$N_x = N_{x0} + \Delta N_x \qquad N_\phi = N_{\phi 0} + \Delta N_\phi \qquad N_{x\phi} = N_{x\phi 0} + \Delta N_{x\phi} \tag{4.44}$$

where ΔN_x, ΔN_ϕ and $\Delta N_{x\phi}$ are the increments due to u_1, v_1 and w_1.

Substituting in Equations 4.8a-b, removing all the terms representing the equilibrium configuration (terms with displacement components with a 0 subscript), linearizing

by keeping only the first order terms, and neglecting the pre-buckling rotations $w_{0,x}$ and $w_{0,\phi}$, the first two stability equations for an orthotropic cylindrical shell are

$$\begin{aligned} A_{11}r^2u_{1,xx} + (A_{12} + A_{66})\,rv_{1,x\phi} + A_{12}rw_{1,x} + A_{66}u_{1,\phi\phi} \\ +A_{16}r\left(rv_{1,xx} + 2u_{1,x\phi}\right) + A_{26}\left(v_{1,\phi\phi} + w_{1,\phi}\right) = 0 \end{aligned} \tag{4.45a}$$

$$\begin{aligned} A_{22}\left(v_{1,\phi\phi} + w_{1,\phi}\right) + (A_{12} + A_{66})\,ru_{1,x\phi} + A_{66}r^2v_{1,xx} \\ +A_{16}r^2ru_{1,xx} + A_{26}\left(2rv_{1,x\phi} + rw_{1,x} + u_{1,\phi\phi}\right) = 0 \end{aligned} \tag{4.45b}$$

The orthotropic equivalent to Equation 4.14c can be obtained similarly.

Unlike the isotropic case, these equations generally cannot be decoupled. However, for the specific case of a balanced laminate, for which $A_{16} = A_{26} = 0$, they can be decoupled. In a balanced laminate, for every ply oriented at $+\theta$, there is a similar ply oriented at $-\theta$. This assumption is true for the $[\pm 45_{GFPW}/0_{CF}/\pm 45_{GFPW}]$ laminate presented in Chapter 2.

After removing the terms with A_{16} and A_{26}, the following steps are used to decouple Equations 4.45:

1. Apply $\frac{\partial^2}{\partial x^2}$ to Equation 4.45a and solve for $v_{1,xxx\phi}$ to obtain a first equation (i)
2. Apply $\frac{\partial^2}{\partial \phi^2}$ to Equation 4.45a and solve for $v_{1,x\phi\phi\phi}$ to obtain a second equation (ii);
3. Apply $\frac{\partial^2}{\partial x \partial \phi}$ to Equation 4.45b and substitute (i) and (ii) into the resulting expression.

The result is an equation that is only a function of u_1 and w_1. Applying the same procedure, but inverting Equations 4.45a and 4.45b, a second equation is obtained with only v_1 and w_1. These decoupled equations are

$$\begin{aligned} \left(A_{12}^2 + 2A_{12}A_{66} - A_{11}A_{22}\right)r^2u_{1,xx\phi\phi} - A_{11}A_{66}r^4u_{1,xxxx} \\ -A_{22}A_{66}u_{1,\phi\phi\phi\phi} + A_{22}A_{66}rw_{1,x\phi\phi} - A_{12}A_{66}r^3w_{1,xxx} = 0 \end{aligned} \tag{4.46a}$$

$$\begin{aligned} \left(A_{12}^2 + 2A_{12}A_{66} - A_{11}A_{22}\right)r^2v_{1,xx\phi\phi} - A_{22}A_{66}v_{1,\phi\phi\phi\phi} - A_{11}A_{66}r^4v_{1,xxxx} \\ + \left(A_{12}^2 + A_{12}A_{66} - A_{11}A_{22}\right)r^2w_{1,xx\phi} - A_{22}A_{66}w_{1,\phi\phi\phi} = 0 \end{aligned} \tag{4.46b}$$

4.5.3 Buckling Prediction Using Rayleigh-Ritz Method

The Rayleigh-Ritz method can be used to estimate the buckling load of an orthotropic cylindrical panel made from a balanced, symmetric laminate. The same simplified problem described in Figure 4.2 is studied here. The same shape function used in the isotropic case is assumed for $w_1(x, \phi)$

$$w_1(x, \phi) = \sin(\bar{m}x)\left(C_1 \sinh(\alpha\phi) + C_2 \sin\left(\bar{\beta}\phi\right)\right) \tag{4.47}$$

where

$$\bar{m} = m\pi/L \qquad\qquad \bar{\beta} = \pi/2\theta_f \tag{4.48}$$

The displacement field $u_1(x, \phi)$ and $v_1(x, \phi)$ can be obtained by solving Equations 4.46. The expressions are

$$u_1(x, \phi) = \cos(\bar{m}x)\left(C_1^u \sinh(\alpha\phi) + C_2^u \sin\left(\bar{\beta}\phi\right)\right) \tag{4.49a}$$

$$v_1(x, \phi) = \sin(\bar{m}x)\left(C_1^v \cosh(\alpha\phi) + C_2^v \cos\left(\bar{\beta}\phi\right)\right) \tag{4.49b}$$

where

$$\begin{aligned}
C_1^u &= \frac{C_1 A_{66}\bar{m}r\left(A_{12}\bar{m}^2r^2 + A_{22}\alpha^2\right)}{A_{11}A_{66}\bar{m}^4r^4 - \bar{m}^2r^2\alpha^2\left(A_{11}A_{22} - A_{12}^2 - 2A_{12}A_{66}\right) + A_{22}A_{66}\alpha^4} \\
C_2^u &= \frac{C_2 A_{66}\bar{m}r\left(A_{12}\bar{m}^2r^2 - A_{22}\bar{\beta}^2\right)}{A_{11}A_{66}\bar{m}^4r^4 + \bar{m}^2r^2\bar{\beta}^2\left(A_{11}A_{22} - A_{12}^2 - 2A_{12}A_{66}\right) + A_{22}A_{66}\bar{\beta}^4} \\
C_1^v &= \frac{C_1\alpha\left(\bar{m}^2r^2\left(A_{11}A_{22} - A_{12}^2 - A_{12}A_{66}\right) - A_{22}A_{66}\alpha^2\right)}{A_{11}A_{66}\bar{m}^4r^4 - \bar{m}^2r^2\alpha^2\left(A_{11}A_{22} - A_{12}^2 - 2A_{12}A_{66}\right) + A_{22}A_{66}\alpha^4} \\
C_2^v &= \frac{C_2\bar{\beta}\left(\bar{m}^2r^2\left(A_{11}A_{22} - A_{12}^2 - A_{12}A_{66}\right) + A_{22}A_{66}\bar{\beta}^2\right)}{A_{11}A_{66}\bar{m}^4r^4 + \bar{m}^2r^2\bar{\beta}^2\left(A_{11}A_{22} - A_{12}^2 - 2A_{12}A_{66}\right) + A_{22}A_{66}\bar{\beta}^4}
\end{aligned} \tag{4.50}$$

The force resultants are unchanged

$$N_{x0} = N_x^0(1 - \cos\phi) \qquad\qquad N_{\phi 0} = N_{x\phi 0} = 0 \tag{4.51}$$

The critical buckling load can then be obtained by substituting the shape functions and the force resultants into the second variation of the total potential energy, and solving for N_x^0. Specializing for a shell with the dimensions presented in Table 4.3, and using the A and D matrices for the laminate $[\pm 45_{GFPW}/0_{CF}/\pm 45_{GFPW}]$

Table 4.3: Dimensions and material properties for the orthotropic cylindrical shell.

r [mm]	θ_f	L [mm]	t [mm]
12.7	90°	500	0.08

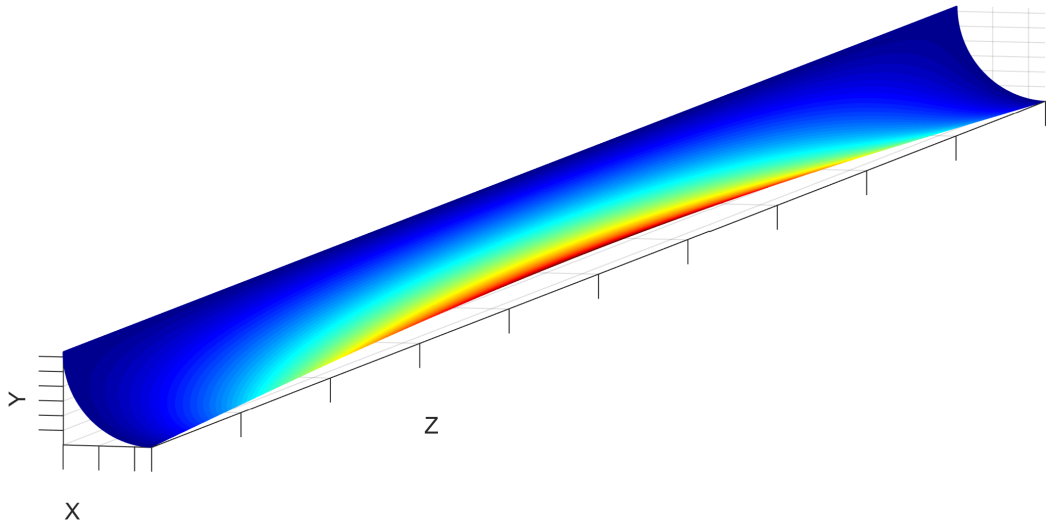

Figure 4.10: Analytical buckling mode for an orthotropic cylindrical shell loaded under non-uniform axial compression, simply supported on three sides and free along one longitudinal edge, with $L = 500\,\text{mm}$, $r = 12.7\,\text{mm}$, $\theta_f = 90°$ and $t = 0.08\,\text{mm}$. The associated buckling load is $N_x^0 = -1.89\,\text{N mm}^{-1}$.

described in Section 2.3, the estimated critical buckling load is $N_x^0 = -1.89\,\text{N mm}^{-1}$, with $m = 1$ and $\alpha = 1.28$. The corresponding mode shape, shown in Figure 4.10, is defined by $A_1 = 1$ and $A_2 = 1.63$.

This analytical prediction of the buckling edge stress can be compared with a numerical solution. The same model presented in Section 4.4 is used, changing the shell section to a *General Shell Stiffness* section in order to input the A and D matrices for the laminate. Figure 4.11 shows the buckling mode obtained from the simulation. The associated buckling load is $N_x^0 = -1.31\,\text{N mm}^{-1}$.

The analytical model overestimates the buckling load by 44% when compared with the numerical results, which is consistent with the Rayleigh-Ritz method giving in general an upper bound to the buckling load. It is also consistent with the findings of Jaunky and Knight, (1999), where they demonstrated that Donnell's equations overestimate the buckling load. However, while the analytical model predicts a single half-wavelength along the length of the shell, the numerical model displays a more complex buckling mode, with 12 half-waves along the length with an amplitude

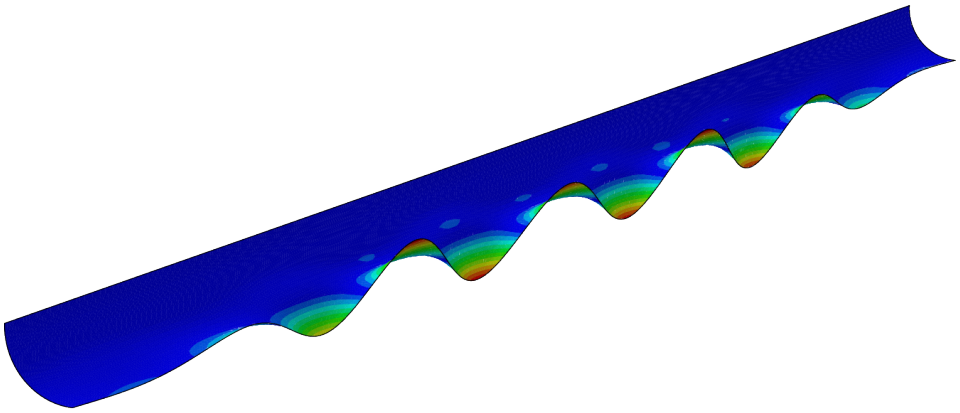

Figure 4.11: Finite element buckling mode for an orthotropic cylindrical shell loaded under non-uniform axial compression, simply supported on three sides and free along one longitudinal edge, with $L = 500\,\text{mm}$, $r = 12.7\,\text{mm}$, $\theta_f = 90°$ and $t = 0.08\,\text{mm}$. The associated buckling load is $N_x^0 = -1.31\,\text{N mm}^{-1}$.

that reaches a maximum at $L/2$. A shape function for w_1 with more terms could better predict the buckling load, for example

$$w_1(x, \phi) = \sin(\bar{m}_1 x) \sin(\bar{m}_2 x) \left(C_1 \sinh(\alpha\phi) + C_2 \sin(\bar{\beta}\phi)\right) \tag{4.52}$$

where $\bar{m}_1$ and $\bar{m}_1$ have different values of m. However, for such shape function, it is not possible to get exact functions for u_1 and v_1 using Equations 4.46a-b. Therefore, the current analytical prediction, while not optimal, is still a good upper bound to the buckling load, even if it neglects shorter wavelength buckling.

The buckling prediction from the simplified shell model can once again be compared with the buckling moment for a complete TRAC structure. Similarly to the isotropic case, the buckling of a TRAC structure with the dimensions described in Table 4.3, adding $w = 8\,\text{mm}$, was studied using the framework described in Chapter 3. The critical moment thus obtained is $M_Y = 147.3\,\text{N mm}^{-1}$. Using Equation 4.7, with $I_Y = 118\,\text{mm}^4$, this is equivalent to $N_x^0 = -1.27\,\text{N mm}^{-1}$. Figure 4.12 shows the corresponding mode shape.

Unlike the isotropic case, the buckling mode is only localized in the flange, with no rotation of the web. Therefore, it is expected that the simplified model, representing only the inner flange, would give a more accurate prediction. While the number of half-wavelengths in the case of the full TRAC structure (22) is higher than in the simplified shell model, the buckling load is only 3% different between the two numerical models. Furthermore, the assumption of a simply supported longitudinal edge seems to be more appropriate in the orthotropic case. A simulation of the simple

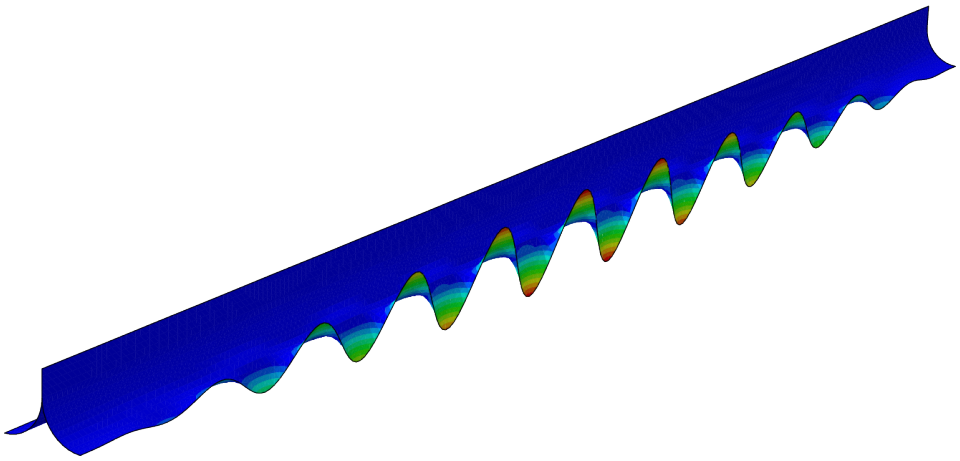

Figure 4.12: Buckling mode for an orthotropic TRAC structure loaded under pure moment, with $L = 500\,\text{mm}$, $r = 12.7\,\text{mm}$, $\theta_f = 90°$, $t = 0.08\,\text{mm}$ and $w = 8\,\text{mm}$. The associated buckling moment is $M_Y = 147.3\,\text{N mm}$.

cylindrical shell, but with clamped boundary condition, gives $N_x^0 = -1.51\,\text{N mm}^{-1}$. Table 4.4 summarizes the results.

Table 4.4: Summary of the results obtained for the buckling of orthotropic TRAC structure.

	N_x^0 [N mm^{-1}]	M_Y [N mm]
Rayleigh-Ritz Method, SS edge	-1.89	219.5
FEM, SS edge	-1.31	152.1
FEM, Clamped edge	-1.51	175.4
TRAC structure	-1.27	147.3

4.6 Conclusion

This chapter has presented an analytical method to predict the buckling moment of a TRAC structure loaded by pure moments. This was done by studying a simplified problem, where only the inner flange is present and the loading is a non-uniform axial compression. Using the Rayleigh-Ritz method with shallow-shell stability equations, the buckling load was estimated. For one specific isotropic TRAC structure, the buckling moment estimated using this method was shown to underestimate the buckling load predicted from finite element simulations by 49%. The difference was attributed to three factors. First, the actual buckling mode of the TRAC structure includes a torsional component which is not captured by the simplified model. Second, the single half-wave of the buckling mode does not fit well within the shallow-shell assumptions. Third, the high transverse bending

stiffness of the shell at the flange junction with the web is not well captured by a simply supported boundary conditions.

The method was also extended to orthotropic TRAC structures. To achieve this, the second variation of the total potential energy and the stability equations were derived for symmetric laminates, where there is no coupling between in-plane and out-of-plane behaviors. Furthermore, it was shown that for the specific case of a balanced laminate, the stability equations can be partially uncoupled. This method was shown to overestimate the buckling moment of a specific orthotropic TRAC boom by only 44% even if the guessed shape function did not capture the shorter wavelength features observed from simulation.

Chapter 5

STRUCTURE BEHAVIOR DURING COILING

Parts of this chapter were modified from the following publications:

Leclerc, Christophe, Pedivellano, Antonio, and Pellegrino, Sergio (2018). "Stress Concentration and Material Failure During Coiling of Ultra-Thin TRAC Booms". In: *2018 AIAA Spacecraft Structures Conference*. 2018–0690. Orlando, FL.

Leclerc, Christophe and Pellegrino, Sergio (2019). "Reducing Stress Concentration in the Transition Region of Coilable Ultra-Thin-Shell Booms". In: *AIAA Scitech 2019 Forum*. 2019–1522. San Diego, CA. DOI: 10.2514/6.2019-1522.

5.1 Introduction

5.1.1 Background

To achieve packaging, the TRAC structure needs to be subjected to two changes of curvature: flattening of the flanges, and coiling of both the flanges and the web around a cylindrical hub. A simple packaging concept achieves coiling by means of a mechanism that applies a tension F at the tip of the structure while a hub with radius R is rotated at angular velocity ω, as shown in Figure 5.1. The tension is necessary to stabilize the structure during coiling and ensure that it conforms well to the hub. Using this concept, the two changes of curvature are imposed simultaneously in a transition region between the fully deployed configuration and the fully coiled configuration.

Initial research on TRAC boom coiling focused on thick composite boom (flange thickness of $\sim$1 mm), and found a lower and an upper limit on the hub radius (Banik and Murphey, 2010; Roybal, Banik, and Murphey, 2007). The lower limit was based on longitudinal strain considerations, while the upper limit was found experimentally to avoid inner flange bifurcation, which occurs when the inner flange locally and partially opens out instead of being fully flattened and conforming to the hub. In both cases, only the fully coiled region was considered to derive these limits. Murphey, Turse, and Adams, (2017) extended this work to thinner composite booms, and looked at the high localized strains in the fully coiled region when flange

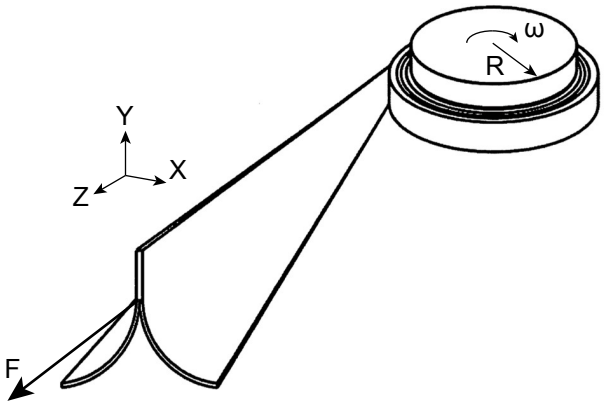

Figure 5.1: TRAC structure partially coiled around a hub with radius R. The hub rotates at angular velocity ω and a force F tensions the structure. X, Y and Z form the global coordinate system, where Z is aligned with the axis of the structure, Y is parallel to the web, and X is normal to the web (Figure modified from Murphey and Banik, 2011).

bifurcation occurs. A study by Fernandez, (2017) also looked experimentally at the minimum coiling radius for TRAC booms made of ultra-thin materials. The smallest successful coiling radius was 25 mm, for a boom where each flange is a single, 85 µm thick, layer of carbon fiber plain weave. This study also looked at bi-stable TRAC booms, where the boom is stable both in the deployed and the coiled configuration. However, this limits the applications, as some packaging schemes have booms coiled in opposite directions (Arya, Lee, and Pellegrino, 2016).

More recently, the inner flange buckling in the transition region of TRAC booms during coiling was studied by Cox and Medina, (2018, 2019), focusing on large cross-section ($r = 85$ mm) and large hubs ($R = 185.5$ mm). Reducing the flange arc length was shown to reduce the maximum strain observed in the transition region, or even prevent completely inner flange buckling. However, reducing the flange arc length while keeping the flange radius constant significantly reduces the bending stiffness in the deployed configuration. Multiple laminates were also studied, showing that the stress peak in the transition region can be somewhat mitigated by choosing a suitable laminate. A different study (H. Yang et al., 2019) looked at coiling of large TRAC booms ($r = 140-160$ mm) around a large hub ($R = 125$ mm), adding flattening rollers upstream of the hub. The influence of flange radius and opening angle, and web width were also studied.

These recent studies have shown that using ultra-thin composites in TRAC structures can reduce significantly the packaged volume, extending the range of applications.

However, greatly decreasing the thickness of the structures has brought up new issues specific to ultra-thin shells, such as inner flange buckling and blossoming of the coiled region of the structures, both having a negative impact on the packaging efficiency and on the deployment behavior. The current study aims at obtaining a better understanding of the coiling process of ultra-thin composite TRAC structure, to enable more efficient packaging around small hubs.

5.1.2 Preliminary Coiling Experiments

Preliminary experiments were first performed on three samples to observe the coiling behavior. The laminate used was a $[0/90]_S$ made of unidirectional carbon fiber/epoxy prepreg with a ply thickness of 17.8 µm, for a total flange thickness of 71 µm. The measured cross-section parameters, using the method described in Section 2.5, were $r = 10.6$ mm, $\theta_f = 105°$ and $w = 8$ mm. Coiling was done using the experimental setup described in Section 5.4. Hubs with three different radii were used: 31.8 mm, 25.4 mm, and 19.1 mm (1.25", 1" and 0.75"). Two important findings were obtained from these preliminary experiments.

First, a significant tension force (15 N) is necessary to ensure that the TRAC structure conforms well to the hub. Similar to tape springs, TRAC structures have a natural coiling radius which is obtained by minimizing the strain energy in the packaged configuration (Wilson, 2017). This natural radius can be obtained from the following equation:

$$R_N = \sqrt{\frac{2\left(r^2\theta_f + rw\right)D_{11} + \frac{1}{2}t^2 rwA_{11}}{2\theta_f D_{22}}} \tag{5.1}$$

Using the material properties for this laminate (see Section 5.3) and the cross-section parameters, the natural coiling radius for the test samples is 35.4 mm, larger than any of the hubs used. Therefore, the tension force is needed to prevent inner flange bifurcation in the coiled configuration.

Second, while the predicted longitudinal strain in the coiled region for the three hub sizes (0.2%, 0.3%, and 0.4% for hub radii of 31.8 mm, 25.4 mm, and 19.1 mm, respectively) was well below the failure strain of carbon fibers, material failure was observed on two of the three samples when coiled around the largest hub, and on all samples when coiled around the hub with a radius of 25.4 mm. In all cases, small cracks were observed in the inner flange, very close to the web.

A closer observation of the inner flange during coiling showed a buckling phenomenon in the transition region between the fully deployed configuration and the fully coiled configuration. This inner flange buckling creates a region of very high localized curvature, right where the flange is merging into the web. Figure 5.2 shows this phenomenon. In this picture, the hub has a radius of 25.4 mm, and the web is located towards the bottom of the image. The buckling can be clearly seen initiating from the web and propagating toward the free edge of the flange.

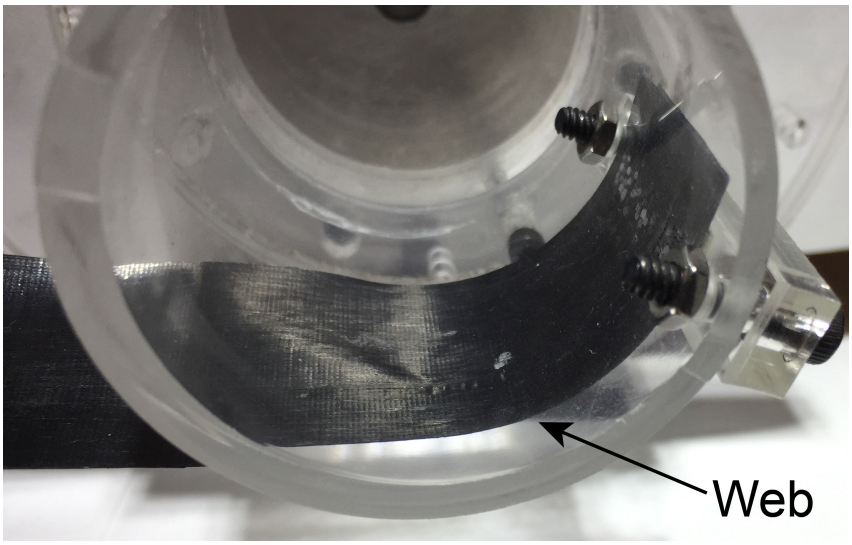

Figure 5.2: Inner flange buckling in the transition region during coiling of a TRAC structure around a hub with $R = 25.4$ mm.

Following this preliminary set of experiments, it is clear that the prediction of maximum strain simply due to the two changes of curvature does not accurately predict the actual stress imposed on the inner flange during coiling in the case of TRAC structures made with ultra-thin composites. The location of the high localized curvature discovered in experiments coincides with the location of observed material failure, suggesting that the buckling phenomenon in the transition region is the cause of failure.

5.1.3 Objectives and Scope

Therefore, the objectives of the current study are 1) to better understand the buckling event observed in the transition region during coiling, 2) to mitigate the resulting high stress concentration in order to allow coiling around small hub without failure, and 3) to validate experimentally the findings.

In this chapter, a numerical simulation framework is first proposed to study the

coiling behavior of ultra-thin TRAC structures. Using this simulation tool, high stress concentrations were observed in the transition region during the coiling of a structure made with a $[0/90]_S$ carbon fiber laminate. To mitigate this issue, a different laminate, a hybrid made both from carbon and glass fibers, is proposed. This new composite laminate reduced significantly the observed stress concentration. The results are validated through experiments where the measured curvature of the inner flange in the transition region is compared with numerical results. Finally, a discussion concludes this chapter.

5.2 Numerical Simulation Framework

To better understand the mechanics of coiling ultra-thin composite TRAC structure, a numerical simulation framework was developed. The model was developed using the commercial finite element software Simulia Abaqus 2018. Due to both multiple contacts and large nonlinear shell deformation, the coiling process is challenging to accurately reproduce in simulation. Therefore, multiple models were created and tested until a suitable option was found.

The simulations use an implicit direct-integration dynamic formulation, a trade-off between static implicit and explicit approaches. It converges to a final static response by using implicit time integration where artificial inertia effects and numerical dissipation are introduced to help convergence of unstable behavior, for example due to nonlinearities and contacts.

The first model was created to replicate as closely as possible the experimental setup (see Section 5.5.1), an exploded view of which can be seen in Figure 5.3. It was composed of a TRAC structure made of two separate flanges bonded together along the web using a tie constraint, a rigid cylindrical hub, and a rigid clamp which was a thin rectangular plate. In a first step, the rigid hub and the rigid clamp were moved toward each other to flatten the TRAC cross-section at the extremity closest to the hub (clamped end). The second step added the tension at the free end of the structure, and the last step performed the coiling. The structure coiling was driven by imposing an angular rotation to the hub, and by defining a rough contact (contact preventing any tangential slip) region between the hub and a small section of the clamped end to ensure that the structure would become coiled on the hub. This coiling, driven by friction, closely matched the experimental setup described in Section 5.5.1.

While this model was able to give some results, convergence was highly sensitive

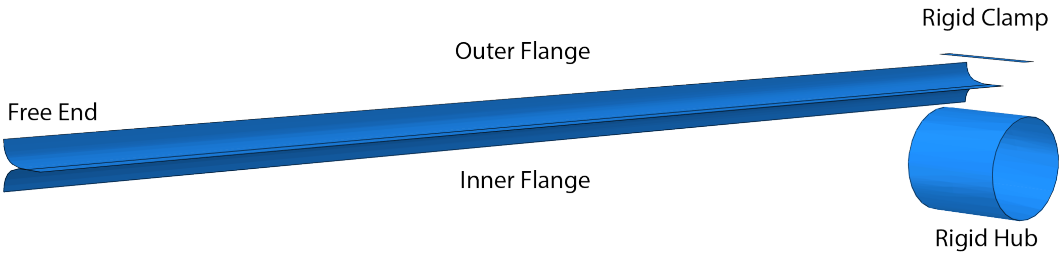

Figure 5.3: Initial simulation model. The structure is composed of two separate flanges (inner and outer) bonded along the web, and a rigid clamp flattens the end of the structure against the hub.

to small changes in either cross-section geometry or material properties. A small change in the stiffness properties, for example, would cause a previously working simulation to fail to reach convergence in any of the three steps. Two aspects of this simulation model were problematic.

First, two types of contacts needed to be enforced, and the contact formulation changed during the simulation. During the first step, all contacts were frictionless to allow flattening of the cross-section. Once flattening was achieved, the contact formulation between the clamped end of the structure (last 5 mm) and both the hub and the clamp was changed to a rough contact, while contacts everywhere else did not change.

Second, two rigid bodies (clamp and hub) were used to flatten the clamped end of the structure. Hence, convergence of the simulations was highly sensitive to the final distance between those two bodies. If this distance was exactly equal to the total thickness of the flattened structure (twice the flange thickness), penetration was often observed, and convergence would not be obtained as the solver could not find an equilibrium solution. However, if the distance was too large, there was no rough contact between much of the structure and the hub, and therefore the contact forces between the hub and the structure were transferred through a very small number of elements. A distance of twice the total thickness was found to work for some cases, but convergence could not be achieved for other cases.

While this first model closely followed the experimental setup, the convergence issues described above prevented it to be used for complete studies of the coiling behavior of TRAC structures. Therefore, a new model was developed to address the shortcomings of the first one.

The new model consists of three pieces: a shell structure, defined by geometric

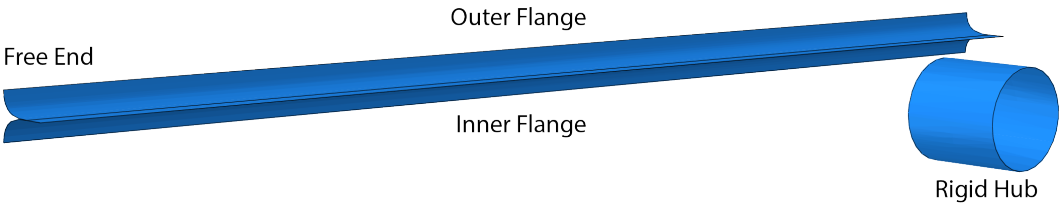

(a) Initial configuration of the model. The structure is composed of two separate flanges (inner and outer) bonded along the web.

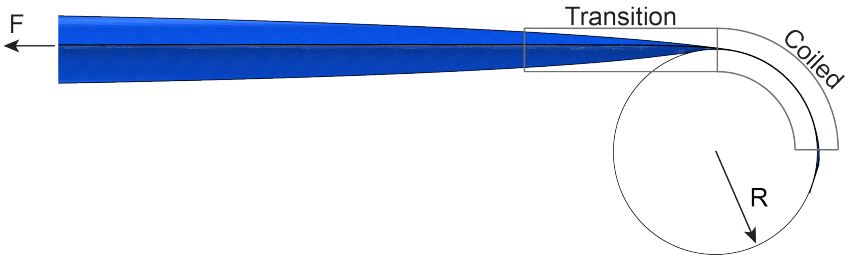

(b) Coiled model under tension F with the two regions of interest: Transition and Coiled.

Figure 5.4: Finite element model of coilable structure.

and mechanical parameters; a coiling mechanism (hub), defined by the radius R; and a tension force F applied axially. The structure is modeled using reduced integration four-node quadrilateral thin-shell elements (S4R). It is composed of an inner flange (in contact with the hub) and an outer flange, modeled separately and bonded together using tie constraints along the web. The structure is modeled as a cylindrical shell made of rigid quadrilateral elements.

To prevent issues related to the flattening process, the rigid clamp was removed and replaced by pressure applied directly on the top flange. A pressure of 30 kPa was found to be sufficient to flatten the cross-section. It was applied on both the web and the flange over a length of 5 mm from the clamped end of the structure, which is the same area that was previously covered by the clamp.

Another key addition to this model is a reference point located at the center of the hub. All six degrees of freedom for the nodes from the web located at the clamped end are kinematically coupled to this reference point. Hence, coiling is achieved by applying a rotation boundary condition to this reference point, which directly drives the clamped end of the structure. Therefore, rough contact is no longer necessary, and only one type of contact (frictionless) is enforced during the simulation.

The full model can be seen in Figure 5.4a. Figure 5.4b shows the structure partially coiled around the hub, with the two regions of interest, transition and fully coiled, marked.

The simulation consists of the following three steps:

1. The cross-section is flattened at the clamped end by moving the hub towards the structure while pressure is applied on the top flange;
2. An axial load is applied at the free end of the structure;
3. The structure is coiled around the hub by imposing an angular velocity to the hub and the reference point.

During the first step, the web at both the clamped and the free ends has all six degrees of freedom constrained. During the second step, the tension load is applied to all web nodes at the free ends, which are kinematically coupled together. In this step, the displacement in the axial direction is freed to allow the structure to stretch under tension. Also, to facilitate convergence in this step, additional constraints are temporarily applied at the nodes of the web along its full length, preventing any displacement other than along the axis of the structure. These constraints are removed prior to the third step.

The structure material properties are defined as a *General Shell Stiffness* section, where the ABD matrix can be directly used. During the simulation, the mid-plane strains $\boldsymbol{\varepsilon}^0$ and curvatures $\boldsymbol{\kappa}$ are recorded. Using this data, the local strains and stresses in the shell coordinate system (longitudinal x, transverse y) can be computed across the full thickness of the laminate using the following equations:

$$\begin{bmatrix} \varepsilon_x \\ \varepsilon_y \\ \gamma_{xy} \end{bmatrix} = \begin{bmatrix} \varepsilon_x^0 \\ \varepsilon_y^0 \\ \gamma_{xy}^0 \end{bmatrix} + z \begin{bmatrix} \kappa_x \\ \kappa_y \\ \kappa_{xy} \end{bmatrix} \tag{5.2}$$

$$\begin{bmatrix} \sigma_x \\ \sigma_y \\ \sigma_{xy} \end{bmatrix} = \bar{\boldsymbol{Q}} \begin{bmatrix} \varepsilon_x \\ \varepsilon_y \\ \gamma_{xy} \end{bmatrix} \tag{5.3}$$

where $\bar{\boldsymbol{Q}}$ corresponds to the transformed stiffness matrix of the corresponding ply, and z is the thickness coordinate representing the position in the shell, where $z = 0$ is the mid-surface. To obtain the stresses in the material principal directions in each ply, the following equation can be used:

$$\begin{bmatrix} \sigma_1 \\ \sigma_2 \\ \sigma_{12} \end{bmatrix} = \boldsymbol{T} \begin{bmatrix} \sigma_x \\ \sigma_y \\ \sigma_{xy} \end{bmatrix} \tag{5.4}$$

where $\boldsymbol{T}$ is the rotation matrix that accounts for ply orientation.

Contacts being an important part of this simulation, the right contact properties need to be used. A single *General Contact* interaction is defined and is assigned to two pairs of surfaces: the two inner surfaces of the flanges, and the outer surface of the inner flange with the hub surface. The normal behavior of this contact is defined as "hard" (not allowing any penetration), and the constraint enforcement method is set to "Augmented Lagrange," which was found to be more stable than the default method. The tangential behavior is frictionless. As a *General Shell Stiffness* section does not have any information about the shell thickness, this information is input directly into the contact formulation as *Surface Thickness Assignments* to ensure proper contact distances.

Due to the large amount of elements and contacts, this model is computationally expensive to run. To reduce the runtime to about 4 hours, a rotation of only 0.5 turns is imposed to simulate coiling.

A study was performed to find the optimal mesh size. While increasing the number of elements across the arc length of the flange from 30 to 40 changed the maximum compressive stress by 0.7%, increasing from 40 to 50 only changed the stress by 0.02%. Therefore, the mesh size was fixed at 0.7 mm, which corresponds to 40 elements across the transverse direction in the flange and the web combined.

This model was shown to be much more stable than the previous one, as no convergence issues were observed while varying both the cross-section geometry and the material properties. Hence, this model was used for all simulations described next.

5.3 Simulation Results

Simulations were run using the geometry of the samples presented in Section 5.1.2, with a hub radius of 25.4 mm and a structure length of 470 mm. The laminate is $[0/90]_S$ made of unidirectional carbon fiber prepreg. Each ply consists of T800 carbon fiber with an epoxy resin and has an areal density of 17 g m^{-2}, as described in Chapter 2. Table 5.1 contains the ply properties. Using the Classical Lamination Theory, the A and D matrices for this laminate are

$$\boldsymbol{A} = \begin{bmatrix} 4805 & 163 & 0 \\ 163 & 4805 & 0 \\ 0 & 0 & 533 \end{bmatrix} \mathrm{N\,mm^{-1}} \tag{5.5}$$

$$\boldsymbol{D} = \begin{bmatrix} 3.386 & 0.0683 & 0 \\ 0.0683 & 0.651 & 0 \\ 0 & 0 & 0.224 \end{bmatrix} \mathrm{N\,mm} \tag{5.6}$$

while the $\boldsymbol{B}$ matrix is zero due to the laminate symmetry.

Table 5.1: Material properties of 17 GSM unidirectional carbon fiber/epoxy prepreg tape.

E_1 [GPa]	E_2 [GPa]	G_{12} [GPa]	ν_{12}	t [µm]
128	6.5	7.5	0.35	17.75

Figure 5.5 shows the nomenclature for the plies in the laminate, and the local curvilinear shell coordinate system. The x axis is longitudinal, y axis is transverse, and z axis is normal to the shell. The stress can be computed at any point throughout the thickness, but the most interesting locations are at the interfaces between two plies or at the surfaces. These locations are labeled based on their thickness coordinate, z_i for the inner flange and z_o for the outer flange. The thickness coordinate value is 0 at the mid-plane of each flange, and increases going away from the hub.

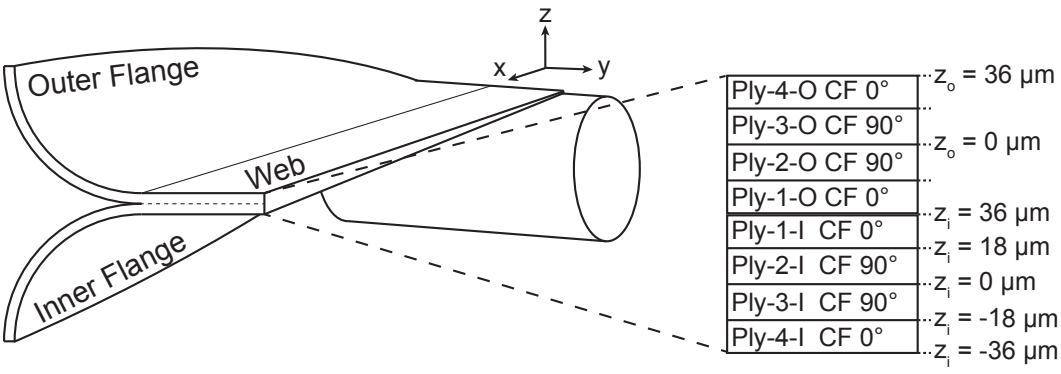

Figure 5.5: Naming convention for the individual plies in each flanges for the $[0/90]_S$ carbon fiber TRAC structure, and definition of the local shell coordinate system (x, y, z). x is along the axis of the structure, y is transverse along the flange, and z is normal to the shell. Thickness coordinates (z_i and z_o) for both flanges are also defined.

The maximum stresses in the fully coiled region are obtained using the following equations:

$$\Delta\kappa_x = \frac{1}{R} \quad \text{and} \quad \Delta\kappa_y = \frac{1}{r} \tag{5.7}$$

$$\sigma_{x,max} = \bar{Q}_{xx} \cdot \varepsilon_{x,max} = \pm\Delta\kappa_x \bar{Q}_{xx} z^* = \pm\frac{\bar{Q}_{xx} z^*}{R} \tag{5.8}$$

$$\sigma_{y,max} = \bar{Q}_{yy} \cdot \varepsilon_{y,max} = \pm\Delta\kappa_y \bar{Q}_{yy} z^* = \pm\frac{\bar{Q}_{yy} z^*}{r} \tag{5.9}$$

In equations 5.8 and 5.9, z^* corresponds to the location of maximum stress. Due to fiber orientation, the maximum stress is always in the fiber direction. Therefore, for σ_x, the maximum stress is on the flange surfaces, and for σ_y, the maximum stress is in Ply-2 and Ply-3, at their interface with Ply-1 and Ply-4 respectively.

In the flanges, the radius of curvature changes from 0 to R in the x direction, and from r to 0 in y. The web changes curvature only in the x direction. The equation for the longitudinal stress σ_x assumes that the two flanges are coiled together without relative shear displacement, which is true in the web. Therefore, the longitudinal stress is always compressive in the inner flange, and goes from a maximum in Ply-4-I at $z_i = -36\,\mu m$ (negative value from equation 5.8 with $z^* = t$), to zero in Ply-1-I at $z_i = 36\,\mu m$. Similarly, σ_x is always positive in the outer flange, going from zero in Ply-1-O at $z_o = -36\,\mu m$ to a maximum value in Ply-4-O at $z_o = 36\,\mu m$. The transverse stress goes from a maximum tensile value in Ply-3-I at $z_i = -18\,\mu m$, to a maximum compressive value in Ply-2-I at $z_i = 18\,\mu m$.

Using the laminate material properties, the maximum estimated stresses in the fully coiled region are $\sigma_{x,max} = \pm 360$ MPa and $\sigma_{y,max} = \pm 216$ MPa. However, during the preliminary experiments presented in Section 5.1.2, high curvature changes were observed in the transition region, meaning that higher stress values are expected.

Figure 5.6 shows the simulation results for coiling around a hub of 25.4 mm. The hub has been hidden to expose the inner flange. The transverse black line corresponds to the top of the hub, where the inner flange is fully in contact with it. The contour map displays the change in longitudinal curvature $\Delta\kappa_x$ in Figure 5.6a and in transverse curvature $\Delta\kappa_y$ in Figure 5.6b.

The change in longitudinal curvature in the fully coiled region is $\pm 39\,m^{-1}$, corresponding to $1/R$ (due to sign convention in Abaqus, the value is negative for the

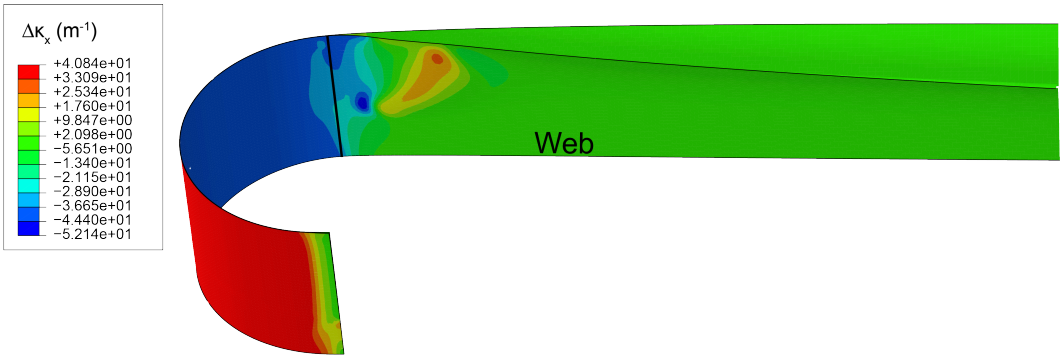

(a) Longitudinal curvature changes ($\Delta\kappa_x$, m^{-1}).

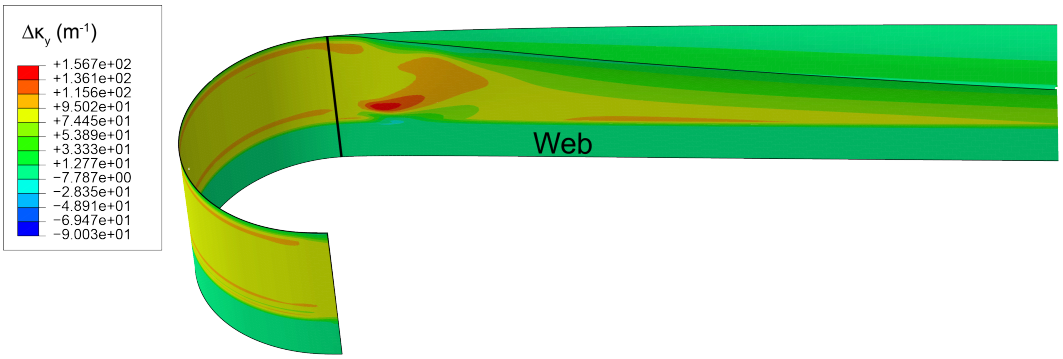

(b) Transverse curvature changes ($\Delta\kappa_y$, m^{-1}).

Figure 5.6: Curvature plots from simulation results for the $[0/90]_S$ carbon fiber TRAC structure.

inner flange and positive for the outer flange). As expected, the change in transverse curvature in the web is always zero. In the fully coiled region, the change of transverse curvature in the flanges is $94\,\mathrm{m}^{-1}$, corresponding to $1/r$.

However, the most interesting feature can be found on the inner flange, in the transition region between the deployed and coiled parts of the structure. One can notice a high localized curvature in this region, most notably in the transverse curvature. It starts close to both the web and the contact point with the hub and propagating toward the free edge of the flange. This matches well with the buckle observed in the experiments.

The stress distribution in the transition region can be used to better understand the effect of this localized curvature. Figures 5.7 and 5.8 show the stress components in the fiber orientation at different point across the thickness for the inner flange. The outer flange is not shown here as no localized curvature was observed in its transition region, leading to lower stresses when compared to the inner flange.

Due to the large difference in orthotropic stiffness, the stress components in the fiber

direction are always much higher. Therefore, Figure 5.7 displays the longitudinal stress distribution (σ_x) for Ply-1-I and Ply-4-I at different values of z_i. Figure 5.7a corresponds to Ply-1-I at the surface touching the outer flange, Figure 5.7b to Ply-1-I at the interface with Ply-2-I, Figure 5.7c to Ply-4-I at the interface with Ply-3-I, and Figure 5.7d to Ply-4-I at the surface in contact with the hub.

Figure 5.8 displays the transverse stress distribution (σ_y) for Ply-2-I and Ply-3-I. Figure 5.8a corresponds to Ply-2-I at the interface with Ply-1-I, Figure 5.8b to Ply-2-I at z_i =0 µm, and Figure 5.8c to Ply-3-I at the interface with Ply-4-I.

To better display the results, the plots show the stress distribution in the inner flange unwrapped from the hub and projected onto a plane. The coordinate system is the local shell system, where x is the longitudinal axis ($x = 0$ at the clamped end), and y is the transverse axis ($y = 0$ at the root of the web). The plots are centered around the location of contact between the structure and the hub, marked as a black vertical line. The black horizontal line separates the flanges from the web. Only the stresses in a 8 cm long region of the structure are shown, because it encompasses both the fully coiled region and the transition region.

Some stress concentration can be observed in the longitudinal direction (Figure 5.7). The maximal tensile load (270 MPa) is located in the transition region, at the free edge, and is mostly constant across to full thickness. A compressive stress is observed in the transition region of Ply-1-I, but the maximum value in this region is still less than the stress in the coiled region. The maximum longitudinal compressive stress (−355 MPa) is located in Ply-4-I, at the surface in contact with the hub ($z_i = -36$ µm), in the web region. This matches well with the predicted value from Equation 5.8, which gave −360 MPa. Similarly, the longitudinal stress in the web at the interface between the inner flange and outer flange (Figure 5.7a) is zero, as expected.

However, the stress concentration in the transition region is much more significant in the transverse direction (σ_y). Across only half of the flange thickness (from Ply-2-I, $z_i = 18$ µm to Ply-3-I, $z_i = -18$ µm), the transverse stress varies from high compression (−412 MPa) to high tension (343 MPa). These values are both higher than the corresponding maximum observed in the longitudinal direction for the inner flange. Furthermore, this zone of very high stress is highly localized, starting in the flange very close from both the web and the line of contact with the hub. In the coiled region, Equation 5.9 (±216 MPa) provided a good prediction of the stress, with values between 210 MPa and 220 MPa at the flange surface, zero stress in the

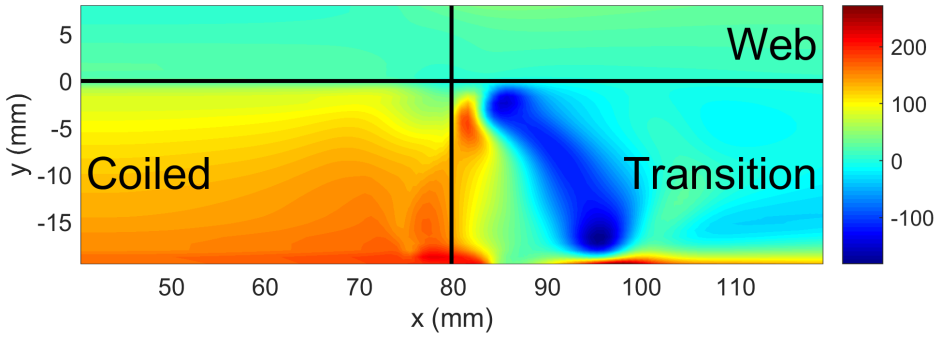

(a) Ply-1-I, $z_i = 36\,\mu m$

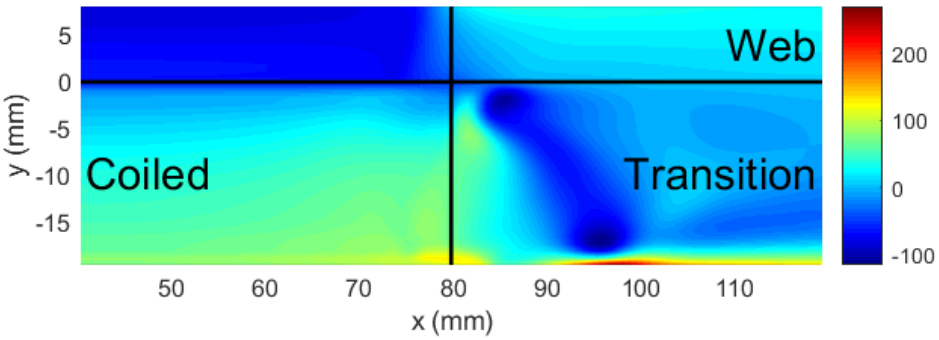

(b) Ply-1-I, $z_i = 18\,\mu m$

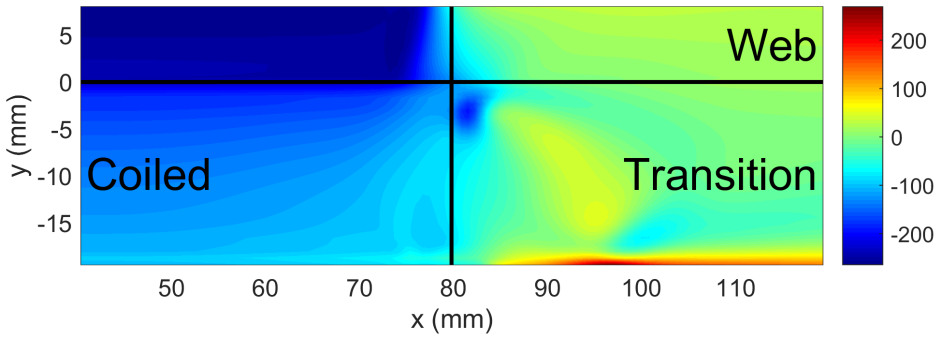

(c) Ply-4-I, $z_i = -18\,\mu m$

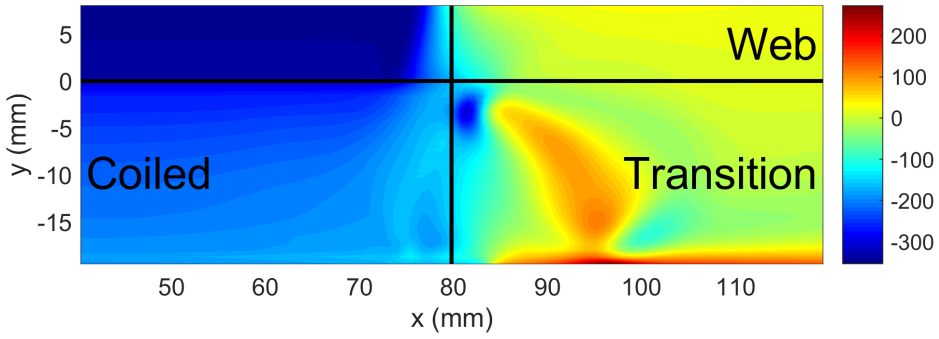

(d) Ply-4-I, $z_i = -36\,\mu m$

Figure 5.7: Longitudinal stress (σ_x, MPa) in the inner flange of the $[0/90]_S$ carbon fiber TRAC structure.

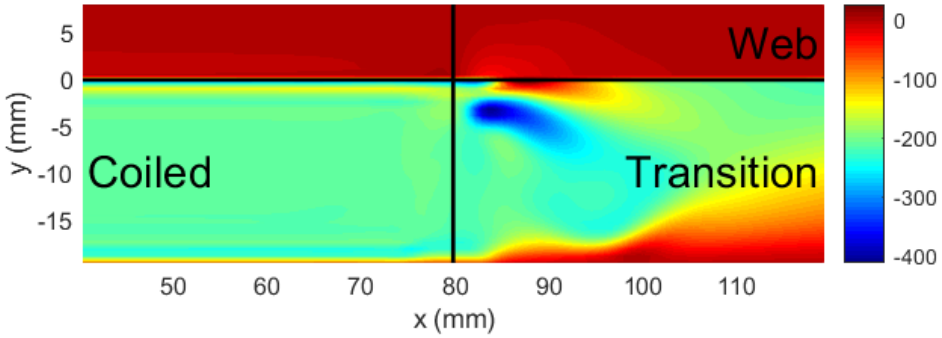

(a) Ply-2-I, $z_i = 18\,\mu m$

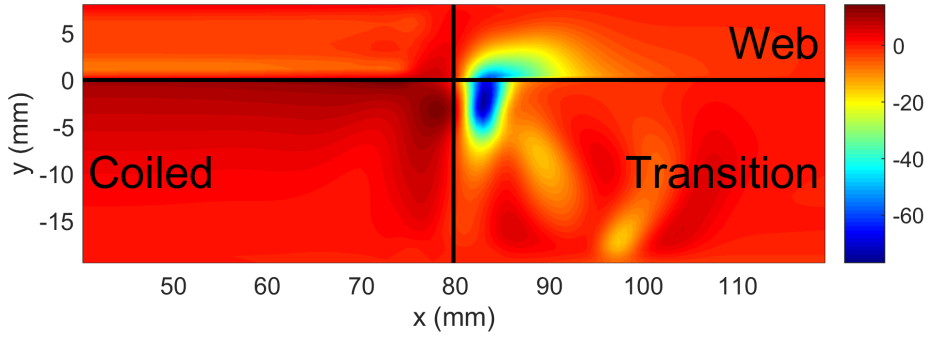

(b) Ply-2-I, $z_i = 0\,\mu m$

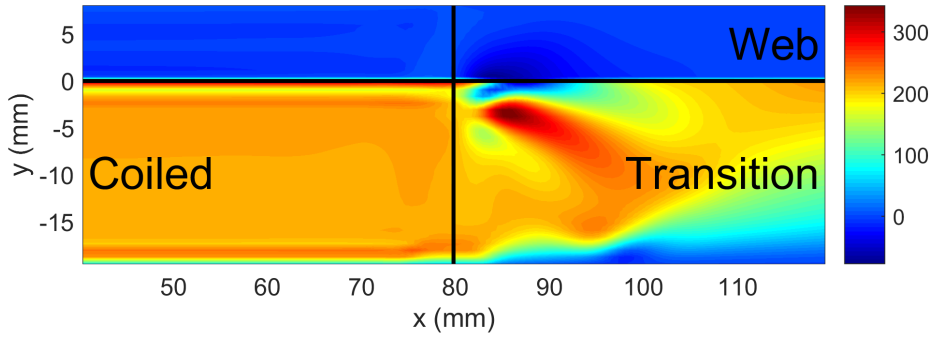

(c) Ply-3-I, $z_i = -18\,\mu m$

Figure 5.8: Transverse stress (σ_y, MPa) in the inner flange of the $[0/90]_S$ carbon fiber TRAC structure.

web, and zero stress at $z_i = 0\,\mu m$.

This simulation shows that the high localized curvature observed in the experiments is due to a combination of the coiling geometry and the TRAC structure geometry. While some stress concentration is observed in the longitudinal direction, the highest stress values are seen in the transverse direction. Indeed, in the fully coiled region, the maximum compressive stress ($-360\,MPa$) is only 87% of the maximum values in the transition region. Therefore, reducing this stress concentration is important to avoid failure when coiling a TRAC structure around small hubs.

5.4 Reducing Stress Concentration by Changing Flange Laminate

The simulation results for the TRAC structure made of a $[0/90]_S$ laminate showed stress concentration in the transition region, particularly in the transverse direction. Therefore, one solution to reduce the stress is to remove altogether the 90° plies, and replace them by layers of plain weave glass fiber fabric to give some in-plane shear and transverse strength to the laminate. By orienting the glass fiber plies at ±45°, no fibers are directly in the transverse direction. Furthermore, the glass fiber plain weave is tougher and has a higher strain limit when compared to carbon fiber. The idea of having a single ply of unidirectional carbon fiber composite oriented at 0° sandwiched between two plies of a plain weave oriented at 45° to obtain a very flexible laminate was first proposed by Pollard and Murphey, (2006). Structures using this type of laminate were studied by multiple authors (Khan, Borowski, and Taha, 2016; Murphey et al., 2015; M. Peterson and Murphey, 2013).

As the structure mechanical properties in the deployed configuration are mainly driven by the longitudinal fibers, similar properties can be achieved by keeping the same thickness of carbon fiber prepreg in the 0° direction. Also, to reduce the longitudinal stress as much as possible, it is optimal to keep the carbon fiber prepreg in the center of the laminate. The resulting laminate is $[\pm 45_{GFPW}/0_{CF}/\pm 45_{GFPW}]$, where $GFPW$ denotes a glass fiber plain weave prepreg, and CF denotes a unidirectional carbon fiber prepreg tape. The corresponding material properties for this laminate were given in Section 2.3.

While the corrected ABD matrix is used as explained in Section 2.3, Equation 5.3 uses ply level properties to compute the stress components in the laminate. Therefore, the nominal ply properties from Table 2.2 are used to compute the stresses throughout the thickness of the flanges.

The simulation framework presented in Section 5.2 can be used to study this new

laminate and understand the effects of replacing the 90° carbon fiber plies by a glass fiber plainweave oriented at 45°. Figure 5.9 shows the nomenclature for the plies in this laminate. A simulation was performed using the same cross-section geometry ($r = 10.6$ mm, $\theta_f = 105°$ and $w = 8$ mm) than the full carbon fiber laminate. Figure 5.10 shows the curvature plots extracted from the simulation results.

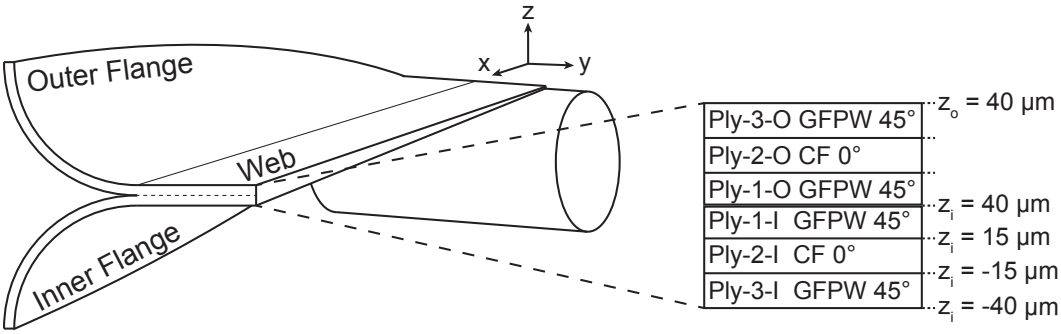

Figure 5.9: Naming convention for the individual plies in each flanges for the $[\pm 45_{GFPW}/0_{CF}/\pm 45_{GFPW}]$ TRAC structure, and definition of the local shell coordinate system (x, y, z). x is along the axis of the structure, y is transverse along the flange, and z is normal to the shell. Thickness coordinates (z_i and z_o) for both flanges are also defined.

When compared with the previous laminate, similar observations can be made from these curvature plots. The transverse curvature is always zero in the web, and both curvatures in the fully coiled region match with the predictions from flattening and coiling. Regions of high curvature can also be observed in the transition region. However, the maximum curvature is now smaller ($138\,\mathrm{m}^{-1}$ versus $157\,\mathrm{m}^{-1}$) in the transverse direction, and higher in the longitudinal direction ($-78\,\mathrm{m}^{-1}$ versus $-52\,\mathrm{m}^{-1}$).

As there are no fibers directly in the transverse direction, only the longitudinal stress in the carbon fiber ply (Ply-2-I) will be studied. Figure 5.11 shows the stress plots at three locations through the thickness of the carbon fiber ply. While some stress concentration can be observed in the transition region, the location of the maximum compressive stress (-281 MPa) is at $z_i = -15\,\mu$m, in the web, in the fully coiled region. This matches well with the expected result, obtained using Equation 5.8, of -278 MPa. Once again, the maximum tensile stress is located in the transition region, at the free edge, with a value of 290 MPa, similar to the equivalent value for the $[0/90]_S$ laminate (280 MPa).

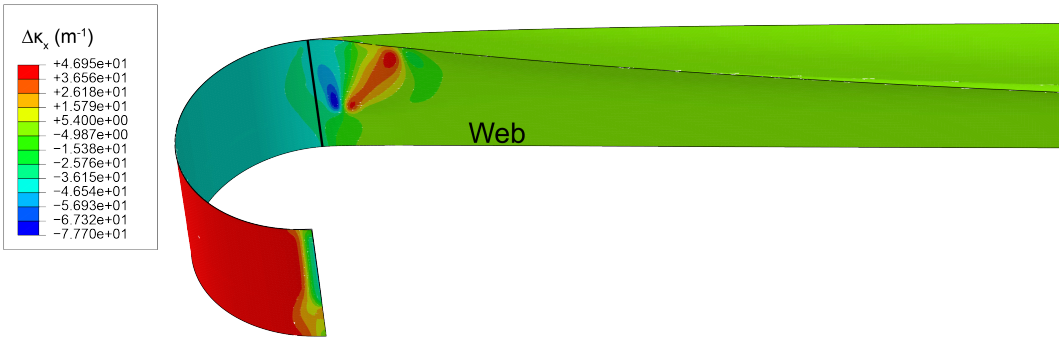

(a) Longitudinal curvature changes ($\Delta\kappa_x$, m^{-1}).

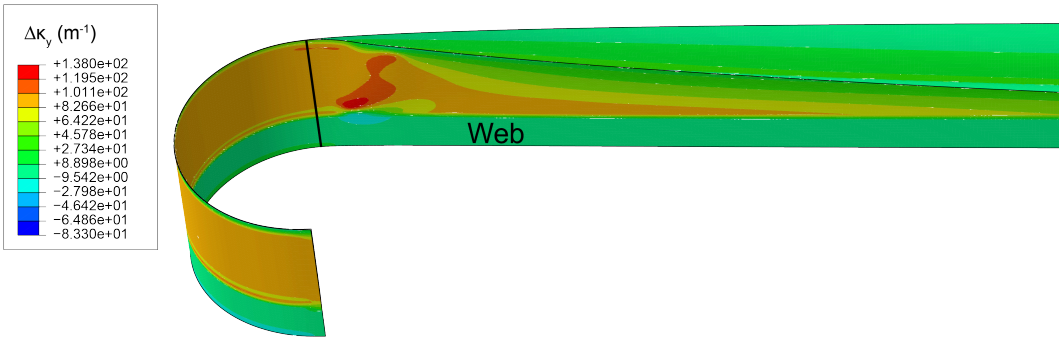

(b) Transverse curvature changes ($\Delta\kappa_y$, m^{-1}).

Figure 5.10: Curvature plots from numerical simulation results for the $[\pm 45_{GFPW}/0_{CF}/\pm 45_{GFPW}]$ TRAC structure.

Using this simulation framework, the effect of reducing the hub radius can also be studied. Figure 5.12 shows the longitudinal stress distribution for TRAC structures coiled around hubs with $R = 19.1$ mm and $R = 12.7$ mm. Only the stress in Ply-2-I, at a coordinate thickness of $z_i = -15\,\mu$m, is shown, as this is where the maximum stress is observed. Once again, the maximum compressive stresses for these two cases are located in the fully coiled region, with -378 MPa and -577 MPa for the hub with $R = 19.1$ mm and $R = 12.7$ mm, respectively. These values agree very well with the expected values from Equation 5.8. The maximum tensile stress is once again located at the free edge, with values of 302 MPa in both cases.

These results, obtained by decreasing the hub radius, demonstrate that the advantages of the improved laminate, mainly lower stress concentrations in the transition region leading the the maximum compressive stress being in the fully coiled region, are still observed for smaller hubs.

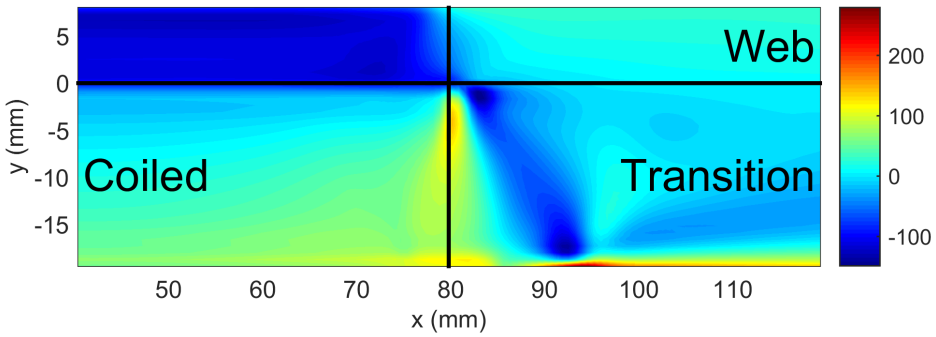

(a) Ply-2-I, $z_i = 15\,\mu m$

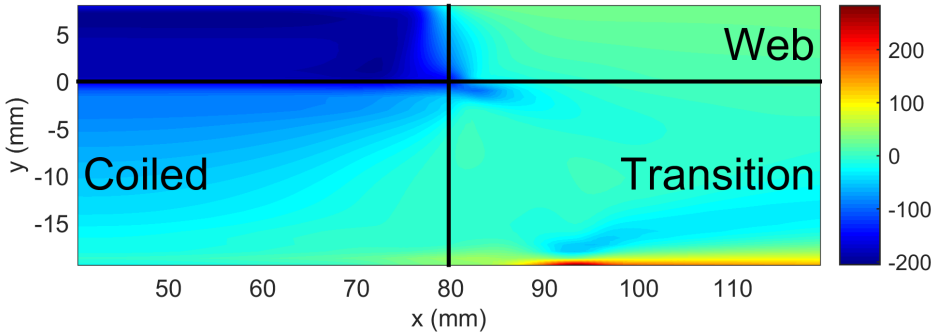

(b) Ply-2-I, $z_i = 0\,\mu m$

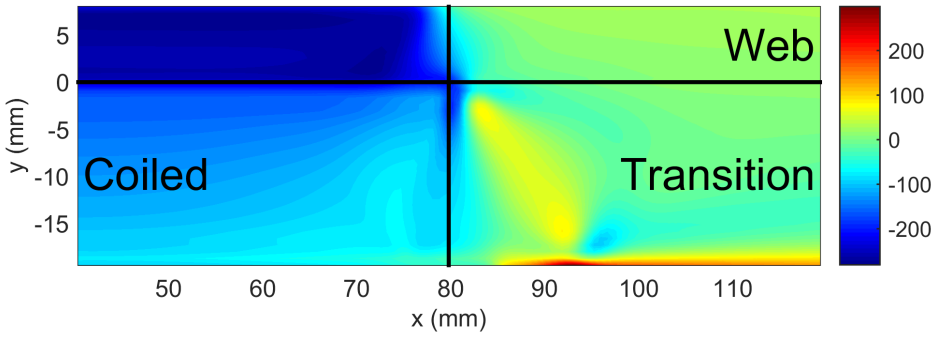

(c) Ply-2-I, $z_i = -15\,\mu m$

Figure 5.11: Longitudinal stress (σ_x, MPa) in the inner flange of the $[\pm 45_{GFPW}/0_{CF}/\pm 45_{GFPW}]$ TRAC structure.

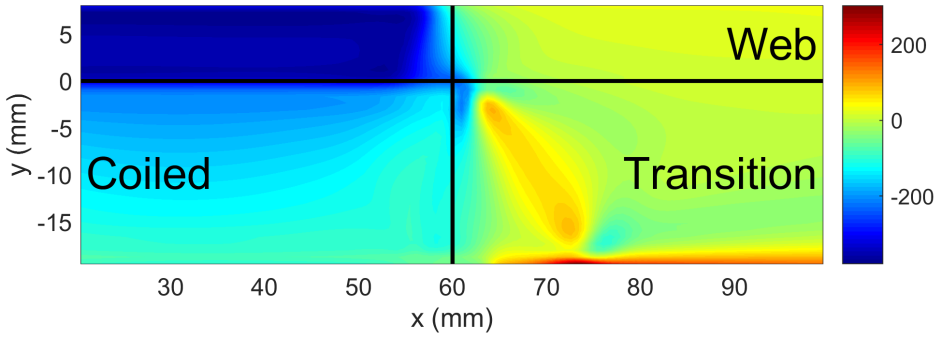

(a) $R = 19.1$ mm

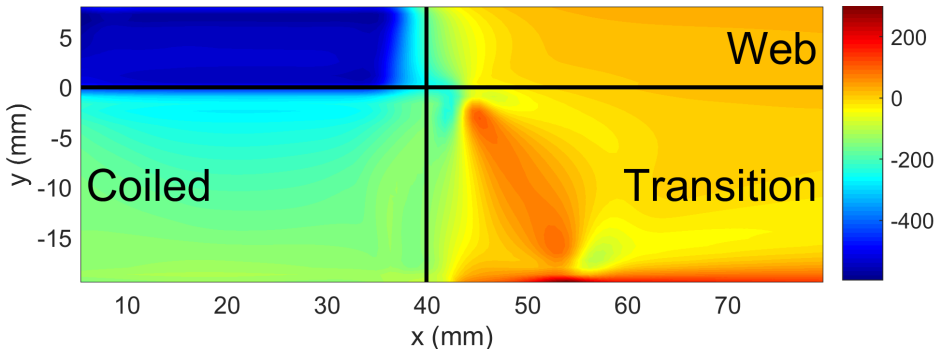

(b) $R = 12.7$ mm

Figure 5.12: Longitudinal stress (σ_x, MPa) in Ply-2-I, $z_i = -15\,\mu$m, of the inner flange of the $[\pm 45_{GFPW}/0_{CF}/\pm 45_{GFPW}]$ TRAC structure for two different hub radii.

5.5 Experimental Validation

To validate the simulation framework presented in Section 5.2, a new set of experiments was performed, using the new laminate analysed in Section 5.4. A non-contact measurement technique was used to obtained the deformed shape during the experimental coiling, and the results were compared with numerical simulations.

5.5.1 Experimental Setup

A dedicated experimental setup for coiling TRAC structures was designed and built. It can be seen in Figure 5.13. It consists of a cylindrical hub made of transparent acrylic, attached to a gearbox (Ondrive P30-60) with a 60:1 ratio. An electric motor drives the gearbox at 60 RPM, turning the hub at only 1 RPM to reproduce quasi-static coiling conditions. Four different hub radii can be used on the setup: 12.7 mm, 19.1 mm, 25.4 mm, and 31.8 mm (0.5", 0.75", 1", and 1.25"). The TRAC cross-section is flattened and attached to the hub using a narrow, flat clamp, as seen in Figure 5.14a. A small piece of sandpaper is bonded under the clamp to increase friction on the structure and prevent any slipping.

A constant tension force is applied at the other end of the structure using a calibrated weight connected to the structure with thin cable and a pulley. This force is applied using an "L" shaped clamp that is attached to the web only, as shown in Figure 5.14b. This leaves the end section free to deform, and aligns the force with the centroid of the cross-section. Three cameras were used to observe the test: one camera looks from above, one camera positioned on the side (looking in the -Y direction, at the web), and the other camera views the inner flange from below (with an angle to avoid looking through the hub).

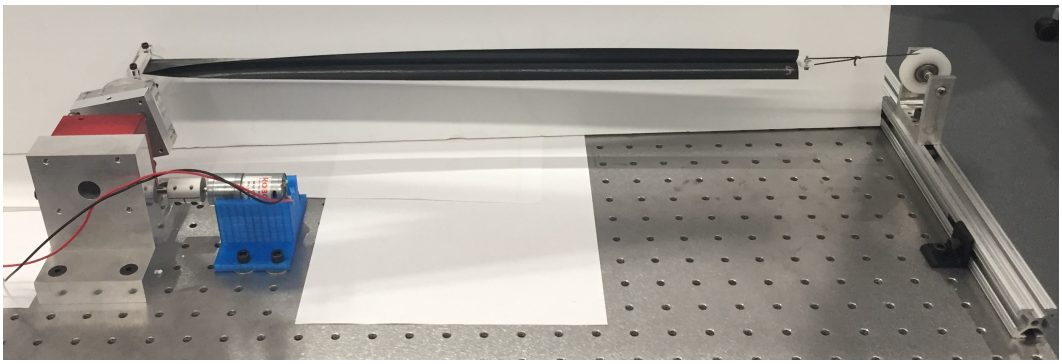

Figure 5.13: Coiling experimental setup.

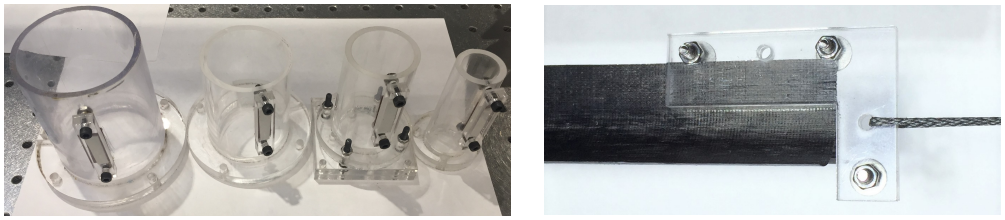

(a) 4 different hub radii: 31.8 mm, 25.4 mm, 19.1 mm, 12.7 mm (from left to right).

(b) Clamp applying tension force to the TRAC structure.

Figure 5.14: Boundary conditions during experimental coiling.

Samples were first coiled around the largest radius (R = 31.8 mm). Because of the thickness of the clamp, the structure can only be wrapped once around the hub. Once the sample had been coiled, the experiment was stopped, and then the structure was uncoiled in a controlled way at the same rotational velocity. Next, coiling was repeated on the second hub (R = 25.4 mm). If cracking occurred during the first test, the other end of the sample was used for the next diameter. If no failure was observed, the same end was reused. Finally, if no cracking occurred after this second coiling, the smallest radii (R = 19.1 mm and R = 12.7 mm) were also tested. Inspection for cracks was done through visual examination. If a cracking sound was

heard during the test, the video recording of the test was used to correlate the sound with the potential failure location, and a more thorough inspection was done under microscope. While this method was useful to find cracks on the outer surface, it did not allow detection of material failure in the inner plies of the laminates.

5.5.2 Curvature Calculation

While material failure provides qualitative information useful to compare different structure laminates, a quantitative measurement is necessary to adequately compare experiments with simulation results. Due to the thinness of the laminate, a non-contact measurement method was preferred to avoid interaction with the structure. The chosen technique consisted in measuring both the outer flange surface and the inner flange surface using a Faro arm (Edge 14000) with a 3D laser scanner attachment (ScanArm HD) to acquire the deformed shape during coiling, and compare the results with the simulations.

To achieve this measurement, a special hub with a cutout was designed and manufactured using a laser cutter with a rotary fixture, as seen in Figure 5.15. The cutout allowed to clearly observe and measure the transition region of the inner flange, without changing the boundary conditions as it was designed to follow the contact points between the structure and the hub. To easily locate the measured point cloud in 3D, the Faro Arm was used to measure the hub, and its axis was used to generate a coordinate system. This left only two degrees of freedom, the rotation around the hub and the translation along its axis, simplifying the process of comparing multiple scans with numerical results.

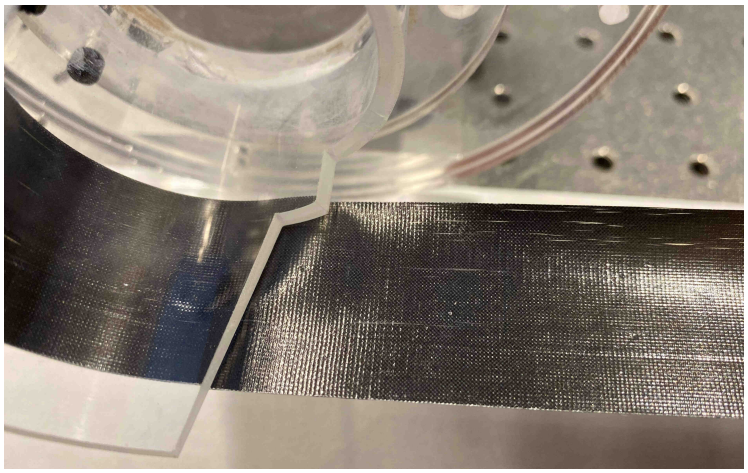

Figure 5.15: Coiled TRAC structure around hub with cutout ($R = 25.4\,\text{mm}$). Inner flange buckling is seen close to the hub.

The resulting measured point cloud, after initial cleaning, was processed using Meshlab, an open source software to process 3D meshes (Cignoni et al., 2008). First, a subset of the point cloud was extracted using the *Point Cloud Simplification* filter, to reduce the number of points. The raw point cloud can have up to 600,000 vertices, so the filter was used to decrease that number to around 6000 in order to reduce noise. Second, the normal at each point was computed with the *Compute Normals for Point Sets* filter, using 10 neighbors to perform the estimate. Third, the surface was reconstructed using the *Ball-Pivoting* algorithm (Bernardini et al., 1999). The default parameters were used, with a clustering radius of 20% and an angle threshold of 90°. Finally, the principal curvatures of the reconstructed surface were computed using the *Pseudoinverse Quadratic Fitting* method.

Using the simulation framework presented in Section 5.2, numerical results were obtained for a TRAC structure with dimensions corresponding to the test samples as measured following the process described in Section 2.5 (r = 12.35 mm, θ_f = 89.4° and w = 8 mm). As the principal curvatures are not computed during the simulations, the same data processing was done on the numerical results. The mesh obtained from the simulations was processed using the same procedure, except for the first step which was ignored to keep all the available nodes (around 15,000). Therefore, it was possible to easily compare the shape measured in experiments with the numerical results.

5.5.3 Results

Four 0.5 m long TRAC structure samples made with the $[\pm 45_{GFPW}/0_{CF}/\pm 45_{GFPW}]$ laminate were tested experimentally. All four samples were successfully coiled around the 31.8 mm hub, without any material damage. All four samples were then coiled around the 25.4 mm hub. One sample suffered a small localized crack in the inner flange, while the other three samples were successfully coiled. While a much more detailed failure analysis would be necessary to accurately compare the two laminates, this second series of tests suggests that the new laminate can be reliably coiled around smaller hubs than the previous $[0/90]_S$ laminate.

To study how tightly TRAC structures made of this new laminate can be packaged, one of the samples was then coiled around both the 19.1 mm and 12.7 mm hubs. While no material failure was observed following coiling around the first hub, small localized damage was seen after the last test, as seen in Figure 5.16. A crack can be observed in the inner flange, close to the web, at the location where simulation

predicts a high localized curvature (see Figure 5.10).

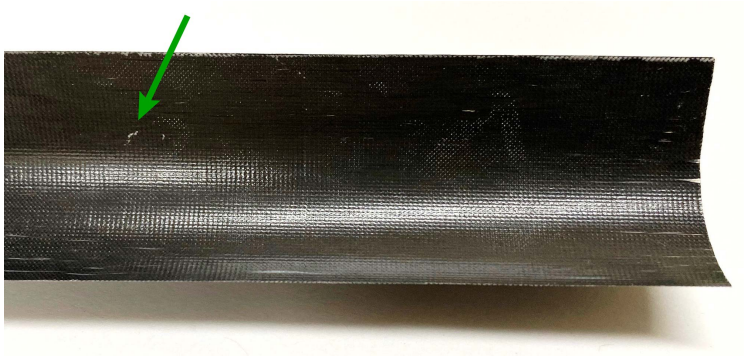

Figure 5.16: Inner flange of TRAC structure after coiling around hub with R = 12.7 mm. A small crack is shown by the green arrow.

By using the partially cut hub from Figure 5.15 (R = 25.4 mm) and stopping the coiling process at a point such that the inner flange was in contact with the hub as close as possible to the cutout without influencing the shape, the deformed shape of the structure was measured using the Faro Arm laser scanner. In this configuration, it was possible to partially measure the buckled shape of the inner flange. The curvature map from this measured shape was then compared to simulation results. Figures 5.17a and 5.17b show the comparison for the outer and inner flanges, respectively. To better illustrate the shape, the color map displays the mean curvature, which is the average of the signed curvature over all directions at a given point. The plots are viewed from the top of the experimental setup, equivalent to looking toward the X direction (see Figure 5.1). The hub is represented in gray on the left side. For each figure, the experimental measurements are on top, while the simulation results are at the bottom.

For the outer flange, the experimental curvature map matches well with simulation results. The gradual flattening of the flange is well captured, as is the fully coiled region. As expected, no localized curvature is seen in the transition region of the outer flange. The only discrepancy is in a small region of the web, in the coiled region where high curvature was measured. However, it appears to be an artefact of the measurement method and data processing, as no similar feature could be visually observed during the experiment.

Similarly, very good agreement is obtained for the inner flange. Due to the presence of the hub, only a portion of the transition region could be measured. The gradual flattening of the flange was well captured. The inner flange buckling observed in

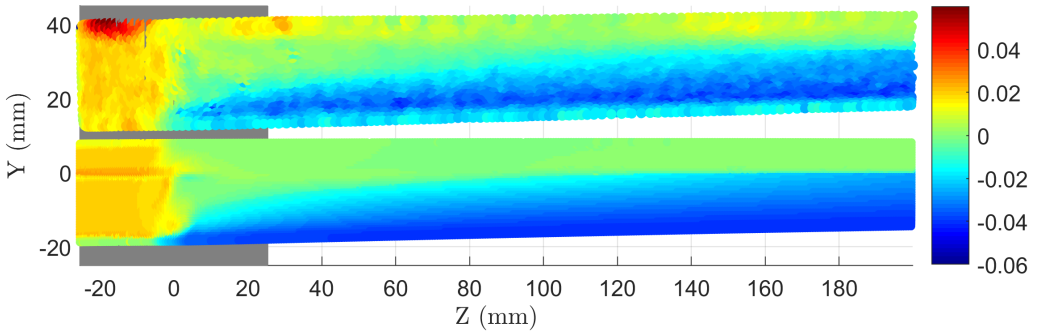

(a) Plots of the mean curvature (mm^{-1}) for the outer flanges. On top is the measured shape from experiment, and at the bottom is the shape extracted from simulation results.

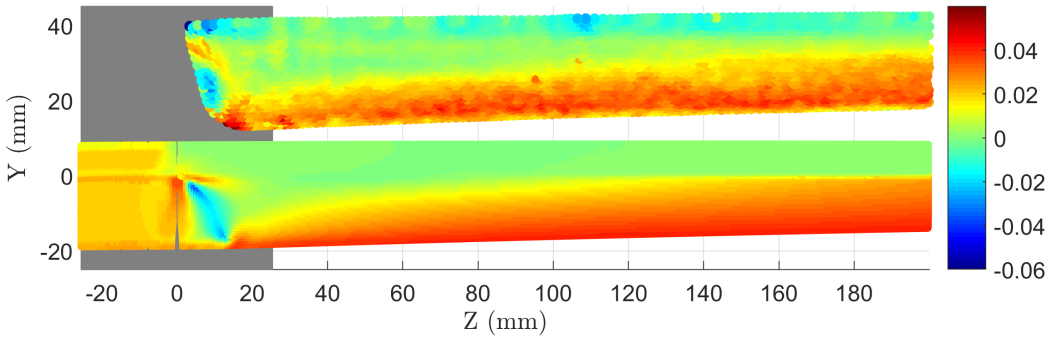

(b) Plots of the mean curvature (mm^{-1}) for the inner flanges. On top is the measured shape from experiment, and at the bottom is the shape extracted from simulation results.

Figure 5.17: Comparison of the flanges mean curvature between experiment and simulation, for a TRAC structure partially coiled around a hub with $R = 25.4$ mm.

experiments can be easily seen in the measurements, and matches very well with the predicted shape from simulation.

This comparison shows that the simulation framework developed to study the coiling behavior of ultra-thin TRAC structures predicts well the observed behavior in experiments.

5.6 Conclusion

A study of the coiling behavior of ultra-thin TRAC structure has been presented in this chapter. A simple coiling mechanism, consisting of a driven rotating hub and a stabilizing tension force, was used to perform preliminary coiling experiments on TRAC structures made with four plies of unidirectional carbon fiber prepreg tape. In the transition region between the fully deployed region and fully coiled region,

inner flange buckling was observed, leading to material failure.

A numerical simulation framework was developed to better understand the mechanics of the coiling process for ultra-thin TRAC structures. Results from this model showed high localized curvature changes in the transition region for the inner flange, leading to high localized stresses. Indeed, the maximum compressive stress in the transverse direction due to this localized curvature change was shown to be 16% higher than the value expected from a simple analytical estimate based on overall curvature changes due to flattening and coiling.

To address this issue, a new laminate was proposed. This laminate is made by sandwiching a single ply of unidirectional carbon fiber between two plies of glass fiber plainweave fabrics. Simulation results for this new design showed that the stress concentration in the transition region is greatly reduced, leading to the maximum compressive stress to be in the fully coiled region. Similar results were obtained when reducing the hub radius. This result is very important for the design of TRAC structures. For this laminate, simple analytical estimates based on the changes of curvature due to flattening and coiling can accurately predict the maximum stresses observed.

Finally, the numerical model was validated by comparing with experiments. The shape of the inner flange was measured using a 3D laser scanner, and the curvature thus obtained was compared with simulation results.

Chapter 6

CONCLUSION

6.1 Summary and Discussion

The overall objectives of the research presented in this thesis were to implement and enable the use of ultra-thin ply composites in coilable structures, focusing on the specific case of the TRAC cross-section. These objectives were divided into four goals that were addressed in this work:

1. Develop a manufacturing process to fabricate structures using the thinnest composite materials available.
2. Study the behavior of the structures in the deployed configuration when subjected to pure bending and torsion.
3. Predict the buckling load of a structure under pure bending.
4. Study the behavior of the structures during the coiling process.

A TRAC structure design was presented in Chapter 2. A requirement on the bending stiffness was derived from a system-level study for a large space solar power satellite. Two laminates made of the thinnest materials available, both a glass fiber plainweave fabric and a carbon fiber unidirectional tape, were studied. Coiling considerations, presented in Chapter 5, showed that the laminate made from both glass fiber plainweave and carbon fiber unidirectional performed better. Using this laminate, the geometric parameters of the TRAC cross-section were selected to comply with bending stiffness requirement.

The challenges of working with thin-ply composites were also addressed in Chapter 2. Accurate material stiffness properties were obtained by combining experimental measurements, both at the ply level and at the laminate level, and the classical lamination theory. An in-autoclave manufacturing process for ultra-thin composite TRAC structure was developed, where the flanges are first cured and then bonded together in a subsequent step. The post-cured shape of the prototypes was observed to change significantly due to residual stresses. A method to measure the as-built shape of the prototypes was developed in order to mitigate this variation in shape.

An investigation of the structure's behavior in its deployed configuration was presented in Chapter 3. Three prototypes were tested under pure bending around both axes of the cross-section. Bending around the Y axis was symmetric, while bending around the X axis had two load cases: web in compression ($+X$) and web in tension ($-X$). The behavior was highly nonlinear due to large deformation and localized buckling events. For all three loading cases, two regimes were observed, with a linear pre-buckling phase followed by a gradual buckling event transitioning into a stable post-buckling phase. This second regime continued until ultimate buckling occurred, which occurred at a load as high as four times the initial buckling moment.

A numerical model was developed using Abaqus 2018 to simulate this pure bending loading case. The model was shown to have good agreement with the experiments, and was able to predict accurately the pre-buckling regime, the initial buckling event and some of the stable post-buckling regime. Ultimate buckling was not predicted by the model.

This simulation framework was used to study the effect of varying the structure length from 300 mm to 5000 mm on the initial buckling load. For all three load cases ($+X$, $-X$ and Y), buckling was first a localized mode and transitioned to a global lateral-torsional mode past a certain length. Nonlinear effects in the pre-buckling regime were shown to have a significant impact on the buckling load when the flanges are loaded in compression ($-X$ and Y), leading to a mostly constant buckling load across the full length range. This was due to the localization of the deformation in the flanges during the pre-buckling phase, making the buckling wavelength constant.

The torsional behavior of TRAC structures was also studied in Chapter 3, both experimentally and numerically. The simulation model was able to accurately predict the torsional behavior observed in experiments. The torsional stiffness was shown to increase quadratically with twist. Initial twist in the test prototype due to the manufacturing process was observed, but had little impact on the results as the torsional stiffness is low at small rotation angles due to the open cross-section of the TRAC structure.

An analytical method to predict buckling of TRAC structures under pure bending was proposed in Chapter 4. This was achieved by studying a simplified structure, where only the flange loaded under non-uniform compression was present. It consisted of a cylindrical shell panel simply supported on three sides, with one longitudinal free edge. The buckling load was estimated using the Rayleigh-Ritz method. Partially

uncoupled stability equations for a balanced laminate were derived. While these equations could not directly solve the problem of interest in the thesis due to the non-uniform compression and the free edge, they were used to obtain the shape functions for the in-plane displacements from the out-of-plane displacement, reducing the number of unknowns in the system. This analytical model was shown to overestimate the buckling load of a 500 mm composite TRAC structure by 44%.

The coiling behavior of TRAC structures was investigated in Chapter 5. Material failure was observed during experimental testing of prototypes made from a $[0/90]_S$ carbon fiber laminate. Inner flange buckling was observed in the transition region between the fully coiled and fully deployed regions, leading to high localized curvature at the failure location. A numerical simulation framework was developed to better understand this coiling process. Results showed high transverse localized curvature in the transition region, leading to high transverse stress at the failure location. To mitigate this issue, a new laminate, consisting of a unidirectional carbon fiber ply sandwiched between two glass fiber plainweave fabric layers, was proposed. Simulation results for this laminate showed that stress concentrations were reduced enough in the transition region that the maximum stress was in the fully coiled region. This result is very important for the design of TRAC structures, as this shows that simple analytical estimates based on the change of curvatures due to flattening and coiling can accurately predict the maximum stresses observed.

The contributions presented in the thesis enable the use of ultra-thin ply composites in the design of coilable structures. Tools to quickly estimate the main structural properties were developed, with closed-form equations for the bending stiffness and an analytical method to predict the buckling load under pure bending. This analytical method is general, and could be used to predict buckling under different loading conditions and boundary conditions if at least one flange is under compression. It was also shown that by carefully selecting the laminate for the structure, the maximum stresses during the coiling process is in the fully coiled region, and that these values can be predicted by computing the strains due to the change of curvatures (flattening and coiling). These estimates of the bending stiffness, buckling moment and maximum coiling stresses enable the rapid design of coilable structures for various applications. These designs can then be studied in great detail by using the experimental methods and numerical simulation frameworks developed for pure bending, torsion and coiling.

6.2 Future Work

Several areas of research can be explored to complement the work presented in this thesis.

The study of the effect of the structure length on the initial buckling load presented in Chapter 3 predicted that this critical load is mostly constant with length for two of the three load cases. This was due to nonlinear effects in the pre-buckling regime. However, only experiments at a length of 575 mm were performed, well below the predicted transition point from localized flange buckling to global lateral-torsional buckling. This was limited by the experimental setup used, as prototypes as long as 1.6 m were fabricated. Larger scale experiments should be performed to validate the conclusions of the present study.

Numerical simulations of the behavior under pure bending gave limited results for the post-buckling regime. While the loss of stiffness following the initial buckling event was well predicted, convergence issues in the stable post-buckling regime prevented the simulations to reach the ultimate buckling load observed in experiments. Other techniques, such as generalized path-following (Eriksson, 1998; Groh, Avitabile, and Pirrera, 2018), are more suited to predict the full post-buckling behavior and could be used to predict the ultimate buckling load.

The coiling study presented in Chapter 5 has focused on reducing the maximum compressive stress observed during the coiling process. However, while material failure was observed in the experiments, no prediction of failure was performed based on the results from the numerical simulations. Incorporating a suitable failure criterion in the numerical model to predict material failure would benefit the design process.

BIBLIOGRAPHY

Aguirre-Martinez, M., Bowen, D.H., Davidson, R., Lee, R.J., and Thorpe, T. (1986). "The development of a continuous manufacturing method for a deployable satellite mast in CFRP". In: *British Plastics Congress*. Citeseer, pp. 107–110.

Almroth, B.O. (1962). "Buckling of a Cylindrical Shell Subjected to Nonuniform External Pressure". In: *Journal of Applied Mechanics* 29.4, pp. 675–682. ISSN: 0021-8936. DOI: 10.1115/1.3640653.

Amacher, R., Cugnoni, J., Botsis, J., Sorensen, L., Smith, W., and Dransfeld, C. (2014). "Thin ply composites: Experimental characterization and modeling of size-effects". In: *Composites Science and Technology* 101, pp. 121–132. ISSN: 0266-3538. DOI: https://doi.org/10.1016/j.compscitech.2014.06.027.

Ansari, R., Sahmani, S., and Rouhi, H. (2011). "Rayleigh–Ritz axial buckling analysis of single-walled carbon nanotubes with different boundary conditions". In: *Physics Letters A* 375.9, pp. 1255–1263. ISSN: 0375-9601. DOI: https://doi.org/10.1016/j.physleta.2011.01.046.

Arya, M., Lee, N., and Pellegrino, S. (2016). "Ultralight Structures for Space Solar Power Satellites". In: *3rd AIAA Spacecraft Structures Conference*. 2016–1950. DOI: 10.2514/6.2016-1950.

ASTM (2015). *Standard Test Method for In-Plane Shear Properties of Polymer Matrix Composite Materials by the Rail Shear Method*. Standard. ASTM International.

Banik, J.A. and Ardelean, E.V. (2010). "Verification of a retractable solar sail in a thermal-vacuum environment". In: *51st AIAA/ASME/ASCE/AHS/ASC Structures, Structural Dynamics, and Materials Conference*. AIAA. Orlando, FL, p. 2585.

Banik, J.A. and Murphey, T.W. (2010). "Performance Validation of the Triangular Rollable and Collapsible Mast". In: *Proceedings of the 24th Annual AIAA/USU Conference on Small Satellites*. AIAA. Logan, UT.

Batdorf, S.B. (1947). *A simplified method of elastic-stability analysis for thin cylindrical shells*. Technical Report NACA-TR-874. NACA.

Bazant, Z.P. and Cedolin, L. (2010). *Stability of structures: elastic, inelastic, fracture and damage theories*. World Scientific.

Becker, H. and Gerard, G. (1962). "Elastic stability of orthotropic shells". In: *Journal of the Aerospace Sciences* 29.5, pp. 505–512.

Bernardini, F., Mittleman, J., Rushmeier, H., Silva, C., and Taubin, G. (1999). "The ball-pivoting algorithm for surface reconstruction". In: *IEEE Transactions on Visualization and Computer Graphics* 5.4, pp. 349–359. DOI: 10.1109/2945.817351.

Bessa, M.A. and Pellegrino, S. (2017). "Design of ultra-thin composite deployable shell structures through machine learning". In: *IASS Annual Symposium "Interfaces: architecture . engineering . science"*. Hamburg, Germany.

Betts, B., Spencer, D., Nye, B., Munakata, R., Bellardo, J.M., Wong, S.D., Diaz, A., Ridenoure, R.W., Plante, B.A., Foley, J.D., et al. (2017). "Lightsail 2: Controlled solar sailing using a CubeSat". In: *The 4th International Symposium on Solar Sailing. Kyoto Research Park, Kyoto, Japan (17–20 Jan 2017b)*.

Biddy, C. and Svitek, T. (2012). "LightSail-1 solar sail design and qualification". In: *Proceedings of the 41st Aerospace Mechanisms Symposium*. Pasadena, CA.

Brush, D.O. and Almroth, B.O. (1975). *Buckling of Bars, Plates, and Shells*. McGraw-Hill.

Campbell, D., Barrett, R., Lake, M.S., Adams, L., Abramson, E., Scherbarthn, M.R., Welsh, J.S., Freebury, G., Beidleman, N., and Abbot, J. (2006). "Development of a novel, passively deployed roll-out solar array". In: *2006 IEEE Aerospace Conference*. IEEE, 9–pp.

Chamberlain, M.K., Kiefer, S.H., and Banik, J.A. (2018). "On-orbit Structural Dynamics Performance of the Roll-Out Solar Array". In: *2018 AIAA Spacecraft Structures Conference*. 2018–1942. DOI: 10.2514/6.2018-1942.

Chu, K. and Krishnamoorthy, G. (1967). "Buckling of open cylindrical shells". In: *Journal of the Engineering Mechanics Division* 93.2, pp. 177–206.

Cignoni, P., Callieri, M., Corsini, M., Dellepiane, M., Ganovelli, F., and Ranzuglia, G. (2008). "MeshLab: an Open-Source Mesh Processing Tool". In: *Eurographics Italian Chapter Conference*. Ed. by V. Scarano, R. De Chiara, and U. Erra. The Eurographics Association. ISBN: 978-3-905673-68-5. DOI: 10.2312/LocalChapterEvents/ItalChap/ItalianChapConf2008/129-136.

Cox, K.B. and Medina, K.A. (2018). "An Investigation of Inner Flange Buckling in Furlable Composite Booms". In: *Proceedings of the American Society for Composites—Thirty-third Technical Conference*.

Cox, K.B. and Medina, K.A. (2019). "Scalability of Triangular Rollable and Collapsible Booms". In: *AIAA Scitech 2019 Forum*. 2019–2026. DOI: 10.2514/6.2019-2026.

Crisfield, M.A. (1981). "A fast incremental/iterative solution procedure that handles "snap-through"". In: *Computational Methods in Nonlinear Structural and Solid Mechanics*. Ed. by A.K. Noor and H.G. McComb. Pergamon, pp. 55–62. ISBN: 978-0-08-027299-3. DOI: https://doi.org/10.1016/B978-0-08-027299-3.50009-1.

Daniel, I.M. and Ishai, O. (2005). *Engineering mechanics of composite materials*. 2nd Edition. Oxford university press New York.

Dong, S.B., Pister, K.S., and Taylor, R.L. (1962). "On the theory of laminated anisotropic shells and plates". In: *Journal of the Aerospace Sciences* 29.8, pp. 969–975.

Donnell, L.H. (1933). *Stability of thin-walled tubes under torsion*. Technical Report NACA-TR-479. NACA.

Donnell, L.H. (1934). "A new theory for the buckling of thin cylinders under axial compression and bending". In: *Trans. Asme* 56.11, pp. 795–806.

Eriksson, A. (1998). "Structural instability analyses based on generalised path-following". In: *Computer Methods in Applied Mechanics and Engineering* 156.1, pp. 45–74. ISSN: 0045-7825. DOI: https://doi.org/10.1016/S0045-7825(97)00200-4.

Fernandez, J.M. (2017). "Advanced Deployable Shell-Based Composite Booms for Small Satellite Structural Applications Including Solar Sails". In: *4th International Symposium on Solar Sailing*. Tokyo, Japan.

Fernandez, J.M. (2018). "Sheath-based rollable lenticular-shaped and low-stiction composite boom". US Patent 9,863,148.

Groh, R.M.J., Avitabile, D., and Pirrera, A. (2018). "Generalised path-following for well-behaved nonlinear structures". In: *Computer Methods in Applied Mechanics and Engineering* 331, pp. 394–426. ISSN: 0045-7825. DOI: https://doi.org/10.1016/j.cma.2017.12.001.

Herbeck, L., Leipold, M., Sickinger, C., Eiden, M., and Unckenbold, W. (2001). "Development and test of deployable ultra-lightweight cfrp-booms for a solar sail". In: *Spacecraft Structures, Materials and Mechanical Testing*. Vol. 468, p. 107.

Hess, T.E. (1961). "Stability of orthotropic cylindrical shells under combined loading". In: *ARS Journal* 31.2, pp. 237–246.

Hoang, B., White, S., Spence, B., and Kiefer, S. (2016). "Commercialization of Deployable Space Systems' roll-out solar array (ROSA) technology for Space Systems Loral (SSL) solar arrays". In: *2016 IEEE Aerospace Conference*, pp. 1–12. DOI: 10.1109/AERO.2016.7500723.

Jaunky, N. and Knight Jr, N.F. (1999). "An assessment of shell theories for buckling of circular cylindrical laminated composite panels loaded inaxial compression". In: *International Journal of Solids and Structures* 36.25, pp. 3799–3820. ISSN: 0020-7683. DOI: https://doi.org/10.1016/S0020-7683(98)00177-2.

Johnson, L., Whorton, M., Heaton, A., Pinson, R., Laue, G., and Adams, C. (2011). "NanoSail-D: A solar sail demonstration mission". In: *Acta Astronautica* 68.5, pp. 571–575.

Jones, R.M. (2006). *Buckling of bars, plates, and shells*. Bull Ridge Corporation.

Khan, A.I., Borowski, E.C., and Taha, M.R. (2016). "Dynamic Deployment of Composite Tape Springs". In: *Proceedings of the American Society for Composites: Thirty-First Technical Conference*.

Kollar, L.P. and Springer, G.S. (2003). *Mechanics of composite structures*. Cambridge University Press.

Krishnamoorthy, G. and Narang, B.S. (1977). "Buckling of open cylindrical shells under combined compression and bending stress". In: *AIAA Journal* 15.3, pp. 322–328. DOI: 10.2514/3.7326.

Leipold, M., Eiden, M., Garner, C.E., Herbeck, L., Kassing, D., Niederstadt, T., Krüger, T., Pagel, G., Rezazad, M., Rozemeijer, H., Seboldt, W., Schöppinger, C., Sickinger, C., and Unckenbold, W. (2003). "Solar sail technology development and demonstration". In: *Acta Astronautica* 52.2. Selected Proceedings of the 4th IAA International conference on L ow Cost Planetary Missions, pp. 317–326. ISSN: 0094-5765. DOI: https://doi.org/10.1016/S0094-5765(02)00171-6.

Leipold, M., Runge, H., and Sickinger, C. (2005). "Large SAR membrane antennas with lightweight deployable booms". In: *28th ESA Antenna Workshop on Space Antenna Systems and Technologies, ESA/ESTEC*. European Space and Technology Research Centre Noordwijk, The Netherlands, p. 8.

Love, A.E.H. (1892). *A treatise on the mathematical theory of elasticity*. Cambridge University Press.

Magnucki, K. and Maćkiewicz, M. (2006). "Elastic buckling of an axially compressed cylindrical panel with three edges simply supported and one edge free". In: *Thin-Walled Structures* 44.4, pp. 387–392. ISSN: 0263-8231. DOI: https://doi.org/10.1016/j.tws.2006.04.004.

Murphey, T.W. and Banik, J.A. (2011). "Triangular rollable and collapsible boom". US Patent 7,895,795.

Murphey, T.W., Francis, W., Davis, B., and Mejia-Ariza, J.M. (2015). "High strain composites". In: *2nd AIAA Spacecraft Structures Conference*. 2015–0942.

Murphey, T.W., Turse, D., and Adams, L. (2017). "TRAC Boom Structural Mechanics". In: *4th AIAA Spacecraft Structures Conference*. 2017–0171. Grapevine, TX.

NASA (2019). *Roll-Out Solar Array*. URL: https://www.nasa.gov/mission_pages/station/research/experiments/explorer/Investigation.html?#id=1876 (visited on 11/05/2019).

NASA/MSFC/D-Higginbotham (2012). *NanoSail-D Home Page*. URL: https://www.nasa.gov/mission_pages/smallsats/nanosaild.html (visited on 11/05/2019).

Ning, X. and Pellegrino, S. (2017). "Experiments on imperfection insensitive axially loaded cylindrical shells". In: *International Journal of Solids and Structures* 115-116, pp. 73–86. ISSN: 0020-7683. DOI: https://doi.org/10.1016/j.ijsolstr.2017.02.028.

Novozhilov, V.V. (1959). *The theory of thin shells*. Trans. by P.G. Lowe. P. Noordhoff.

Onoda, J. (1985). "Optimal laminate configurations of cylindrical shells for axial buckling". In: *AIAA Journal* 23.7, pp. 1093–1098. DOI: 10.2514/3.9042.

Peterson, J.P., Seide, P., and Weingarten, V.I. (1968). *Buckling of thin-walled circular cylinders*. Technical Report SP-8007. NASA.

Peterson, M.E. and Murphey, T.W. (2013). "Large Deformation Bending of Thin Composite Tape Spring Laminates". In: *54th AIAA/ASME/ASCE/AHS/ASC Structures, Structural Dynamics, and Materials Conference*, p. 1667. DOI: 10.2514/6.2013-1667.

Pollard, E. and Murphey, T.W. (2006). "Development of Deployable Elastic Composite Shape Memory Alloy Reinforced (DECSMAR) Structures". In: *47th AIAA/ASME/ASCE/AHS/ASC Structures, Structural Dynamics, and Materials Conference*. DOI: 10.2514/6.2006-1681.

Rimrott, F. Paul J. (1965). "Storable tubular extendible member: a unique machine element". In: *Machine Design* 37.28, pp. 156–165.

Roybal, F.A., Banik, J.A., and Murphey, T.W. (2007). "Development of an elastically deployable boom for tensioned planar structures". In: *48th AIAA/ASME/ASCE/AHS/ASC Structures, Structural Dynamics, and Materials Conference*. 2007–1838.

Sakovsky, M. and Pellegrino, S. (2019). "Closed cross-section dual-matrix composite hinge for deployable structures". In: *Composite Structures* 208, pp. 784–795. ISSN: 0263-8223. DOI: https://doi.org/10.1016/j.compstruct.2018.10.040.

Seide, P. and Weingarten, V.I. (1961). "On the Buckling of Circular Cylindrical Shells Under Pure Bending". In: *Journal of Applied Mechanics* 75, pp. 112–116.

Sihn, S., Kim, R.Y., Kawabe, K., and Tsai, S.W. (2007). "Experimental studies of thin-ply laminated composites". In: *Composites Science and Technology* 67.6, pp. 996–1008. ISSN: 0266-3538. DOI: https://doi.org/10.1016/j.compscitech.2006.06.008.

Spence, B.R., White, S., LaPointe, M., Kiefer, S., LaCorte, P., Banik, J., Chapman, D., and Merrill, J. (2018). "International Space Station (ISS) Roll-Out Solar Array (ROSA) Spaceflight Experiment Mission and Results". In: *2018 IEEE 7th World Conference on Photovoltaic Energy Conversion (WCPEC) (A Joint Conference of 45th IEEE PVSC, 28th PVSEC 34th EU PVSEC)*, pp. 3522–3529. DOI: 10.1109/PVSC.2018.8548030.

Stohlman, O.R. and Loper, E.R. (2016). “Thermal deformation of very slender triangular rollable and collapsible booms”. In: *3rd AIAA Spacecraft Structures Conference, San Diego, California*. 2016–1469.

Szyc, W., Laszczyk, Z., and Magnucki, K. (2006). “Elastic buckling of an axially compressed sandwich cylindrical panel with three edges simply supported and one edge free”. In: *Thin-Walled Structures* 44.8, pp. 910–918. ISSN: 0263-8231. DOI: https://doi.org/10.1016/j.tws.2006.07.004.

Timoshenko, S.P. and Gere, J.M. (1961). *Theory of elastic stability*. 2nd Edition. New York: McGraw-Hill.

Turula, P. and Chu, K. (1970). “Buckling of open cylindrical shells with imperfections”. In: *Journal of the Engineering Mechanics Division* 96.6, pp. 1125–1142.

Varadan, T.K. and Bhaskar, K. (1999). *Analysis of Plates: theory and problems*. Narosa Publishing House.

Whorton, M., Heaton, A., Pinson, R., Laue, G., and Adams, C. (2008). “Nanosail-D: the first flight demonstration of solar sails for nanosatellites”. In: *22nd AIAA/USU Conference on Small Satellites*.

Wilde, R., Zawodny, P., and Magnucki, K. (2007). “Critical state of an axially compressed cylindrical panel with three edges simply supported and one edge free”. In: *Thin-Walled Structures* 45.10. Stability of Structures, pp. 955–959. ISSN: 0263-8231. DOI: https://doi.org/10.1016/j.tws.2007.08.035.

Wilson, L.L. (2017). “Analysis of Packaging and Deployment of Ultralight Space Structures”. PhD thesis. California Institute of Technology.

Yang, H., Liu, L., Guo, H., Lu, F., and Liu, Y. (2019). “Wrapping dynamic analysis and optimization of deployable composite triangular rollable and collapsible booms”. In: *Structural and Multidisciplinary Optimization* 59.4, pp. 1371–1383. ISSN: 1615-1488. DOI: 10.1007/s00158-018-2118-9.

Yang, T.H. and Guralnick, S.A. (1976). “Buckling of axially loaded open shells”. In: *Journal of the Engineering Mechanics Division* 102.2, pp. 199–211.